TECHNISCHE UNIVERSITÄT MÜNCHEN

Institut für Wasserchemie und Chemische Balneologie

Lehrstuhl für Analytische Chemie und Wasserchemie

Nanoparticles and light - Characterization of dynamic changes to nanoparticle surfaces

Sayed M. Amininejad

Vollständiger Abdruck der von der Fakultät für Chemie der Technischen Universität München zur Erlangung des Akademischen Grades eines

Doktors der Naturwissenschaften (Dr. rer. nat.)

genehmigten Dissertation.

Vorsitzender:	apl. Prof. Dr. Christoph Haisch
Prüfer der Dissertation:	1. apl. Prof. Dr. Thomas Baumann
	2. Prof. Dr. Klaus Köhler

Die Dissertation wurde am 15.03.2021 bei der Technischen Universität München eingereicht und dadurch die Fakultät für Chemie am 21.04.2021 angenommen.

Acknowledgements

This thesis is based on research conducted between October 2015 and October 2018 at Lehrstuhl für Analytische Chemie und Wasserchemie, Institut für Wasserchemie und Chemische Balneologie, Technische Universität München. This thesis would not have been completed if certain people had not contributed with their kind support and academic knowledge.

Firstly, I would like to express my sincere gratitude to my advisor Prof. Dr. Thomas Baumann for the exciting topic, continuous encouragement and support throughout my PhD work, for his patience, motivation, and immense knowledge. His guidance helped me in all the time of research and writing of this thesis. I could not have imagined having a better advisor and mentor for my PhD study.

I want to thank Prof. Reinhard Niessner and Prof. Martin Elsner for giving me the opportunity to finish my work and giving me the trust to accomplish my thesis. Furthermore, I got many ideas from their profound knowledge for my scientific research.

I want to thank Dr. Natalia P. Ivleva for her support, patient instructions on Raman instrument and for discussing the topic throughout my work. Without her help and knowledge, this work would have been of another quality.

The financial support from Deutsche Forschungsgemeinschaft (DFG) within the research unit 1536 InterNano must be well acknowledged.

Furthermore, I would like to thank all the collaborators in Internano research group for the scientific support, and special thanks goes to Prof. Gabriele Schaumann and Dr. Ing. George Metreveli for ICP-MS measurement of Au@Ag nanoparticles. I thank Christine Sternkopf for developing SEM images. I would like to thank Sebastian Wiesemann for preparation of silicon wafers for SERS measurements.

I want to thank Dr. Nasrin Talebian for her support and guidance during the cooperation work at Islamic Azad University Of Shahreza in Iran.

I want to thank Dr. Matthias Alte for being my mentor and his kind support during this period.

I have enjoyed introducing the subject to some hardworking bachelor and master students for internships and bachelor thesis. These students are Markus Heindl, Clara Schulz, Florian Zand and Daniel Toller.

I would like to thank all my colleagues at IWC for their impressive participation to create an inspiring working atmosphere. I am incredibly grateful to my collaborates in the Geohydrology group: Dr. Martine Ueckert, Dr. Carina Wismeth and Bernhard Köhl. They have contributed immensely to my personal and professional time. The group has been a great source of friendship as well as useful advice and collaboration.

Lastly, I would like to thank my parents, grandparents and siblings for their love and encouragement—especially my mother, who has always supported me unconditionally in all my pursuits.

List of Publications

Amininejad, S.; Ivleva, N. P.; Baumann, T. Characterization of coatings on metallic nanoparticles by surface-enhanced Raman scattering (SERS) for environmental purposes. *Vadose Zone Journal* **2020**, 19 (1), e20076. https://doi.org/10.1002/vzj2.20076

Degenkolb, L.; Leuther, F.; Lüderwald, S.; Philippe, A.; Metreveli, G.; **Amininejad, S.**; Vogel, H.-J.; Kaupenjohann, M.; Klitzke, S. The Fate of Silver Nanoparticles in Riverbank Filtration Systems—The Role of Biological Components and Flow Velocity. *Science of the Total Environment* **2020**, *699*, 134387. https://doi.org/10.1016/j.scitotenv.2019.134387

Amininejad, S.; Baumann, T.; Talebian, N.; Amininezhad, S. M.; Application of ZnO nanoparticles with different morphologies for photocatalytic reduction of a sample azo dye in aqueous solution (submitted).

Abstract

Due to novel properties such as optical properties and high specific surface area, noble metal and semiconductor nanoparticles have been implemented in a wide range of products in different fields. Semiconductor NPs like TiO_2 and ZnO have been used as efficient photocatalytic materials in water purification for degradation of toxic organic pollutants in the presence of light. Noble metal and semiconductor NPs also show antibacterial characteristics, and therefore they have been implemented in a wide variety of products.

However, NPs can be released into the environment during their production, application and disposal, which can adversely result in unknown risks to human health and the environment. Nanoparticles are stabilized with different coating agents to enhance their efficiency by avoiding their aggregation and dissolution, which may also alter the environmental fate of NPs after their release into the environment. Among different methods implemented to characterize the coating of NPs, surface-enhanced Raman spectroscopy is an emerging technology which benefits from optical properties of NPs and has a great potential for detection of different coatings especially on noble metal NPs. In this thesis by profiting from the optical properties of noble metal and semiconductor NPs, we try to develop the knowledge and application of nanotechnology in environmental fields.

In the first part of this thesis, we synthesized Au@Ag nanoparticles to study the exchange and competition of different coating agents with different binding abilities to simulate the release of NPs into a water body with several potential coating agents. Suwannee River Natural Organic Matter (SRNOM), 4-mercaptobenzoic acid (4-MBA) and 4-Mercaptopyridine (4-MPy) were selected molecules for the experiments. It was shown, 4-MPy has a higher binding affinity than SRNOM and 4-MBA through the presence of simultaneous sulfur and nitrogen atoms which leads to dominating the coating process when two coating agents are present in the media at the same time. Furthermore, 4-MBA and 4-MPy make bonds to the SRNOM coated nanoparticle despite that SRNOM coating has been previously formed.

In the second part, the synthesized Au@Ag NPs were successfully coated on silicon wafer to produce SERS substrates to detect different molecules. 4-MBA and 4-MPy were selected as sample molecules, and a detection limit of 5×10^{-9} M was obtained. Also, the substrate was implemented to characterize the 4-MPy coating on P25 Degussa TiO_2 NPs.

In the third part, the P25 Degussa TiO_2 NPs were thermally modified at different temperatures to achieve NPs with different characteristics. The modified NPs were used to characterize the formation and stability of coatings by SERS and also as photocatalytic material for deactivation of sample bacteria. It was observed that the crystal structure of TiO_2 NPs plays an essential role in their application. It was also observed that SERS Spectra of the coating show some changes if heavy metal ions are present in the media during the coating process.

In the last section, ZnO NPs with different morphologies were successfully synthesized via an easy solvothermal method with different solvents. The ZnO NPs were employed for degradation of a sample azo dye. SEM imaging revealed that the particles synthesized in 1-hexanol, ethylene glycol and water have rod, sphere and flower shape, respectively. The photocatalytic efficiencies of the ZnO NPs were affected by their different morphologies and crystal growth habits, particle size and optical properties. Results indicate that flower-like ZnO NPs showed significantly higher photocatalytic efficiency than rod- and sphere-like ZnO NPs.

Contents

1 Theoretical Background

1.1 Introduction and aim of the thesis

Nanotechnology has become one of the most promising technologies applied in a wide variety of areas. Miniaturization of different materials, including noble metals and semiconductors, affords interesting novel properties such as optical properties and high specific surface area.[1,2] Miniaturization of materials down to the nanoscale regime impacts the behaviour and interactions of light with matter especially metals and semiconductors as important nanomaterials with wide application in various sectors such as electronics, food, biomedicine and even for environmental purposes such as water treatment and purification.[3–7] Semiconductor materials like TiO_2 and ZnO have been widely used as efficient photocatalytic material for decomposing toxic organic molecules to H_2O, CO_2, and other harmless molecules in the presence of light.[8,9] Ag, TiO_2 and ZnO NPs also possess significant antibacterial effect towards a broad range of organisms which makes them suitable for antibacterial consumer products.[10–13] Unlike conventional chemical disinfectant, the antibacterial nanomaterials are not expected to produce harmful disinfection byproducts (DBPs).[14] However, NPs can be released into the environment during their production, application and disposal, which can adversely lead to unknown risks to human health and environment.[15,16] Coating agents are generally used to synthesise NPs to stabilize them and avoid aggregation and dissolution of the NPs.[17,18] On the other side, all engineered inorganic nanoparticles (EINPs), coated or uncoated, will interact with natural macromolecules such as natural organic matter (NOM) or humic substances when released into the natural aqueous environment which plays an essential role in the environmental fate and toxicity potential of the NPs.[19,20] Although huge progress has been made in understanding the potential environmental and ecological consequences of EINPs, the knowledge regarding the importance and characterization of coatings on NPs for their environmental fate is still lacking. Especially, different characteristics such as persistence and dynamics of the coating over time in the environment are unknown and more research to understand the interactions between NPs and their coating is required.[21,22] Different scenarios such as developing a natural coating around uncoated NPs, exchange of a surface coating or even formation of multi layer coatings seem possible.[23] Among different methods implemented to characterize the coating of NPs, surface-enhanced Raman spectroscopy (SERS) is an emerging technology which benefits from optical properties of NPs and incorporates nanotechnology into normal Raman spectroscopy.[24] Low measurement runtime and minimal sample processing are main advantages of this method

when compared with other conventional analytical methods. SERS has a great potential for detection of different coatings on noble metal NPs and to some extend for semiconductor NPs.[23,25,26] Until now, SERS phenomenon on semiconductors has not been well investigated and mainly, the enhancement factor observed for semiconductors were greatly lower than those of noble metals.[27,28] Also, most of the experiments using SERS for characterization of coatings on different NPs, have been conducted in the lab using simplified batch systems.[29] Therefore, there is need to adapt this method to be used under environmentally relevant conditions. The aim of this thesis is to study the optical properties of noble metal and semiconductors nanomaterials for environmental purposes. By implementing benefits of optical properties of noble metal and semiconductor NPs, we try to develop the knowledge and application of nanotechnology in environmental fields. The objective is to implement and optimize SERS for characterization and measurement of NOM coatings on metallic and semiconductor NPs. In addition, the morphology and phase structure dependent antibacterial and photocatalytic activity of ZnO and TiO_2 as an important factor are investigated.

The following objectives based on the optical properties of nanomaterials are defined for this thesis:

- To characterize and measure the changes of the coatings on metallic NPs under different environmentally relevant conditions using SERS. In addition to establishing an optimized setup for characterization of different coatings on NPs, the hypothesis if the first contact of potential coating agents derives the fate of the NPs should be investigated. This hypothesis is critical for assessing the stability and transport of NPs in rapidly changing environments, e.g., NPs emitted into rivers or sewage treatment plants.
- To develop and apply a method to characterize and measure the coatings on TiO_2 NPs using Raman microscopy and SERS. This objective aims both the direct measurement of coatings on TiO_2 NPs and also the indirect measurement of the coating through deposition of coated TiO_2 on noble metal SERS-active surfaces.
- To investigate the photocatalytic effect of semiconductor NPs. This objective investigates the factors influencing the interaction of light with NPs in photocatalytic processes such as degradation of environmental pollutants and inactivation of bacteria.

1.2 Electromagnetic spectrum (Light)

The term light is sometimes used as a synonym for electromagnetic radiation ranging from radio waves to gamma rays. As their names suggest, electromagnetic radiation waves are fluctuations of electric and magnetic fields, which can transport energy from one location to another in the form of photons. Visible light is also a small fraction of this electromagnetic spectrum except that the human eye can detect visible waves. Figure 1.1 shows regions of the electromagnetic spectrum, including radio waves, infrared, visible, ultraviolet, X-rays, and gamma rays.

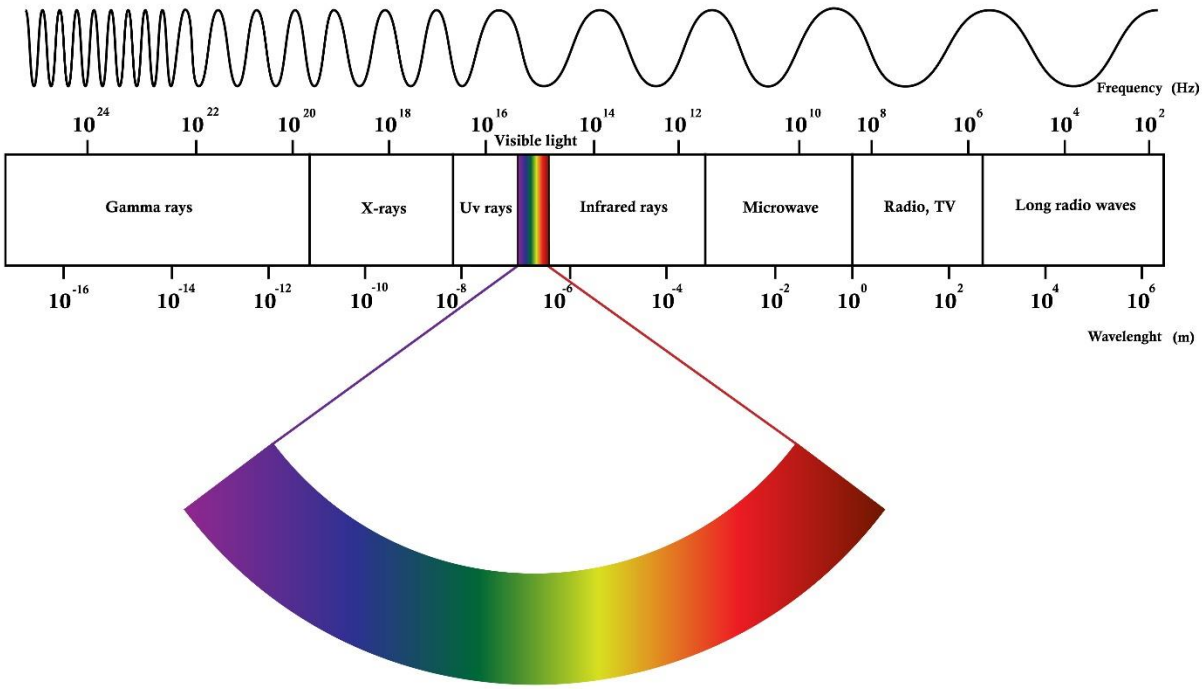

Figure 1.1 The electromagnetic spectrum (Image from: https://www.livescience.com/38169-electromagnetism.html).

1.3 Interaction of light with matter

Different phenomena can happen when light interacts with matter depending on the relationship of the light wavelength and the interfering matter's physical size. Depending on

the material's surface quality, transparency or translucency, the incident light will be reflected, transmitted, absorbed, or scattered.

1.3.1 Interaction of light with bulk metal

Free electrons in a bulk metal move opposite to the electric field's direction when the metal is subjected to a force created by the electric field of light. Positive ions stay fixed in the same position, which causes a shift between the center of distribution of the negative charge and the positive charge. This phenomenon is illustrated in Figure 1.2. The electrons in a metal NP are defined by a simplified model of a gas free of electrons that move against a stationary background of positive ions.[30,31]

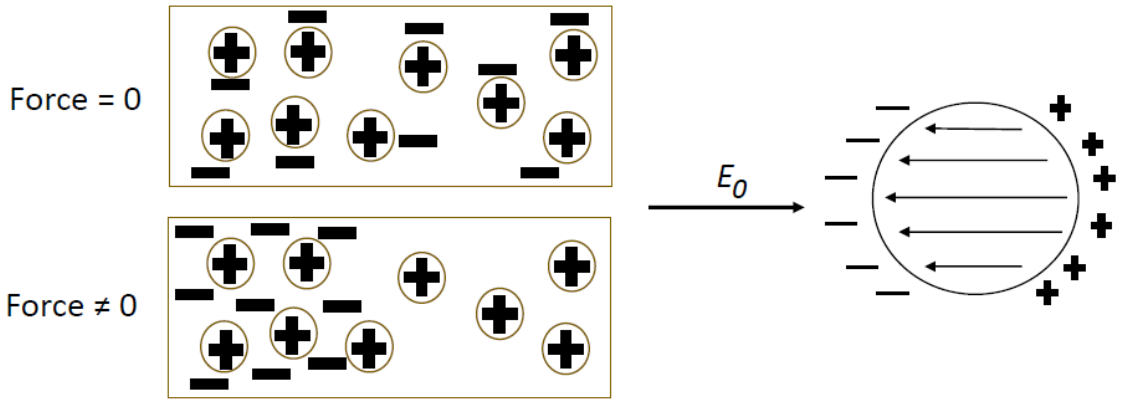

Figure 1.2 Illustration of a metal structure subjected to a force created by an electric field. (Left) bulk and (Right) nanoparticle. Based on Ref.[32]

Free conduction electrons can move over broad distances in bulk metal materials, and therefore usually the electrons do not oscillate against specific localized ions with a restoring force. The motion is quite comparable to a mass being dragged in a viscous fluid. Light with a frequency above the plasma frequency, like UV for metals, will not even oscillate electrons and the light will be absorbed or transmitted in interband transitions of the metal. Light with a frequency below UV will oscillate electrons out of the phase, creating a strong reflection.[32]

1.3.2 Interaction of light with metal nanoparticles

Bulk metal is diminished in three dimensions to form nanoparticles with dimensions less than the wavelength of the incident light. The smaller particle size compared to the wavelength of

the incident light, will lead to a constant electric field across the nanoparticle, causing a uniform displacement of the electron density. The nanoparticle's confined electrons will oscillate while being accompanied by a strong force from positive ionic core background. This force causes a non-propagating collective oscillation of the surface cloud with a characteristic oscillation frequency like a simple harmonic oscillator.[33] This phenomenon is not similar to the bulk metal, which does not have a specific oscillation frequency. The collective oscillation causes a large absorption and scattering cross section, and an amplified local optical electromagnetic field which also plays an import role in surface enhanced-Raman scattering effect. The maximum strength of this electric field occurs just outside the nanoparticle and drops rapidly with distance from the nanoparticle (Figure 1.3).[34]

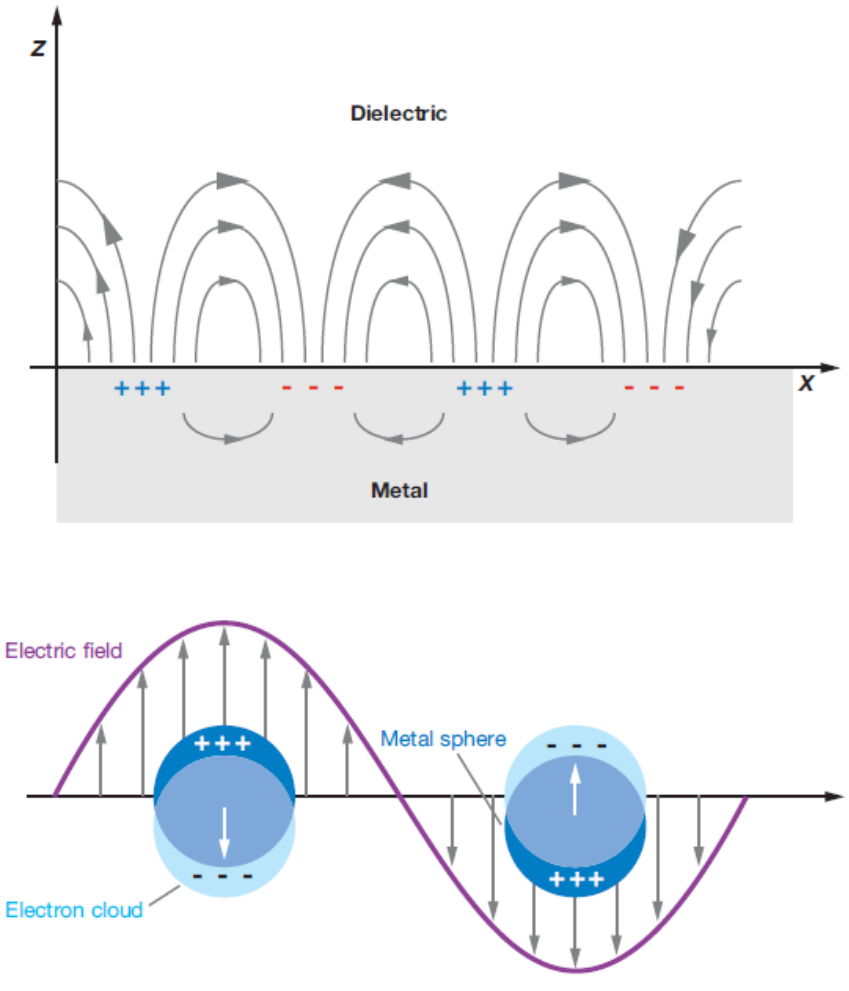

Figure 1.3 Illustration of surface propagating plasmon (top) and localized surface plasmon (LSPR) (bottom). Reprinted from Ref.[34]

1.3.3 Interaction of light with semiconductor nanoparticles

The interaction of semiconductor nanoparticles with light is different from metal materials. Unlike metals, semiconductor materials do not electrically conduct and have no free electrons in their conduction band. The electrons are bound to atoms and are in the valence electronic bands. In metals, the conduction and valence bands overlap together, but in semiconductors, the bands are isolated by an energy gap called band gap as indicated in Figure 1.4.

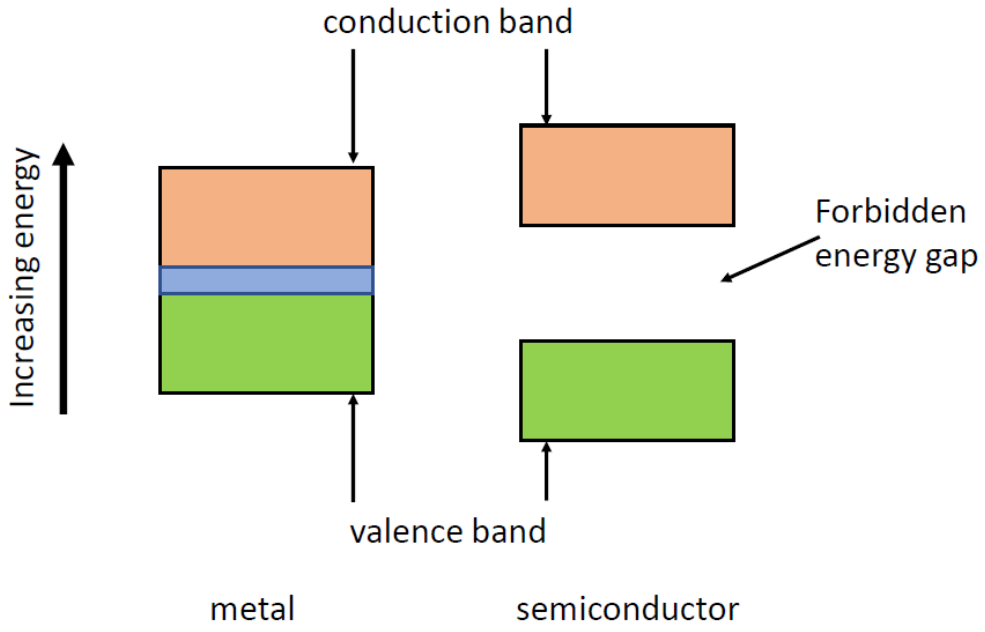

Figure 1.4 Conduction and valence band for metal and semiconductor. Based on Ref.[35]

To overcome the bandgap in semiconductors, an external force like external light is required to convey enough energy to a bound electron to place it in the conduction band accompanied by its separation from the positive charge. Separation of the electron from the charge leaves a positive hole in the valence band. Both the electron and the positive hole are free to move away from their original location, and they move together as electron-hole pair or excitation with the electron orbiting around the hole at an average distance. This kind of photoreaction plays a vital role in photocatalysis, which will be explained more in section 1.4.

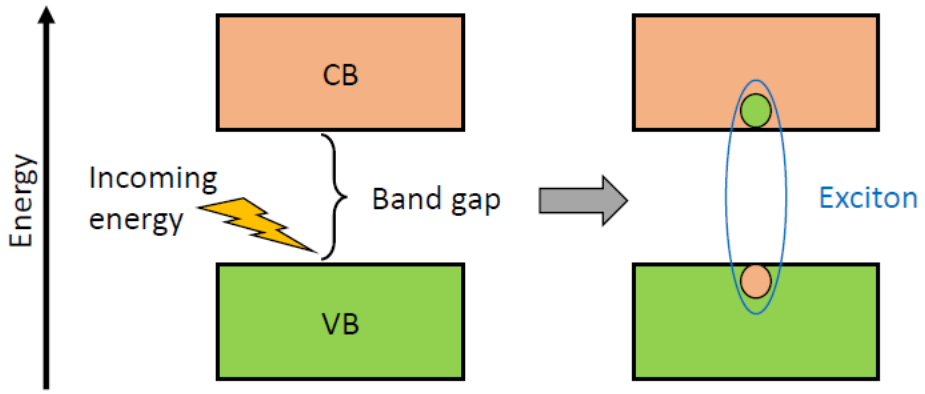

Figure 1.5 Excitation of electron from valence band to conduction band in a semiconductor by light. Based on Ref.[35]

1.4 Photocatalysis

Photocatalysis is a field of chemistry that deals with chemical reaction happening in the presence of light and a photocatalyst. A photocatalyst is a semiconductor, which increases the rate of reaction by its presence. Photocatalysis has a wide range of applications in antibacterial, self-cleaning, deodorizing and water purification.[36–39]

1.4.1 Environmental application of photocatalysis

Although more than 70% of the earth is covered with water bodies, people are constantly battling for a cleaner und purified water as a necessary demand for life.[40,41] As a consequence of the Industrial evolution, more pollution is introduced into the air and water. The removal of organic and biological contaminants (such as organic dyes and drug effluents) from water effluents need a simple, cost-effective, and eco-friendly solution. In the last few years, photocatalysis came up as a promising and well accepted method, especially for the treatment of wastewater polluted with dyes.[42,43]

Among various photocatalysts, TiO_2 and ZnO are recognized as the most photoactive catalysts among employed semiconductors.[44] TiO_2 has a band gap of 3.2 eV with high photocatalytic efficiency, good chemical and optical stability, optimal environmental and biological compatibility.[45] ZnO has a band gap of 3.37 eV, which is comparable to TiO_2 and has mainly been considered due to its relatively lower production costs and easy fabrication.[46,47] Some

experiments have also shown that ZnO exhibits a better efficiency than TiO_2 in photocatalytic degradation of some dyes and other pollutants in water.[48,49]

Size, shape and defects are the crucial factors which significantly influence the photocatalytic and antibacterial performance of these two semiconductors. Therefore, some studies have been focusing on optimization of morphology and crystalline structure of semiconductor NPs.[10,50,51]

TiO_2 exists in three crystalline phases of anatase, rutile and brookite.[52,53] Rutile is the most common natural form of TiO_2, and anatase and rutile are the most common crystalline phases for synthesized TiO_2 NPs. Brookite TiO_2 nanoparticles are challenging to synthesize and usually need highly concentrated acids or high temperatures and pressure for their production.[52,54] In general, the size decrease of TiO_2 and ZnO NPs increases their photocatalytic and antibacterial activity.[55] There are various controversial reports regarding the effect of crystal phase on photocatalytic and antibacterial activity of TiO_2 NPs.[56–58] Despite current debates, some studies show that anatase TiO_2 NPs show a higher antibacterial effect than rutile NPs due to inducing more oxidative stress. However, there are also some other studies which show higher antibacterial activity of rutile NPs.[56–59]

1.4.2 Photocatalytic and antibacterial reaction

The photocatalytic process occurs via several steps through different chemical reactions which are illustrated in Figure 1.6. In the first step, light with energy (*hv*) equal to or greater than the band gap energy (E_g) excites the semiconductor NP. During the interaction, electrons in the valence band (VB) are excited to the conduction band (CB) of the semiconductor NP. Subsequently, electron vacancies remain in the VB and electron-hole (e^--h^+) pairs are generated. In the second step, electron-hole pairs transfer to the photocatalyst surface and reactive oxygen species (ROS) are formed through the reaction of the electron and hole with oxygen and water molecules. The formed highly reactive ROS, e^- and h^+ can effectively degrade dye molecules. The following chemical reactions occur during photocatalytic reaction on the surface of semiconductor NP:

$$\text{Semiconductor NP} + hv \rightarrow e^-(\text{CB}) + h^+(\text{VB})$$

$$O_2 + e^- \rightarrow {}^{\cdot}O_2$$

$$H_2O + h^+ \rightarrow {}^{\cdot}OH + H^+$$

$$^{\cdot}O_2 + H^+ \rightarrow {}^{\cdot}OOH + e^- + H^+ \rightarrow H_2O_2$$

$$H_2O_2 + e^- \rightarrow {}^{\cdot}OH + OH^-$$

Dye + {e^-, h^+, $^{\cdot}O_2$, and/or $^{\cdot}OH$} →Intermediate chemical →oxidized products

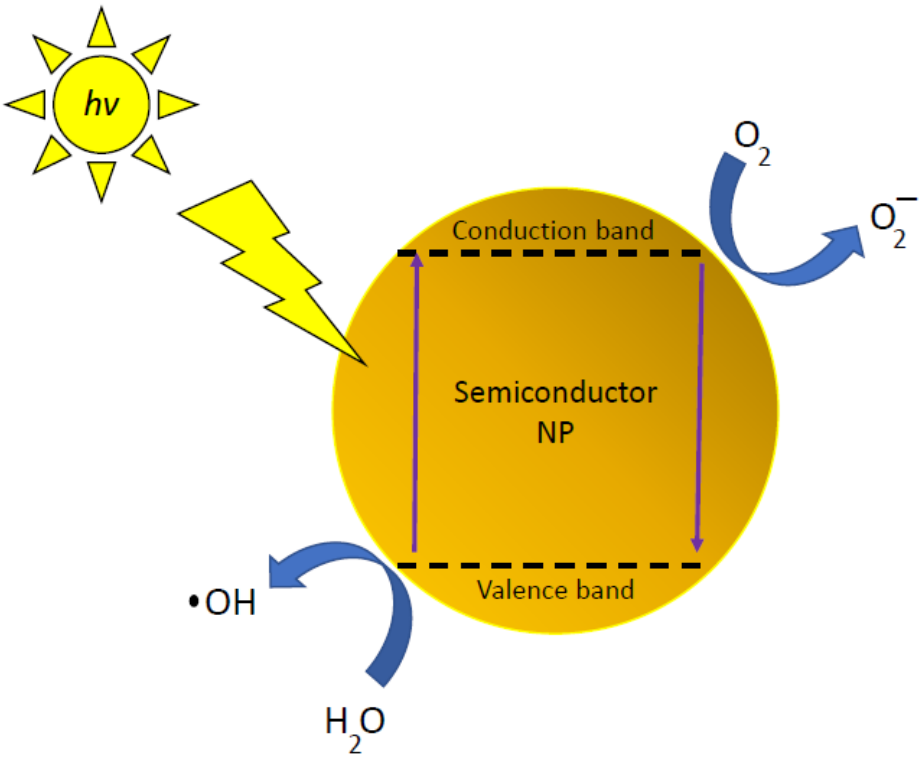

Figure 1. 6 Schematic mechanism of semiconductor NP as photocatalyst. Based on Ref.[60]

Different factors of semiconductor NPs like morphology, surface area, solubility, and surface charge of the semiconductor nanoparticle will strongly influence nanoparticles' availability for uptake into cells and their toxicity for antibacterial application.[61] Following scenarios may affect antibacterial activity of semiconductors:

1) The cations eluted from the powder; 2) Highly reactive oxygen species (ROS) formed including hydroxyl groups ($^{\cdot}OH$), superoxide anions ($^{\cdot}O_2$) and hydrogen peroxide (H_2O_2); 3) pH value 4) Membrane dysfunction; 5) Nanoparticle internalization.[62–65]

Antibacterial and photocatalytic use of NPs is just a small proportion of the broad application of NPs in various fields. The increasing application and use of NPs in different products would

lead to an increased release of NPs in the environment. For toxicity and fate of nanoparticles in the environment, it is essential to study the chemical nature of nanoparticles as well as their coatings.[19]

1.5 Methods for characterization of coatings on NPs

Coating of nanoparticles can alter the stability of the nanoparticles.[17,18] Different methods for characterization of interactions between coatings and NPs are summarized in Figure 1.7.[66] Among different methods implemented to characterize the coating of nanoparticles, surface-enhanced Raman scattering (SERS), is an emerging technology, which has shown great capability for detection of different coatings especially on noble metal nanoparticles.[67]

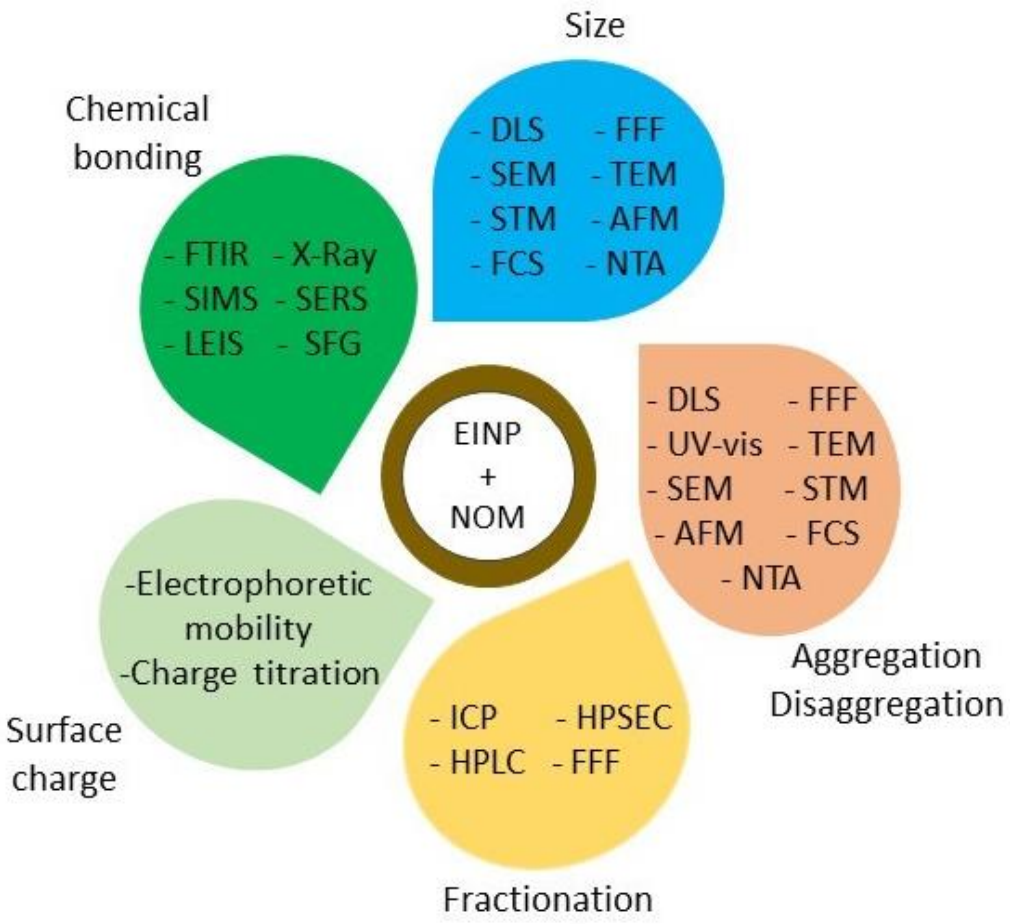

Figure 1.7 Methods to characterize the interaction of coatings and NPs. Based on Ref.[66]

1.6 Surface-enhanced Raman scattering (SERS)

Raman spectroscopy (RS) is a nondestructive vibrational spectroscopic method that provides highly specific information based on the effect of inelastic light scattering by molecules.[68] RS has several advantages such as: 1) a small amount of sample is needed. 2) water is a low Raman scatterer, which makes this method suitable for samples containing water. 3) it is a complementary method of IR spectroscopy, especially for those molecules with a center of inversion where the selection rule is applied.[68–70]

However, limited sensitivity and fluorescence background covering the Raman bands are the main drawbacks of this method.[71] Surface enhanced-Raman scattering is another Raman technique which helps to overcome these drawbacks.[68,72]

Surface-enhanced Raman scattering was firstly observed and discovered on a roughened silver electrode by Fleischmann et al. in 1974.[73] Since then, surface-enhanced Raman scattering has gained increasing attention in chemistry, biology, physics, medicine etc.[74–78] In the early days, the SERS was only focused on group 11 metals (Au, Ag, Cu) due to their high enhancement to Raman scattering. The Raman effect can be dramatically enhanced if a molecule is attached to or in the proximity of noble metal nanostructures. The rapid growth of nanoscience and nanotechnology has contributed to the rapid development of SERS from noble metals to other materials like semiconductors and transition metals.[79–82] SERS has been implemented to investigate different organic and inorganic molecules adsorbed on noble metals and semiconductors.[23,83] The enhancement mechanism for noble metal NPs is different from semiconductors. Electromagnetic enhancement and chemical enhancement are at least the two principal mechanisms contributing to the SERS enhancement.[84] Electromagnetic enhancement plays a vital role in the enhancement on noble metals, and chemical enhancement is the primary enhancement mechanism for semiconductors. The enhancement mechanism for noble metals and semiconductors are explained separately here.

1.6.1 Electromagnetic enhancement

Electromagnetic enhancement on noble metals

There are basically three electromagnetic enhancement theories: surface mirror field theory, lightning effects and localized surface plasmon resonance.[85] Generally, it is believed that electromagnetic enhancement theories come from the enhancement of the electromagnetic field on the surface of the nanoparticle.[70,85] This effect is called localized surface plasmon resonance (LSPR) and will be discussed here.

LSPR is a light absorption mechanism and is observed when laser light in the visible range illuminates rough metal NPs like Au, Ag and Cu. [86,87] A localized surface plasmon arises when the light illuminates a metal NP that is smaller than the wavelength of the incident light, and a local amplification electromagnetic field will be generated on the NP's surface. When molecules are located in the local amplification electromagnetic field, the intensity of incident light that excites Raman mode of the molecule is enhanced. Therefore, the scattering cross of molecules section will be significantly amplified by several orders of magnitude, and as a result, the enhanced Raman scattering spectrum is obtained. The relation between the Raman intensity, I, and the local EM strength, *E*, is usually approximated as $I \approx |E|^4$.[88,89] The relation between local EM strength, E, and the interspaced distance, D, is described by the following equation:[84,90]

$$E \approx (1/D)^{12}$$

Therefore, with increasing the distance between noble metal NP and the target molecule, the SERS signal reduces significantly.

The location of the LSPR band is dependent on the size, shape, identity and aggregation state of the nanoparticle. The chemistry of the medium and even the laser wavelength are other factors influencing the LSPR. For example, the LSPR of a spherical gold nanoparticle with an average size of 50 nm is at about 530 nm, which falls into the green light range.[91,92] Therefore, a suspension of 50 nm gold nanoparticle absorbs green light and transmits red light, which is why this suspension exhibits red color under visible light illumination.[93,94] The Maximum SERS enhancement on noble metal NPs occurs when the target molecule is positioned on the surface of the metal NP, and the diameter of the metal NP is smaller than the wavelength of the incident laser. Also, the incident laser's frequency should match the LSPR of the metal NP

to reach the highest SERS enhancement.[92,95] The electromagnetic enhancement scenario alone cannot explain the different SERS spectra for different molecules on the same substrate. Chemical enhancement is another mechanism discussed to solve the mentioned question.

Electromagnetic enhancement on semiconductors

Due to small electron density in semiconductors, the conduction band plasmon of these materials is supposed to fall in the infrared region. On the other hand, the electron density of valence electrons is as large as 10^{22} to 10^{24} cm^{-1} and therefore supposed to be in the ultraviolet region with a plasmon excitation energy between 4 to 30 eV.[96] Hence, the bulk conduction and valence band plasmons are not applicable for SERS measurements in the visible region of the spectrum.[97] However, there have been some works focusing on shifting the plasmon resonance of semiconductors by various geometries.[98]

It is believed that most likely a combination of surface plasmon, charge transfer (CT), and band gap resonance in addition to EM mechanism is the contributing factor for Raman signal enhancement on semiconductor materials. The majority of studies have proven the charge-transfer mechanism as the main involved mechanism in SERS enhancement of semiconductors.[99,100]

1.6.2 Chemical enhancement

Chemical enhancement is the interaction between the molecule and the surface, including the adsorption orientation feature of the molecule as well as, the CT between the molecule and SERS substrate.[101] The atomic absorption model and the CT model are two mechanisms used to explain this phenomenon, and the scientists widely accepted the latter. The CT model explains that adsorbed molecules can react with atoms on the nanoparticle's surface, and therefore a new chemical bond is formed. This model can explain why the SERS effect will drop to zero immediately with the disappearance of the chemical bond.

CT resonance

Some studies have shown that plasmon resonance plays a role in the Raman enhancement; however, those molecules with similar cross section have shown different enhancements. Basically, those molecules that chemically adsorb on metal nanoparticles have shown the largest enhancement, and these phenomena can be explained by CT mechanism. In this theory, the conduction band orbitals of the metal layer between the highest molecular filled level highest occupied molecular orbital (HOMO) and its first excited unfilled level lowest

unoccupied molecular orbital (LUMO). CT can happen from metal to molecules or from molecules to the metal depending on the relative energies of the metal Fermi level and the HOMO and LUMO levels of the adsorbed molecule (Figure 1.8).

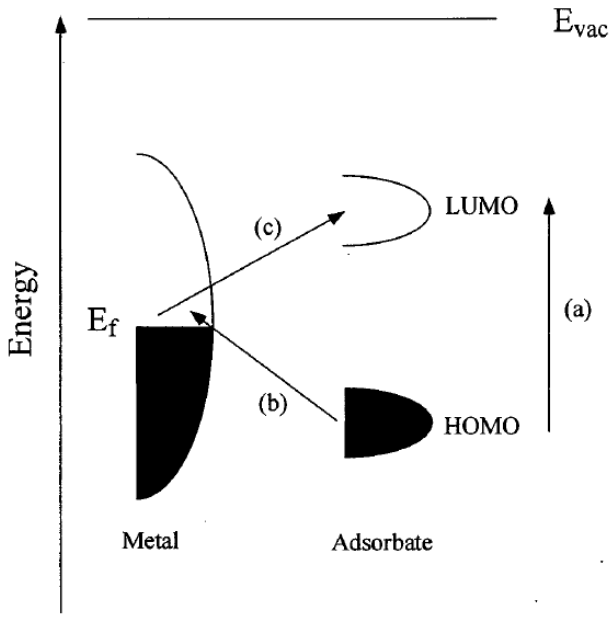

Figure 1.8 Chemical enhancement showing the energy level diagram for a "molecule-metal system". Reprinted from Ref.[88]

In semiconductors, the energy gap is between a full valence band and an empty conduction band. Therefore, the CT between semiconductor material and molecules is dependent on the vibronic coupling, the conduction band and the valence of the molecular excited state and ground state. The CT in Semiconductors can occur via five different pathways which are explained here (Figure 1.9).[25,26,83,102–104]

1) Molecule HOMO-to-CB. The incident light directly excites the electron in the ground state of the molecule from the HOMO to the conduction band's energy level. Instantly the excited electron goes back to a certain ground vibrational energy level of the molecule, and the Raman photon is released.
2) CT complex-to-CB. The formed chemical bonding between the semiconductor and molecule diminishes the formation of a charge transfer complex, leading to the enhancement of the polarizability and subsequently resulting in Raman signals of the original adsorbed molecules.
3) VB-to-molecule LUMO.

The incident light excites the electron in the valence band of the semiconductor to the high energy level LUMO in the molecule, and afterwards, the electron quickly goes back to the valence band and therefore Raman photon is released.

4) Surface state-to-molecule LUMO. The incident light excites the electron from the valence band to the surface defect, forming a surface state. Subsequently, the electron is further excited to the LUMO of the molecule, and a Raman photon is released by the transition to the surface state.
5) CB-to-molecule HOMO. The molecule is excited by the incident light to the energy level LUMO, and the electron is then injected to an energy level in the conduction band of the semiconductor which has the matching energy level. Finally, the electron returns to the molecule's ground vibrational energy level, and Raman photon is released.

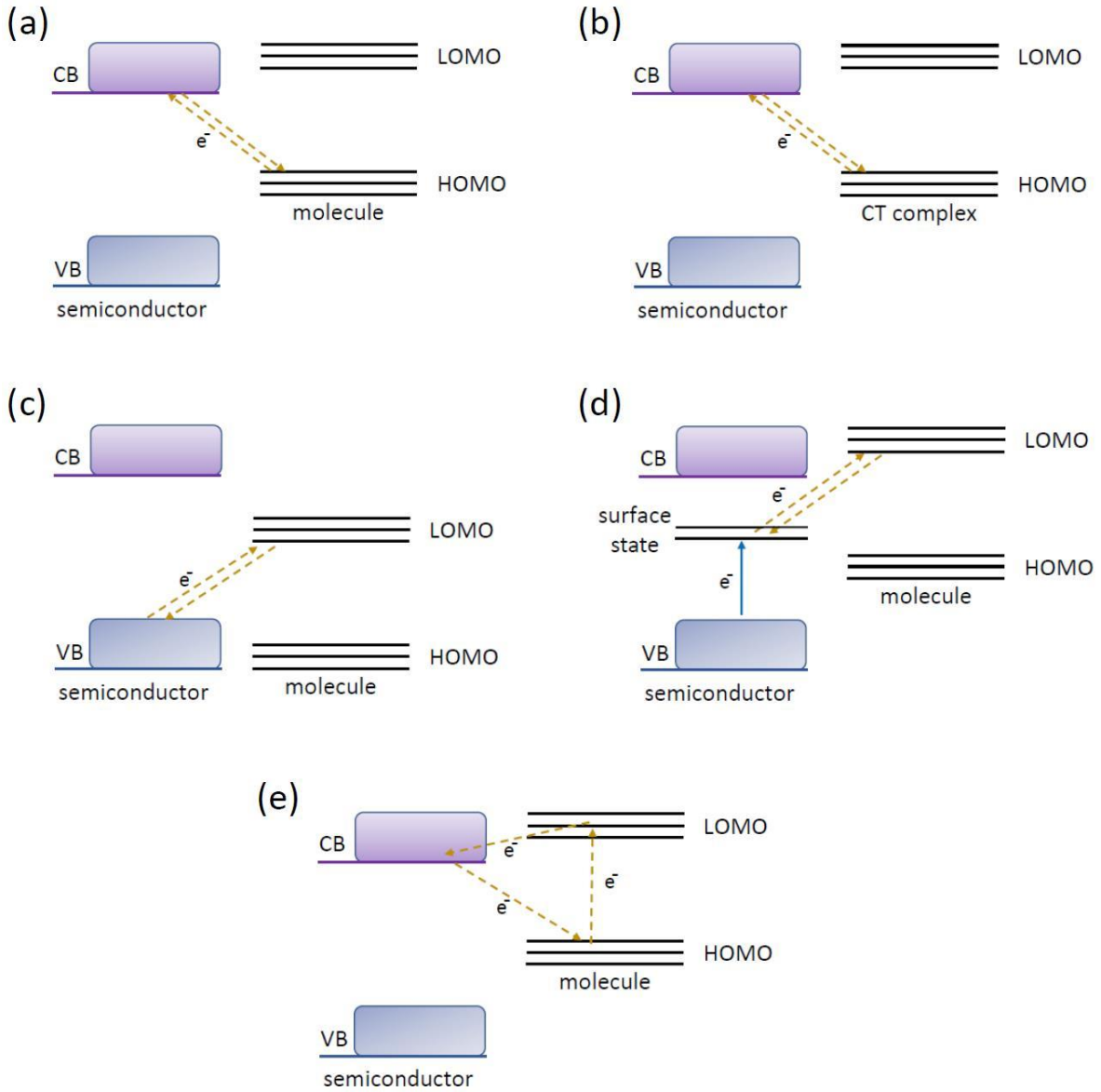

Figure 1.9 The charge transfer pathways in semiconductor-molecule systems (a) molecule HOMO-to-CB, (b) Charge transfer complex-to-CB, (c) VB-to-molecule LOMO, (d) Surface state-to-molecule LOMO and (e) CB-to-molecule LOMO. Based on Ref.[97]

Application of SERS on semiconductors

Yang *et al*. fabricated TiO_2 NPs with different crystallinity by sol-hydrothermal method and used them as SERS substrate for detection of ciprofloxacin (CIP) drug molecules (Figure 1.10).[105] In their study, it has been shown that crystallinity, pH value of the adsorption solution and adsorption time have important effects on the interaction and SERS behavior of CIP molecules and TiO_2 NPs. The enhancement was attributed to the contribution of the TiO_2-to-molecule CT mechanism.

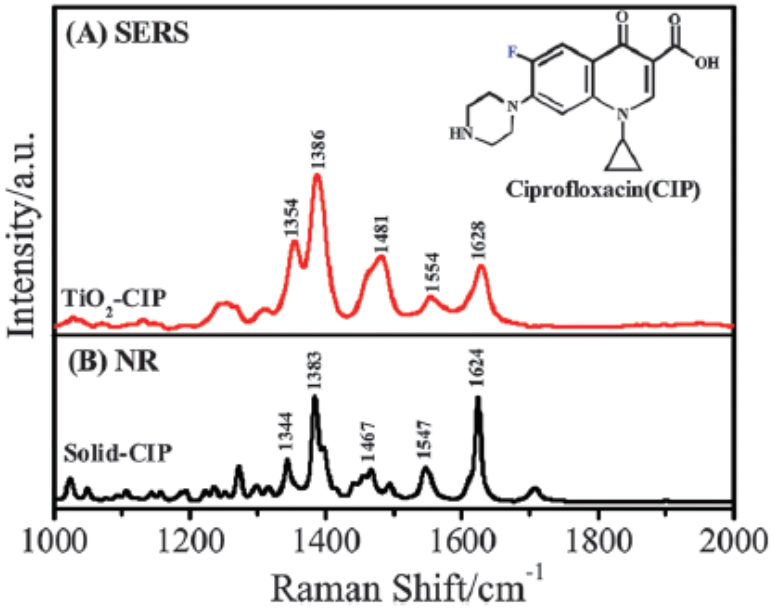

Figure 1.10 SERS spectrum of ciprofloxacin adsorbed on TiO_2 NPs and normal Raman spectrum of the solid ciprofloxacin powder. Adapted from Ref.[105]

Xue *et al*. fabricated a TiO_2/4-mercaptopyridine (4-MPy)/Ag sandwich structure and showed that SERS signal of the 4-MPy is significantly enhanced relative to those observed on 4 -MPy adsorbed on Ag NPs or TiO_2 NPs (Figure 1.11).[106] It was described that 4-MPy molecules form a bridge between TiO_2 and Ag NPs, promoting the charge-transfer and subsequently leading to the SERS signal enhancement.

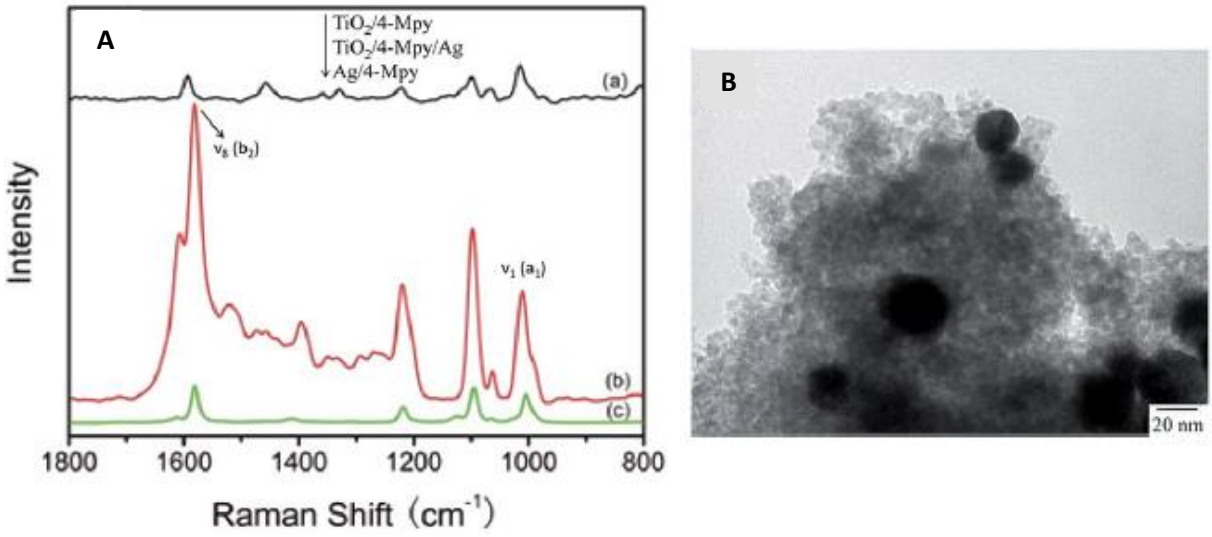

Figure 1.11 (A) SERS spectra of 4-MPy on (a) TiO2 NPs (b) TiO_2/4-MPy/Ag assemblies and (c) Ag colloids. (B) TEM image of the TiO_2/4-MPy/Ag assemblies. Adapted from Ref.[106]

1.6.3 Excitation resonance

When the wavelength of the excitation laser matches an internal electronic transition of the adsorbed molecule, there is an extra enhancement of the Raman signal because of the resonance Raman phenomenon. This phenomenon combines both SERS and resonance Raman, which is called surface-enhanced resonance Raman scattering (SERRS). The resonance enhancement can provide 2-3 order of magnitude of additional enhancement compared to SERS alone. It is required that the target molecule has a visible chromophore and the adsorption of the visible chromophore matches with the laser excitation.[107] SERRS has been implemented to detect single molecule-fluorescent dyes like rhodamine 6G and crystal violet.[72,108] SERRS can help to detect different Raman inactive molecules such as pesticides that SERS alone is unable to detect them because the electromagnetic enhancement is not high enough to enhance such Raman inactive molecules. Most effective application of SERRS has been in using naturally occurring chromophores to investigate in situ changes to proteins and enzymes.[89,109] SERRS has been effectively implemented in forensic sciences to determine the dyes in inks on paper and fibers.[110,111] SERRS is very sensitive and provides molecularly specific spectra that can be identified in mixtures of products.

1.7 Factors influencing the application of SERS for Analysis of NP

Despite the increasing number of SERS applications in different fields like environmental pollutants detection, food chemistry and forensic science, reproducibility of measurements and consistent enhancement is the main limitation of this method.[112–116] Different factors can impact the performance of SERS for analysis of NP. Different factors like type and size of the NP, morphology, aggregation, temperature, solution pH and so on can influence the SERS performance.[117–119] These factors are summarized in Figure 1.12. Some of these factors are explained shortly here:

1.7.1 Type of NP material

Based on the SERS enhancement mechanism, the noble metal nanoparticles like AgNPs, AuNPs, CuNPs and PtNPs support the electromagnetic enhancement which can significantly enhance the Raman signal of the coating agent. Semiconductor materials like TiO_2 and ZnO support the chemical enhancement.[79] In this case, the chemical bond between the chemical

agent and NP is necessary to reach the enhancement.[86] Additional to SERS peaks obtained from the coating agent, the intrinsic Raman peaks of the NPs (e.g. TiO_2) can be used to gain information about the material composition and crystal structure.

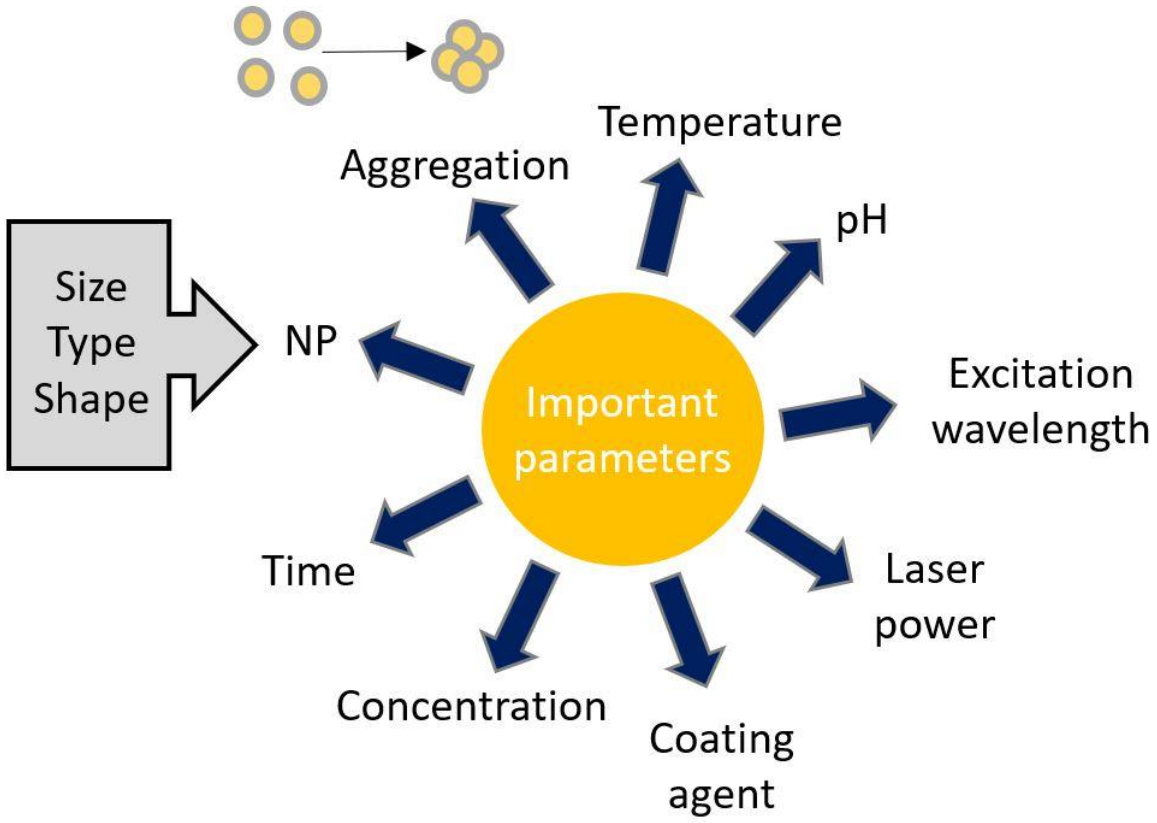

Figure 1.12 parameters needed to be considered for optimizing a system for achieving the best SERS response.

1.7.2 NP size

In general, noble metal NPs within a size range of 10-200 nm, show SERS and NPs smaller than 10 nm or bigger than 200 nm show very weak or no Raman signal.[113,120,121] Noble metal NPs with a size range of 10-100 nm show an optimal SERS.[113,121,122] It is related to size-dependent excitation of dipolar plasmon resonance as the major type of LSPR responsible for the electromagnetic enhancement in noble metal NPS. Different studies have shown that consumer products mostly contain noble metal NPs larger than 20 nm, which is in the detection range for SERS.[123–126]

For semiconductors, the NP size also plays a role in chemical enhancement. Several studies have shown the size dependency of SERS signal to the size of the semiconductor NPs.[79,82]

1.7.3 NP shape

NPs with different shapes show different enhancement factors. A study has shown that dogbone or cube shape AuNPs show a much higher enhancement factor than those in sphere or rod shape NPs.[127] It has been explained that surface structure and sharpness of NP structural feature can change the enhancement factor of the differently shaped NPs.[117]

1.7.4 Surface chemistry

Knowledge of the surface chemistry of the NPs plays an important role in the SERS enhancement factor. Analytes which have a high binding affinity with the target NP and sensitive SERS response, show the highest enhancement cause the matrix interference can be minimized.[128,129] A study has shown that pesticide ferbam is the most useful indicator to detect citrate coated AgNPs through competition with six other sample molecules[128]. Another study has investigated the adsorption of three types of flavonoids on TiO_2 NPs and has shown that myricetin has the highest binding affinity to TiO_2 NPs.[129] The chemical and physical properties of the NPs and also the coating molecule such as functional groups and surface charge are the important factors affecting the surface chemistry.[130–133] Besides, surrounding media like pH is another factor which has a significant impact on the enhancement.[131–133] For example, molecules containing thiol groups have a high affinity to noble metal NPs.[130]

1.7.5 Spatial arrangement

It is believed that significant SERS enhancement occurs when the molecule enters within gaps between NP aggregates smaller than 10 nm. This spatially much localized volume that shows extremely high electric field enhancement are typically referred to as “hot-spots” which can significantly enhance the Raman signal.[134] Due to the importance of hotspot on the performance of SERS, many studies have been focusing on this topic.[135,136] In colloidal systems, hotspots can be created by aggregation. Adding salts can induce aggregation by changing the surface chemistry of NPs and generating hotspots due to more particle-particle interactions for SERS enhancement.[137,138] The tendency of the NPs for aggregation is dependent on different factors such as shape, size, chemical composition and surface chemistry of the

NPs.[139] On the other side, small molecules can easily enter the hotspots and show a higher enhancement in comparison with big molecules.

1.7.6 Laser excitation wavelength

Laser excitation wavelength affects the experiment and should be selected to maximize scattering efficiencies and minimize the fluorescence from the sample at the same time. Visible excitation lasers (e.g. 488 nm, 514 nm, 532 nm and 633 nm) are typically used for the measurements, but other excitation wavelengths from the UV (325 nm) as well as near IR (785 nm or 830 nm) are also implemented for the measurements.[140–143]

1.8 Characterization of NPs in environmental samples

SERS can effectively identify NPs from their dissolved ions or bulk material due to the enhanced Raman signal from the binding molecule to the NPs. For example, SERS has been used to differentiate AgNPs from AgCl and $AgNO_3$ due to the NPs induced enhancement of ferbam molecule.[113] SERS has been used to demonstrate the *in situ* distribution and penetration of AuNPs on plant leaves.[144] Selection of appropriate molecule with a high binding ability plays a vital role in investigating NPs in real environmental samples to reduce the interference of the matrix. The type and amount of the molecule can differ depending on the NP type and matrix in which the NP is detected.[128,145] Different methods such as filtration or centrifugation combined with SERS can be implemented to enrich the NPs from the matrix. For example, centrifugation, combined with SERS, has been implemented to detect AgNPs in different media like environmental water, spinach juice or antimicrobial products[113,128]. In antimicrobial products, the matrices can influence the sensitivity of SERS, and therefore this problem was tried to be solved by implementation of coupled filtration method to detect AgNPs with a concentration limit of 0.005 mg L^{-1}.[146] Using such a system has the advantage of analyzing samples with high volume, but biological particles can clog the system during filtration of complex samples.

Zhao et al. used a method to identify and discriminate rutile and anatase TiO_2 NPs based on their Raman signatures.[147] The concentration of the TiO_2 NPs was determined based on the Raman peak intensity. In their study, the particle size was determined based on the ratio between the Raman intensity of the TiO_2 NPs and the SERS intensity of myricetin bound to the

NPs. The implemented approach has been suggested for monitoring and risk assessment of TiO_2 NPs in foods, consumable products as well as in environmental samples.

1.9 Investigation of fate of NPs

Due to large specific surface area and high activity, NPs show different transformations during their release, transport and distribution in the environment. NPs are usually stabilized by coating with different materials (e.g. citrate, PVP) to avoid dissolution or aggregation. For example, AgNPs can oxidize and release Ag^+ in water. Also, sulfidation and chlorination of the AgNps can occur if the system contains HS^- or Cl^-.[148,149]. NPs can interact with dissolved organic substances in water and attach to the soil matrix. It has been shown that sorption of natural organic agents such as fulvic acid, Humic acid and Suwannee River Humic Acid to AgNPs increase the stability of the NPs. The interaction of NPs and their coatings such as formation of natural coating around NPs or development of multilayer coatings plays a vital role in determining the fate, stability and toxicity of NPs in the environment.

Several studies have investigated the effect of aggregation on the SERS spectra of different molecules. Bell and Mccourt showed that the SERS signal of thiophenol increased first and then reached a plateau with increasing concentrations of $MgSO_4$ as salt to induce homo aggregation of AuNPs.[150]

In our group, SERS has been used to investigate and characterize the adsorption of natural organic matter on AgNPs under environmentally relevant conditions.[67] The results showed that humic acid (HA) binds very strongly to the AgNPs, and the coating cannot be detached by multiple washing steps, including centrifugation and resuspension. In addition, aged AgNPs in river water and soil solution were detected by SERS, and it was found that AgNPs were naturally coated with HA. Another research group has addressed the pH dependency of the interaction between HA and AgNPs and showing different SERS signal intensity.[151] Sanchez-Cortes studied the interaction of the herbicide paraquat (PQ) with HA extracted from modified soils and their adsorption on AgNPs.[152] Both of the agents were successfully detected using 514.5 nm and 1064 nm excitation wavelength. SERS could observe the structural changes of HA and PQ due to presence of each other on AgNPs.

In general, SERS can be a useful method to improve our understanding of the transformation and surface chemistry of NPs in presence of organic molecules in the surrounding. Also, SERS

can help to analyze the interaction of organic compounds with NPs to enhance the knowledge about the role of NPs in changing the environmental fate of organic contaminants.

2 Experimental section

2.1 Chemicals and other Materials

2.1.1 Chemicals

The following chemicals and solvents were used without further purification if not otherwise stated.

1-Hexanol ($C_6H_{14}O$, Merck, Darmstadt, Germany)

4-Mercaptobenzoic acid (4-MBA, Sigma-Aldrich, St. Louis, USA)

4-Mercaptopyridine (4-MPy, Sigma-Aldrich, Japan)

Cadmium standard solution ($Cd(NO_3)_2.4H_2O$ in HNO_3 0.5 mol/l, Fluka, Buchs, Switzerland)

Calcium standard solution ($Ca(NO_3)_2$ in HNO_3 0.5 mol/l, Merck, Darmstadt, Germany)

Chloroauric acid ($HAuCl_4$, 0.01% w/w, Sigma-Aldrich, St. Louis, USA)

Copper standard solution ($Cu(NO_3)_2$ in HNO_3 0.5 mol/l, Merck, Darmstadt, Germany)

Ethylene glycol ($C_2H_6O_2$, Merck, Darmstadt, Germany)

Hydrogen peroxide (H_2O_2, 30%, Merck, Darmstadt, Germany)

Iron standard solution ($Fe(NO_3)_2$ in HNO_3 0.5 ml/l, Fluka, Buchs, Switzerland)

Mercury standard solution ($Hg(NO_3)_2.H_2O$ in HNO_3 0.5 mol/l, Fluka, Buchs, Switzerland)

Polydiallyldimethylammonium chloride solution (PDDA, 0.5%, Sigma-Aldrich, St. Louis, USA)

Silver nitrate ($AgNO_3$, Merck, Darmstadt, Germany)

SolantineBrown BRL (C.I. Direct Brown, Isfahan, Iran)

Sulfuric acid (H_2SO_4, 98%, Fluka Analytical, Seelze, Germany)

Suwannee River Natural Organic Matter (SRNOM, IHSS, St. Paul, USA)

Trisodium citrate dihydrate ($C_6H_5Na_3O_7$ * 2 H_2O, 1% w/w, Merck, Darmstadt, Germany)

Zinc acetate dihydrate ($Zn(CH_3COO)_2{\cdot}2H_2O$, Merck, Darmstadt, Germany)

Zinc standard solution ($Zn(NO_3)_2$ in HNO_3 0.5 mol/l, Merck, Darmstadt, Germany)

2.1.2 Biochemicals

E. coli PTCC 1399 was provided by Department of Chemistry, Shahreza Branch, Islamic Azad University, Isfahan, Iran.

Nutrient agar medium, Merck, Germany.

Nutrient broth medium (NB), Merck, Germany.

Staphylococcus aureus PTCC 1112 was provided by Department of Microbiology, Falavarjan Branch, Islamic Azad University, Isfahan, Iran.

2.2 Instruments and devices

Product	Company	Model
Autoclave	Made in Iran	-
Centrifuge	Eppendorf	5804 R
Cuvette (Uv-vis)	Carl Roth GmbH	Rotalibo®, PMMA
Dynamic light scattering (DLS)	Beckman Coulter	Delsa Nano C
EDX	Bruker	Xflash® 6| 60
Furnace	Heraeus	-
Incubator	Made in Iran	-
Pipette	Eppendorf	Research Vari 100-1000 µL
Pipette	Eppendorf	Research Vari 500-5000 µL
Pipette	VWR	Research Vari 10-100 µL
Pipette	VWR	Research Vari 1-10 µL
Raman microscope	HORIBA scientific	LabRAM HR
Scales	Mettler	PB3000 Delta Range
Scanning Electron Microscope	Carl Zeiss	Sigma VP 300
Scanning Electron Microscope	Philips	XL30
Transmission Electron Microscope	JEOL	JEM-1400
Ultrapure water purification system	Merck	QPAK ®1
Ultrasonic bath	Bandelin Sonorex	Typ RK 510
UV-vis Spectrophotometer	Shimadzu	MPC-2200
UV-vis Spectroscopy	Analytic Jena	SPECORD® 250 PLUS
X-ray power diffraction (XRD)	Bruker	D8 ADVANCE XRD
8 W UV lamps	Philips	UV-A

2.3 List of Experiments

2.3.1 Synthesis and characterization of Au@Ag NPs

Citrate reduced Au@Ag core-shell nanoparticles were synthesized following a similar procedure of Song et al.[153] 50 ml 0.01% (w/w) $HAuCl_4$ was mixed and reduced with 750 µl 1% (w/w) sodium citrate solution and heated at 100°C for 20 mins under magnetic stirring until the color of the solution changed from colorless to wine red. The synthesized Au nanoparticles were used as seed particles for preparation of Au@Ag core-shell nanoparticles. 290 µl 0.5 % (w/w) $AgNO_3$ was added to the 50 ml boiling Au nanoparticle solution. Finally, 0.5 ml 1% (w/w) sodium citrate solution was slowly added to the stirring solution and heated at 100°C for 1 hour, and heating was stopped and cooled down to room temperature for 2 hours. The color of the final solution was red/orange.

UV-vis absorbance spectra, scanning electron microscopy (SEM) coupled with Energy-dispersive X-ray spectroscopy (EDX) and transmission electron microscopy (TEM) were obtained to confirm the successful synthesis of the core-shell nanoparticles. Dynamic light scattering (DLS) was implemented to measure the hydrodynamic size of the nanoparticles. The size and morphology of the nanoparticles were characterized by using a SEM. EDX measurements were conducted to understand the composition of the synthesized nanoparticles. Nanoparticles were additionally characterized by TEM with an acceleration voltage of 120kV. ICP-MS measurements were conducted at the institute for environmental sciences at the University of Koblenz-Landau to evaluate the concentration of Au and Ag. For UV-vis measurements, nanoparticle colloid solutions were measured in semi-micro PMMA-cuvette. Deionized water was measured as a reference spectrum for UV-vis measurements.

2.3.2 Au@Ag NPs SERS measurements

Suwannee River Natural Organic Matter (SRNOM), 4-mercaptobenzoic acid (4-MBA) and 4-mercaptopyridine (4-MPy) were selected as sample molecules for the experiments. The chemical structure of 4-MBA and 4-MPy is shown in Figure 2.1. For optimising SERS measurements for separate 4-MBA, 4-MPy and SRNOM coatings, the Au@Ag suspension was added to coating solutions in equal parts with a final concentration of 10^{-5} molar and equilibrated for 2 hours on an overhead shaker. SRNOM had a final concentration of 20mg/l.

Afterwards, samples were washed twice via centrifugation for 15 min and re-suspended in deionized water after removing the supernatant. The samples were also treated in an ultrasonic bath for 10 min to avoid the formation of aggregates. The samples were kept in a water bath filled with ice to avoid thermal damage to NOM. Finally, 10 µl of the solution was placed on a silicon wafer to dry for SERS measurements.

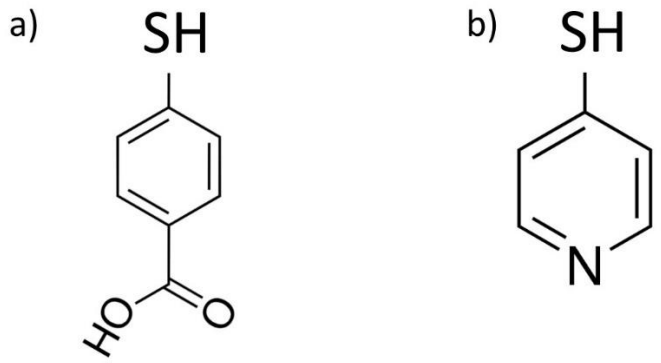

Figure 2.2 Chemical structure of 4-MBA (a) and 4-MPy (b).

Two of the mentioned coating agents were mixed together to simulate competition of coating agents, and the Au@Ag suspension was added in equal parts to them. After shaking for 2 hours on overhead shaker the samples were washed for two times as described above.

To simulate coating agents' replacement, the NPs were coated with SRNOM for 24 hours on an overhead shaker to ensure the coating. Consequently, 4-MBA or 4-MPy with a final concentration of 10^{-5} mol/l was added and the solutions were shaking for 2 hours before washing steps.

SERS spectra were recorded by the Raman microscope using a He-Ne laser (633 nm) with 3.4 mW laser power at the sample. A 50× objective (numerical aperture, NA = 0.75) was used with acquisition times of 2 s, 5 s or 10 s. Replicate of each sample was made three times and spectra were obtained at least at five different points of each sample to verify the spectra's reproducibility. Baseline correction was performed to obtain the final spectrum.

2.3.3 Preparation of core-shell@Si

Silicon wafers were coated based on a method used by Li et al.[154] Silicon wafers were cut into 1 cm × 0.6 cm pieces and inserted for 10 minutes into a boiling solution prepared by mixing 30% H_2O_2 and 98% H_2SO_4 with a volume ratio of 3:7. Afterwards, the silicon wafers were rinsed with water several times. The hydroxyl covered silicon wafers were then inserted into 0.5 % PDDA solution for 30 minutes. Subsequently, they were rinsed again with water repeatedly to detach the PDDA physically attached to the silicon wafer and dried with nitrogen. Finally, the silicon wafers were immersed in Ag@Au suspension for 3 hours before drying with nitrogen. The prepared substrates were stored in sealed tubes temporarily for further experiments. Figure 2.3 shows the schematic illustration for preparation of Au@Ag coated silicon wafers as SERS substrate.

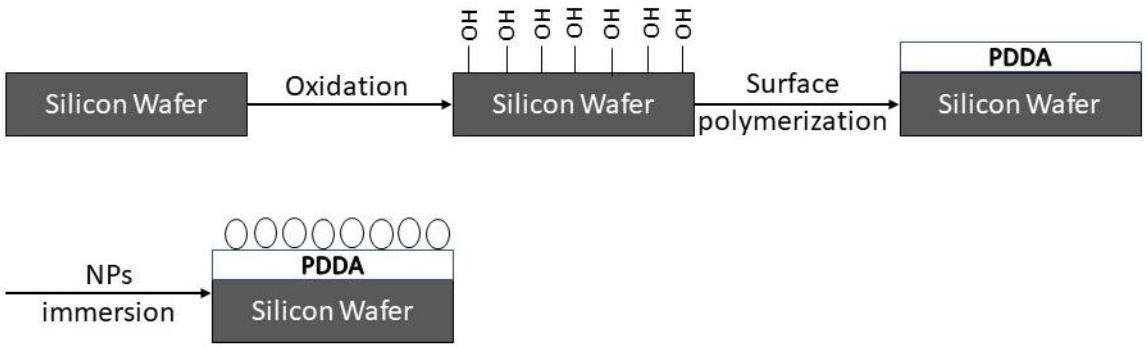

Figure 2.3 Schematic illustration for preparation of Au@Ag coated silicon wafer as SERS substrate.

Oxidation of silicon wafers leads to the formation of negatively charged hydroxyl groups on the surface which can bind to positively charged polymers like PDDA. The Ag@Au Core-shell nanoparticles are negatively charged and can bind to the positively charged silicon wafer.

2.3.4 Detection of chemicals and TiO_2 coating by core-shell @ Si

The prepared Au@Ag coated silicon wafer was soaked in sample solution of 4-MBA and 4-MPy with concentrations of 5 x 10^{-9} up to 5 x 10^{-6} for two hours. The dilutions were prepared by Milli-Q water. In a set of experiments, tap water and snowmelt water were also used to dilute

4-MPy to see if the coated silicon wafer can also be used to detect chemicals in more complex aqueous environments. After soaking, the sample was dried and measured with the Raman microscope.

For the indirect SERS measurement of the TiO_2 coating by the Au@Ag coated silicon wafer, unmodified TiO_2 NPs were diluted in a solution of 4-Mpy (1×10^{-5} M) with a concentration of 50 mg/l and the solution was placed on a shaker for two hours before the shaking was stopped. Afterwards, the samples were washed with Milli-Q water and centrifuged three times. Finally, the solution of 4-MPy coated TiO_2 NPs was diluted 100 times with Milli-Q water and was deposited on top of the Au@Ag coated silicon wafer and was dried before the SERS measurements.

2.3.5 Modification and characterization of TiO_2 NPs

TiO_2 P25 (Degussa) was thermally modified based on a method used by Khoa Le et al. with some changes as following:[155]

TiO_2 was washed with double distilled water and dried at 80 °C in the air. Afterwards, this powder was put in an alumina crucible and placed into a high temperature furnace at different temperatures of 500, 650, 800 and 950°C for 5 minutes. Subsequently, the samples were taken out of the oven and cooled down to the room temperature and finally grounded to achieve the final required powder sample. The samples were labelled with the used modification temperature.

To determine the crystal structure of TiO_2 powders, XRD experiments were performed on a XRD diffraction spectrometer with a Cu Kα line at 1.5406 Å and a Ni filter for an angle range of 2θ =20-80°. The samples' surface morphology was investigated using a SEM, and the electronic absorption spectra were recorded on a UV-vis spectrometer. Raman spectra of the samples were obtained by the Raman microscope employing a He-Ne 633 nm laser with a 50× objective and an acquisition time of 1 s. The surface area of the samples was measured by BET method.

2.3.6 Direct SERS measurement of TiO_2 coating

20 mg of modified TiO_2 NPs at different temperatures were dissolved in 10 mL of 4-MBA (10^{-3} M) ethanol solution. The mixture was stirred for 2 hours, and the stirring was stopped. After two times of washing with purified water and centrifugation, the nanoparticles were dried. Raman spectra were obtained using a 514.5 nm laser.

2.3.7 Antibacterial Experiment

The antibacterial activity of the thermally modified TiO_2 NPs was investigated by the bacterium as per colony count method for gram-positive and gram-negative bacteria. Utilizing Nutrient broth medium (NB), different TiO_2 NPs with a concentration of 200 ppm were applied to *Escherichia coli* and *Staphylococcus aureus* as model microorganisms. The TiO_2 NPs were introduced into 10 ml NB, which was supplied with 200 µl bacteria at an initial concentration of 1.5 $\times 10^5$ CFU (colony forming unit). Also, a medium without nanoparticles as control was prepared and grown under the same reaction conditions. All the samples were illuminated with four 8 W lamps (Philips UV-A, λ_{max} =365 nm), at room temperature for different time intervals of 20 mins for the period of 260 mins. During the experiment, the sample containers were placed horizontally on a shaker platform and were agitated at a speed of 200 rpm. By using a water circulation through the reactor, the temperature of the culture medium was controlled. After sampling, the nanoparticles were separated by centrifugation, and 100 µl of each bacteria suspension was dispersed on the Nutrient Agar medium. The samples on Nutrient Agar medium were incubated for 24 hours at 37°C. The results shown are the average data obtained from triplicate runs. The result of the CFU counting in nanoparticle free medium showed a negligible decrease in CFU, which shows that the photochemical inactivation was negligible under UV-A irradiation with low energy.

2.3.8 Synthesis and characterization of ZnO NPs

According to a method reported in the literature, the ZnO nanoparticles were prepared in a cooperation with Islamic Azad University of Shahreza in Iran. Briefly, 5.60 g of $Zn(CH_3COO)_2 \cdot 2H_2O$ was dissolved into 50 ml of water, 1-hexanol, ethylene glycol, and kept under continuous stirring. In the case of water as solvent, 10 ml NaOH was added dropwise into the solution until a transparent solution was obtained. After vigorous stirring at 60 ◦C for

30 min, the mixture was then moved into a sealed Teflon-lined autoclave and kept at 170 ˚C for 18 h. Subsequently, after the autoclave was cooled, the obtained white powder was collected and washed with pure ethanol and distilled water and finally dried under vacuum at 90 ˚C.

To characterize the structure of the ZnO powders, X-ray powder diffraction (XRD) experiments were performed using a XRD diffraction spectrometer (Cu Kα, λ=1.5406 Å) with a Ni filter for an angle range of 2θ = 20–80^0. SEM measurements were also carried out to characterize the samples' morphology with an accelerating voltage of 17 kV. The samples' optical properties were investigated by a UV-vis spectrophotometer over the range of 350–600 nm at a resolution of 2.0 nm.

2.3.9 Photodegradation of sample azo dye

All the experiments with ZnO NPs were conducted on 100 mL of azo solution in a cylinder quartz vessel, and four 8 W UV lamps (Philips UV-C, l = 365 nm) were employed as the light source in photocatalytic process. The distance between the UV lamps and solution was 12 cm. The experiments were carried out at the temperature of 25±2 ˚C and magnetically stirred and equilibrated in the dark for 20min after the addition of photocatalysts. During the experiment, the test solution in the vessel was stirred continuously. 5 milliliter samples were withdrawn at intervals of 15min for two continuous hours and were then centrifuged at 4000 rpm for 10 min so that ZnO nanoparticles were removed. The photocatalytic reduction efficiency was monitored by measuring the absorbance at 435 nm with a spectrophotometer.

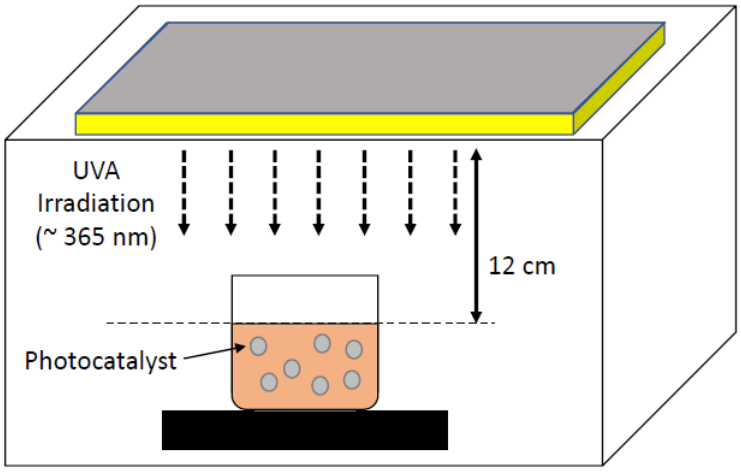

Figure 2.1 schematic setup of the Azo dye degradation by different ZnO photocatalysts.

3 Results and discussion

3.1. SERS measurement of coatings on Au@Ag nanoparticles

The results presented in section 3.1. were published in the publication “Characterization of coatings on metallic nanoparticles by surface-enhanced Raman scattering (SERS) for environmental purposes” by S. Amininejad, N. P. Ivleva and T. Baumann in the “Vadose Zone Journal”.

3.1.1 Characterization of Au@Ag core-shell nanoparticles

In order to confirm the successful synthesis of the Au@Ag nanoparticles, SEM and TEM images were obtained. The images show uniform spheres with an approximate size of 35 nm (Figure 3.1).

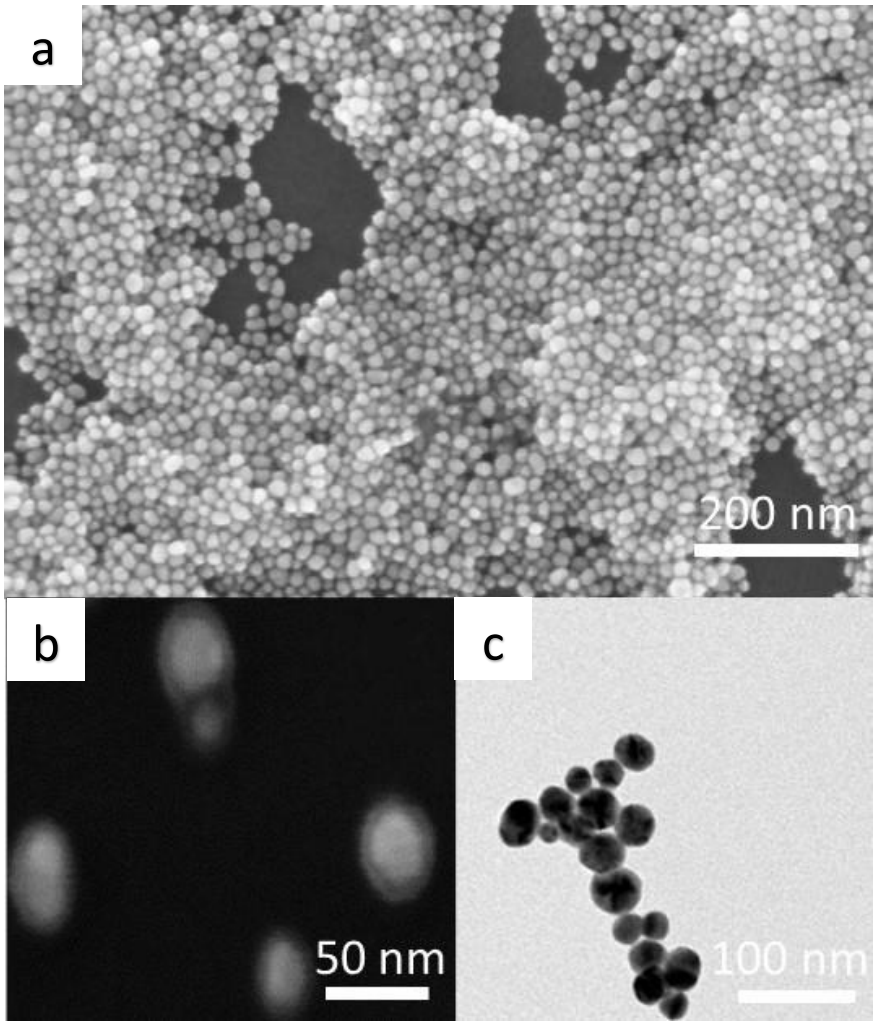

Figure 3.1 Scanning electron microscope (SEM) image of prepared Au@Ag nanoparticles (a), (b) and transmission emission microscope (TEM) image of Au@Ag nanoparticles (c).[156]

The results are in agreement with DLS measurements which reveal an approximate diameter of 33 nm. The result of the EDX analyses shows the presence of gold and silver in the elemental composition of the synthesized nanoparticles. The spectrum contains two peaks which are assigned to Au and Ag (Figure 3.2).

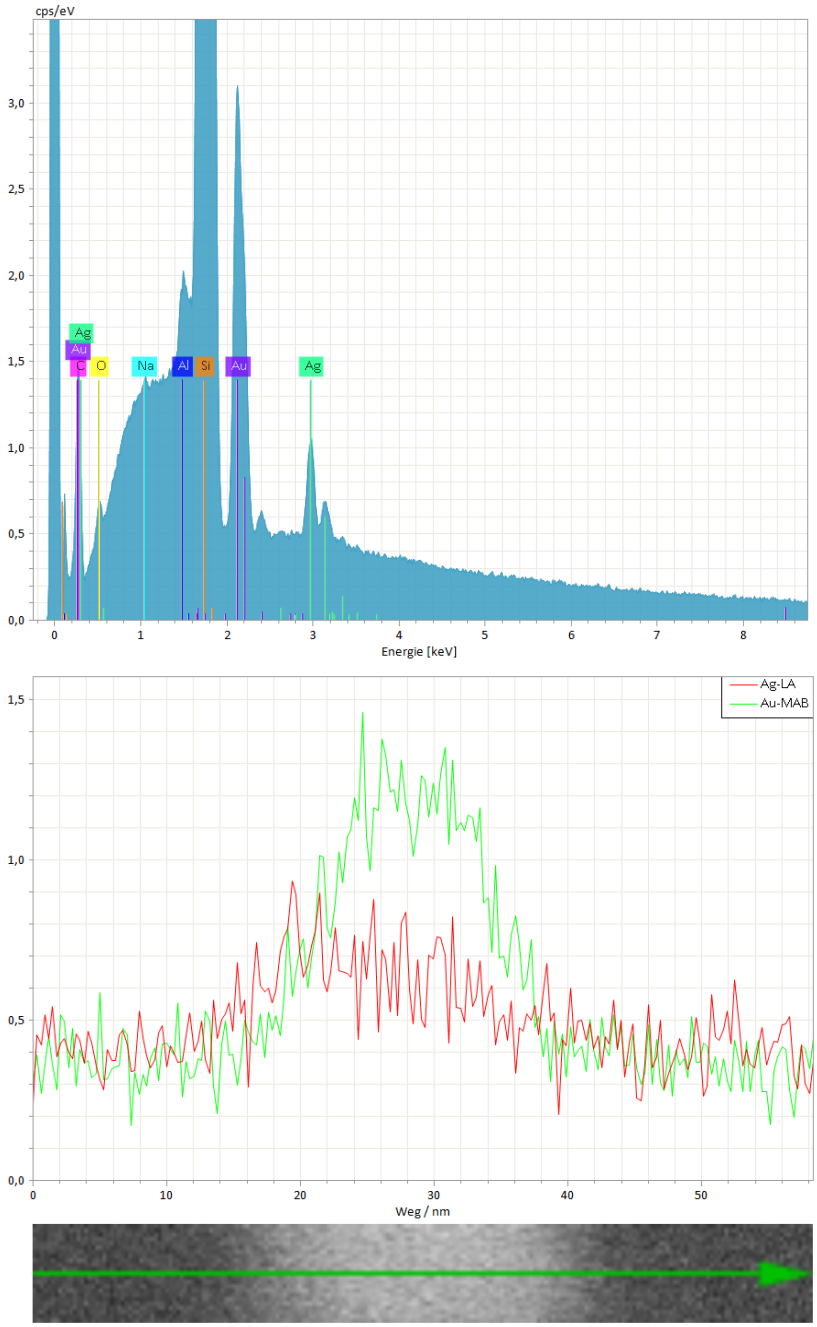

Figure 3.2 Energy Dispersive X-Ray Analysis (EDX) of as-prepared Au@Ag nanoparticles.[156]

The UV-vis spectrum of gold nanoparticles shows a peak at 520 nm, which is in the adsorption peak region for gold. The UV-vis spectrum peak for Au@Ag core-shell nanoparticles shows a blue-shift compared with the absorption peak of Au NPs, which indicates the effective coating of Au NP seeds with silver. Both UV-vis spectra show narrow peaks, which is indicative of relative monodisperse Au@Ag suspension (Figure 3.3).

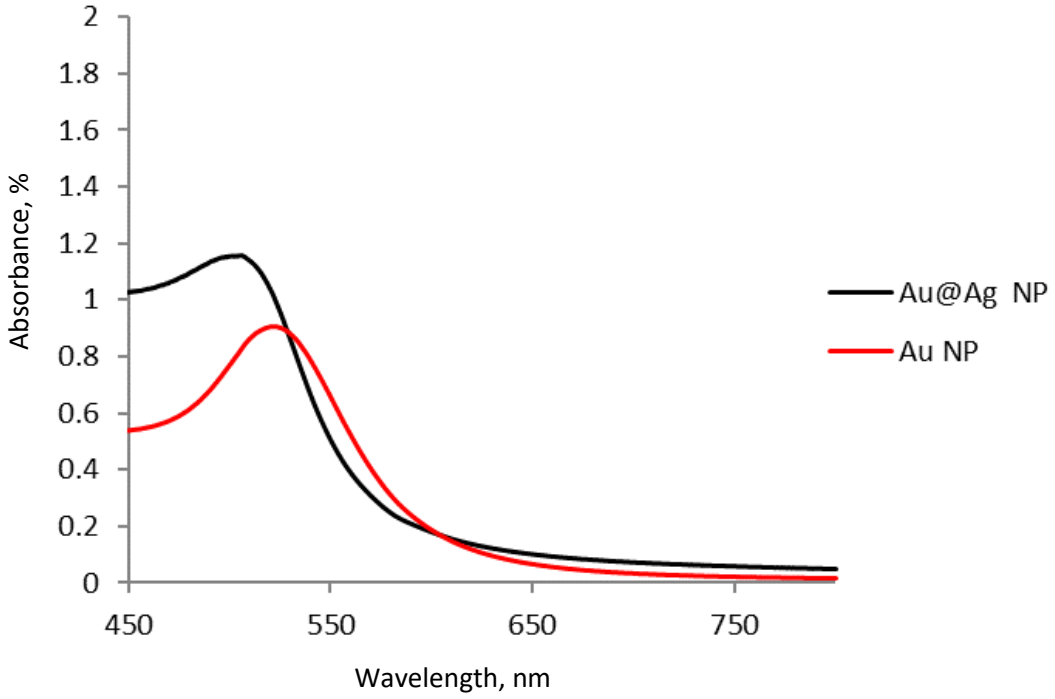

Figure 3.3 UV-vis spectra of Au@Ag and Au nanoparticles.[156]

The Au@Ag nanoparticles have a zeta potential value of -41 mV, which is less than -30 mV and therefore, the nanoparticles are considered to be stable.[157] The results prove the successful synthesis of core-shell nanoparticles.

To evaluate the stability of the synthesized Au@Ag NPs, UV-vis spectra of the aging NPs were taken for a period of 8 weeks with two-weeks time intervals. The results are demonstrated in figure 3.4 and as it can be seen the UV-vis spectra of the NPs are similar, and therefore the NPs are stable at least after eight weeks of aging. The slight decrease of the absorbance spectrum is caused by aggregation of NPs.[158]

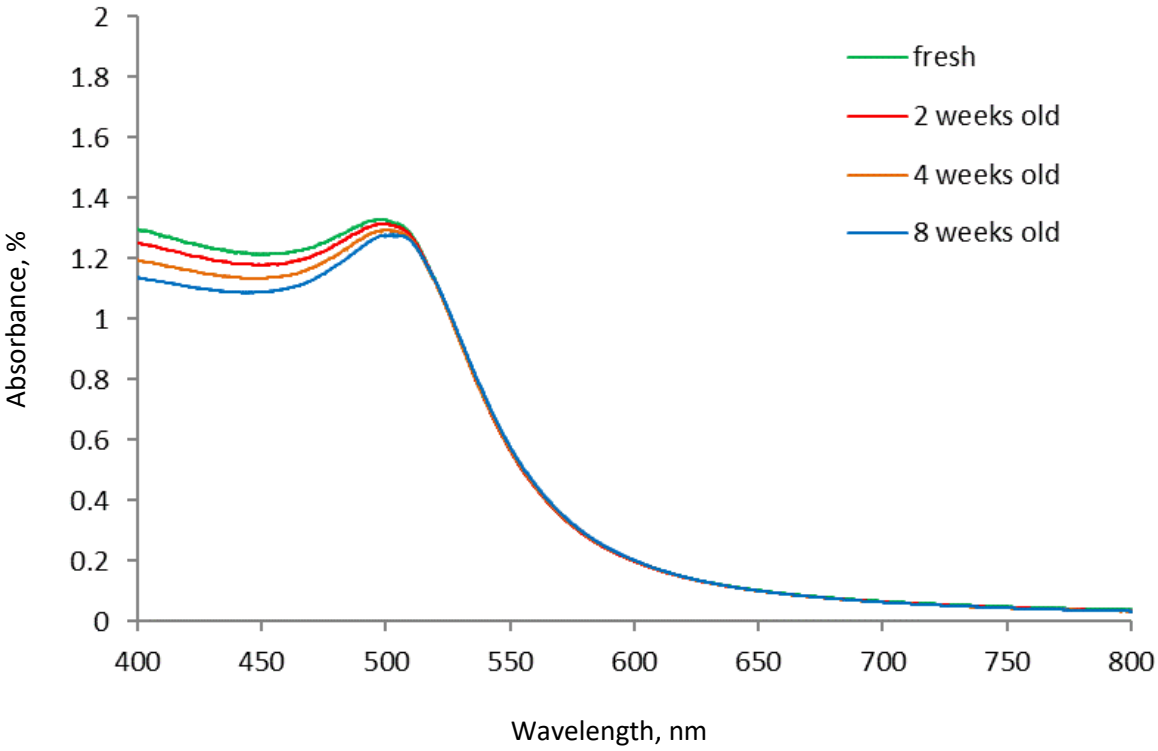

Figure 3.4 UV-vis spectra of Au@Ag NPs of different age

3.1.2 Optimization of SERS experimental parameters

To achieve reproducible SERS results as the main challenge for SERS analysis, the experimental parameters should be optimized at first. The optimum SERS conditions for different coating agents can be highly variable and, therefore, an optimum setup that fits for all of the coating agents should be implemented.[159]

Figure 3.5 shows the SERS spectra of selected coating agents on Au@Ag NPs after optimization of experimental parameters. SERS spectra of 4-MPy is dominated by characteristic peaks at about 711, 1006, 1063, 1097, 1223, 1580 and 1609 cm^{-1}. The band at 1097 cm^{-1} represents the covalent binding of sulfur to the Au@Ag as the result of the altered C-S bond on the ring vibrations. The peak around 711 cm^{-1} is indicative of the in-plane ring deformation with C-S. The bands at 1580 cm^{-1} and 1609 cm^{-1} indicate the ring stretch with nitrogen vibrations and the bands at 1063 cm^{-1} and 1223 cm^{-1} are assigned to in-plane C-H vibrations. Furthermore, the band at around 1006 cm^{-1} is assigned to the ring-breathing vibrations.[160,161] The two

Raman peaks at 1580 and 1609 cm^{-1} have also been attributed to N-deprotonation and N-protonation and therefore being used as a marker for the SERS-based pH sensors.

Two signals dominate the SERS spectra of 4-MBA at about 1585 cm^{-1} which arises from ν_{8a} aromatic-ring vibrations, and the band at about 1076 cm^{-1} which is assigned to ν_{12} aromatic-ring vibrations processing C-S stretching characteristics.[162] The band seen at about 1424 cm^{-1} is attributed to the symmetric stretching vibration of the carboxylate group, $\nu_s(COO^-)$.

Two features dominate SERS spectra of SRNOM at about 1355 cm^{-1} and 1575 cm^{-1}, which are referred to as G peak (graphite peak) and D peak (disordered peak) in carbon analysis. The G peak is assigned to in- plane band-stretching motion of pairs of sp^2 atoms. The D peak is assigned to the breathing mode of sixfold aromatic rings (E_{2g} symmetry).

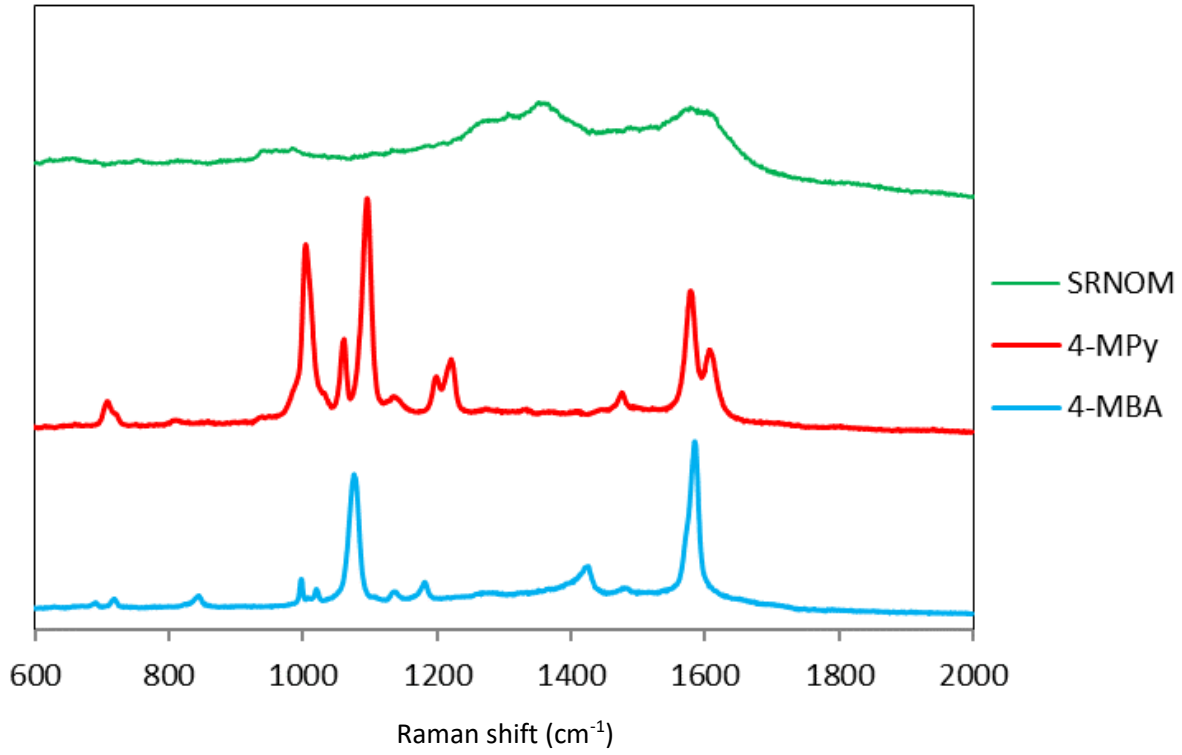

Figure 3.5 SERS spectra of selected coating agents on Au@Ag NPs.[156]

SRNOM coatings on Au@Ag NPs were detected in a concentration range from 0.5 to 50 mg/L (Figure 3.6). Environmental concentrations of humic substances are about 0.5-4.0 mg/L in river water and 0.5-40 mg/L in lakes.

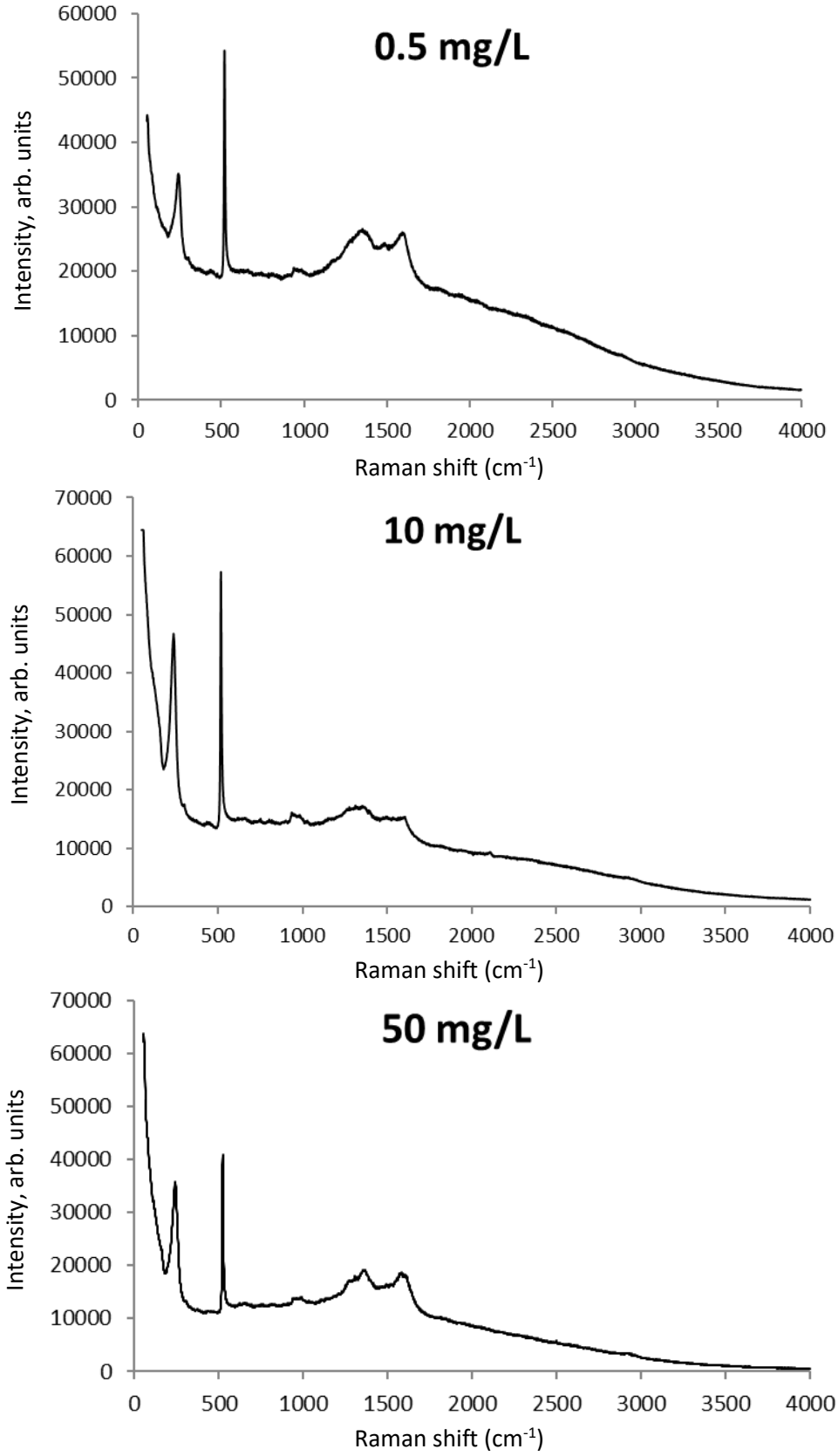

Figure 3.6 Characterization of different concentrations of SRNOM coating (0.5 mg/L, 10 mg/L and 50 mg/L) on Au@Ag NP.

To confirm the effect of different nanoparticles on SERS enhancement, we have compared the different SERS signals of AuNPs as the core with final Au@Ag NPs. Figure 3.7 shows that Au@Ag nanoparticles exhibit a higher SERS enhancement factor than AuNPs.

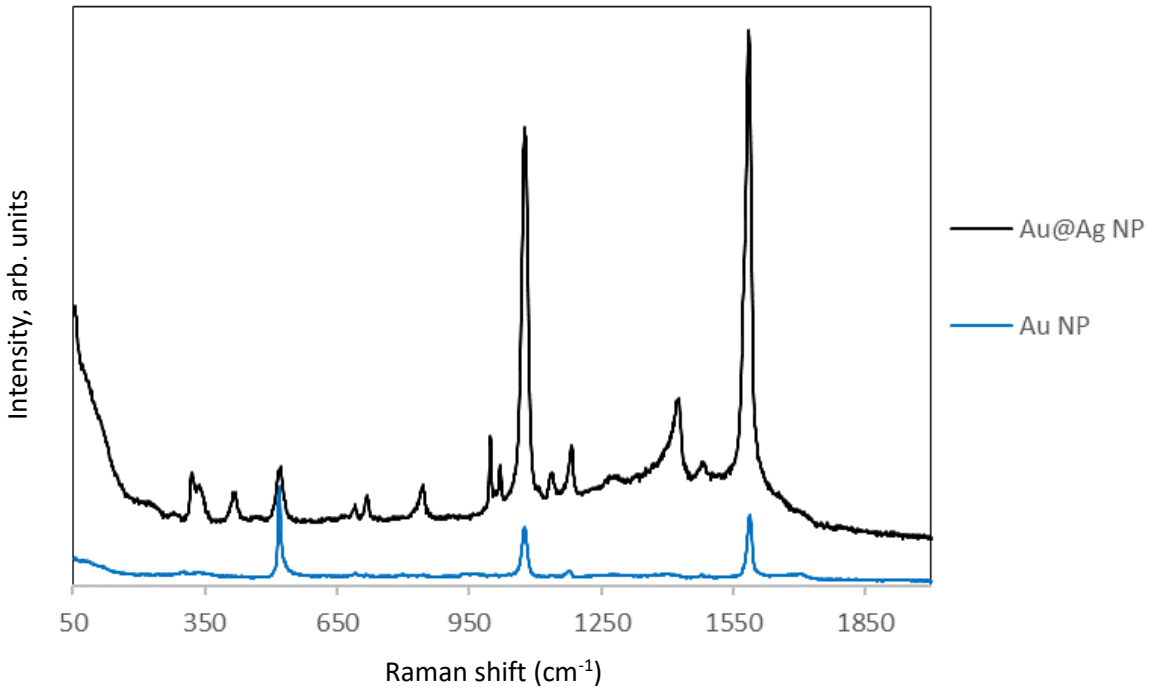

Figure 3.7 The SERS spectra of 4-MBA coated on the surface of Au NPs and Au@Ag NPs.

It has been reported that Ag nanoparticles generate stronger SERS intensities than Au nanoparticles of the same size[163]. However, synthesizing monodisperse Ag NPs is still challenging. From the other side, Au nanoparticles are more uniform[164,165]. Hence, Au@Ag nanoparticles are an effective solution to synthesize more monodisperse nanoparticles with high SERS enhancement.

The selection of proper laser wavelength is highly dependent on the application. Three different excitation wavelengths of 532 nm, 633 nm, and 785 nm have been tested to select the appropriate excitation wavelength. Figure 3.8 shows the recorded spectra of 4-MBA coated Au@Ag nanoparticles with these laser excitation wavelengths.

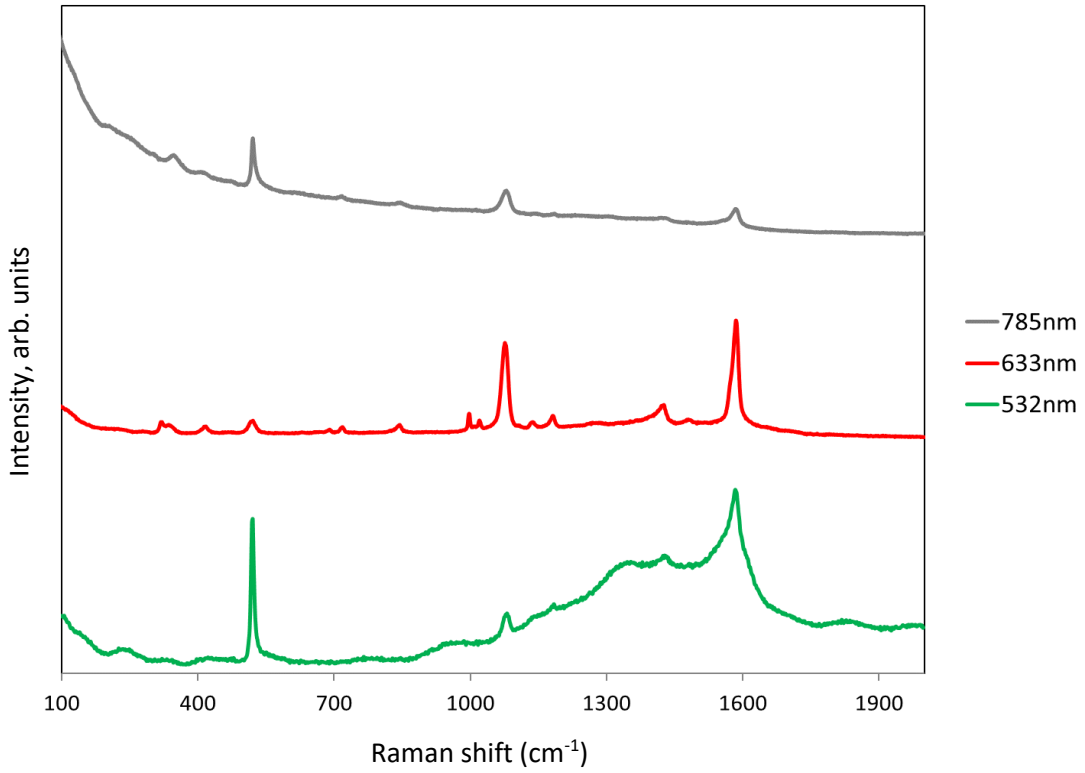

Figure 3.8 The SERS spectra of 4-MBA on the Surface of Au@Ag NPs with different excitation wavelengths.[156]

The use of a 532 nm excitation laser can lead to thermal decomposition of the NOM and the formation of amorphous C. The 633 nm laser provides a balance of high sensitivity and low fluorescence which is optimal for the experiments. The spectra obtained as excited with a 785 nm laser show lower SERS enhancement. Therefore, further experiments were conducted using a 633 nm laser.

Figure 3.9 shows the effect of size of NPs aggregates on the SERS spectra of the 4-MPy coated Au@Ag NPs. With increasing the size of aggregate from less than 1 µm to almost 4 µm, the more intensive SERS spectra are observed which can be attributed to the formation of more hot spots. The formation of hot spots via aggregation depends on many factors such as size, shape, and surface chemistry of the NPs. In colloidal solutions, the formation of hot spots are controlled by the addition of aggregating salts like NaCl or KNO_3, but this process is not well reproducible.[92,159]

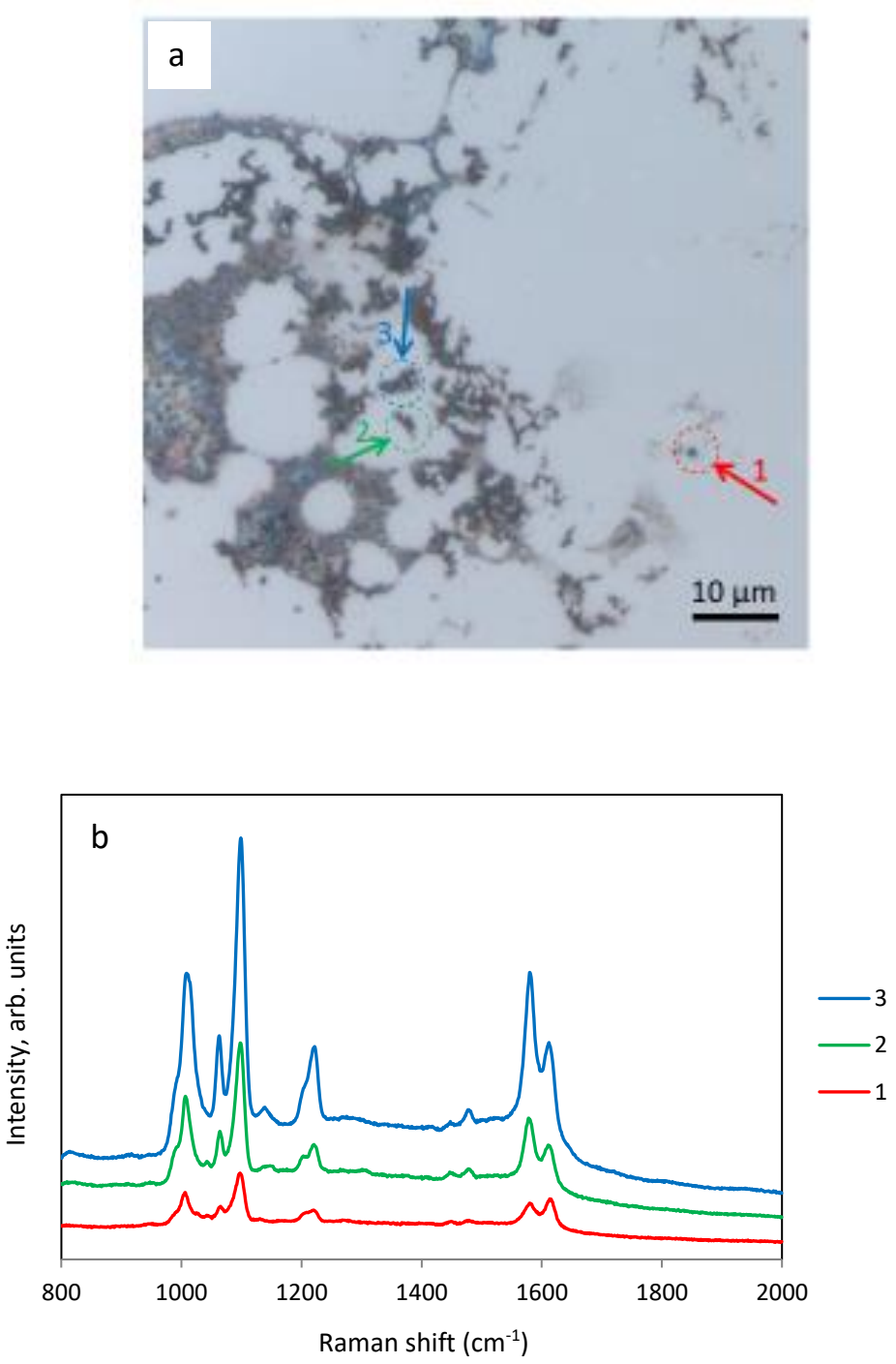

Figure 3.9 Effect of aggregation size on the SERS spectra of 4-MPY on the surface of Au@Ag NPs. (a) Selected aggregates with different sizes. (b) 4-MPy SERS spectra of selected aggregates.[156]

Figure 3.10 shows spectra acquisition of 4-MPy coated Au@Ag NPs deposited on a silicon wafer, taken with different laser powers.

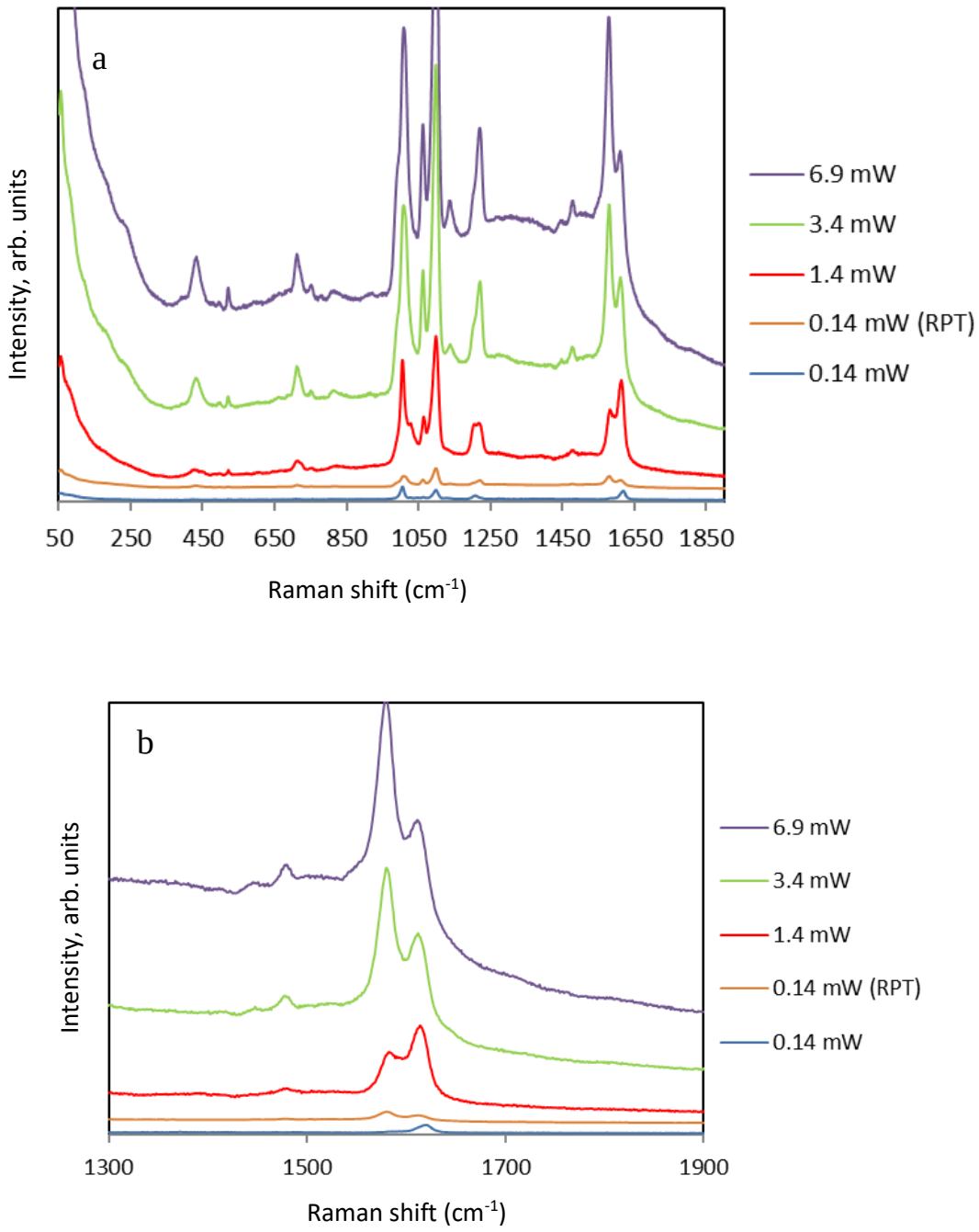

Figure 3.10 Laser power dependency of 4-MPy SERS spectra on the surface of Au@Ag NPs at the same location (a) and laser power induced alteration of 4-MPy coating based on the intensity ratio of I_{1580}/ I_{1609} peaks (b).[156]

It can be observed, that increasing the laser power during measurements, can also increase the enhancement factor, but it also causes change in the structure of the carbonaceous coating. Higher laser powers induce thermal damage to the coating structure and can be suggested by the appearance of the G and D peaks. Also, the intensity ratio of peaks at 1580

and 1609 nm is also changing by increasing the laser power. Figure 3.10 (b) illustrates the evolution of the ratio of I_{1580}/I_{1609} at different laser powers of 0.14, 1.4, 3.4 and 6.9 mW. It can be observed that the intensity ratio increases with increasing the laser power. Finally, by changing the laser power from 6.9 mW back to 0.14 mW, the intensity ratio will stay constant and does not change. This phenomenon can show a laser power (thermal) dependent change of the structure of 4-MPY coating on Au@Ag NPs leading to observed spectral changes. These changes can be attributed to double-end-bonded state (Au@Ag/4-MPy/Au@Ag) formation of coating via both sulfydryl and pyridyl in the structure of 4-MPy.[166]

3.1.3 Competition of coating agents

Figure 3.11 shows the competition of coating agents when two of them are available at the same time in the media and have contact with nanoparticles. The spectra are collected at the same measurement conditions after optimization of the parameters. Figure 3.11 exhibits the characteristic signals of 4-MBA when 4-MBA and SRNOM were both present in the media, which shows 4-MBA binds more strongly than SRNOM to the nanoparticles. The same situation was observed when 4-MPy and SRNOM were both present in the NP containing system, and the spectrum showed the characteristics of 4-MPy which shows that 4-MPy also binds more strongly than SRNOM to the NPs. The competition between 4-MBA and 4-MPy showed that 4-MPy outcompeted 4-MBA and has a stronger bonding with Ag@Au nanoparticles. The results indicate that 4-MPy binds more strongly than the other two coating agents to the nanoparticles. This may be explained by the presence of S and N atoms at the same time in 4-MPy, which leads to a stronger bond than just the S atom in 4-MBA.

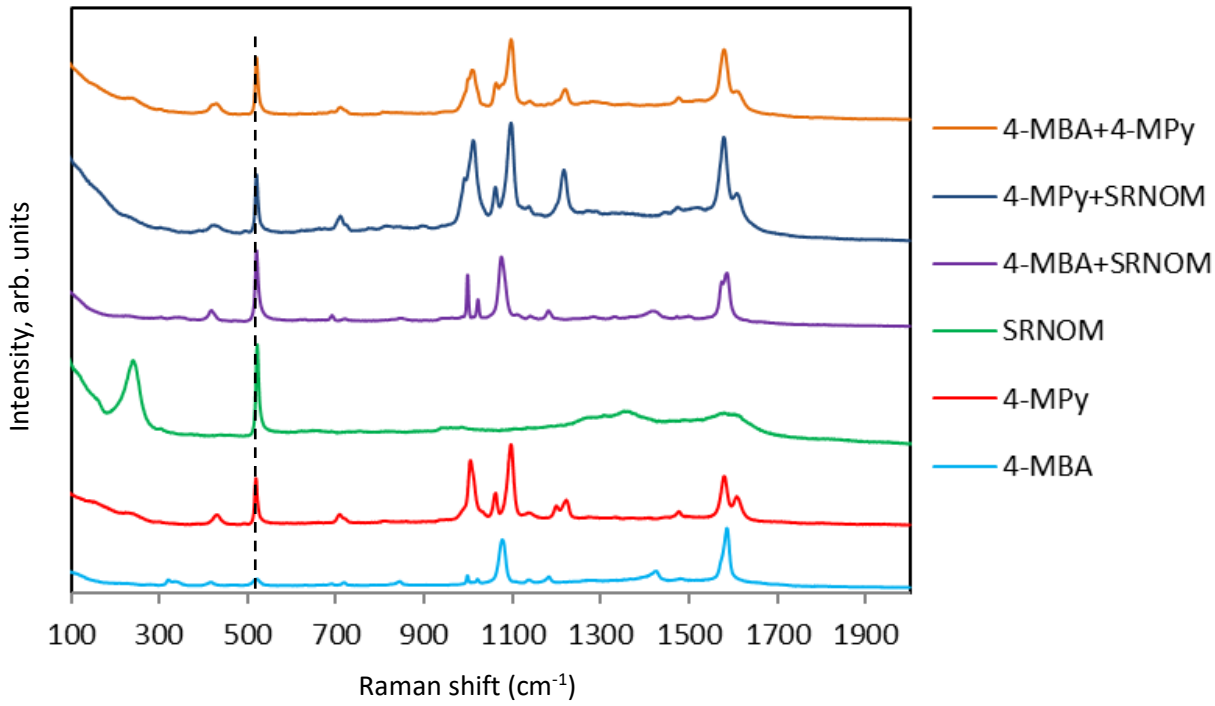

Figure 3.11 Comparison of binding of different coating agents and completion of coating agents.[156]

Figure 3.12 exhibits the SERS spectrum of nanoparticles coated with SRNOM after 24 hours and also the nanoparticle containing systems which exposed to a second coating agent for 2 hours after 24 hours of coating with SRNOM. The spectra indicate the characteristic signals of both coating agents at the same time. It shows that 4-MBA and 4-MPy bind to the nanoparticle despite the SRNOM coating being previously formed. The band at 230cm^{-1} represents the Ag – N vibration of the nanoparticles.[167] Both 4-MPy and 4-MBA are smaller molecules than the SRNOM molecule, and due to presence of a S atom in their molecular structure, they can strongly bind to the surface of the core-shell NPs, even when a coating has already formed.

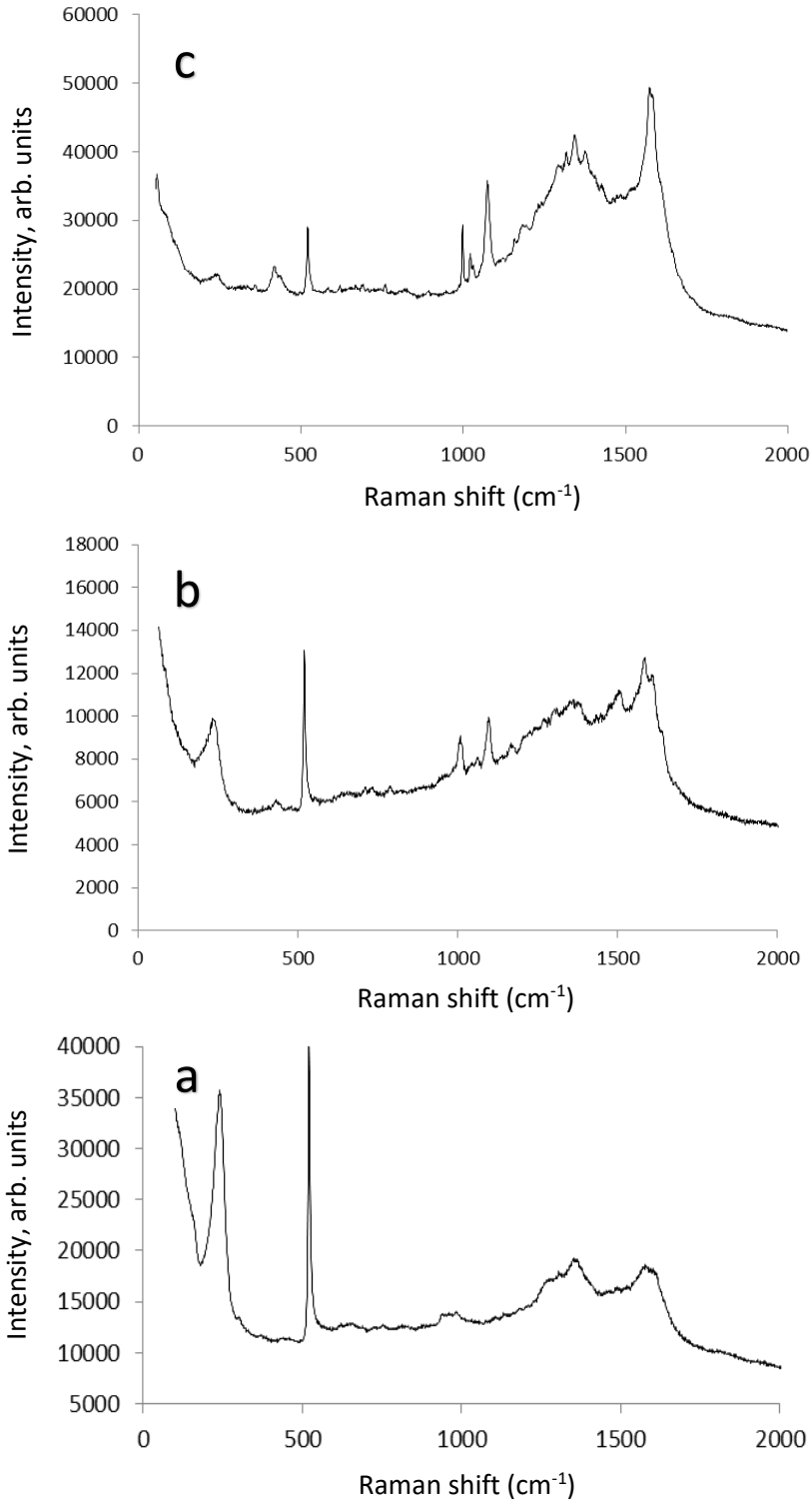

Figure 3.12 SERS spectra of SRNOM coating on Au@Ag nanoparticles after 24 hours (a) SERS spectra of Au@Ag nanoparticle coated with SRNOM for 24 hours and afterwards exposed to 4-MBA (b) or 4-MPy (c) for 2 hours.[156]

3.2 SERS performance of Au@Ag coated silicon wafer

3.2.1 Characterization of Au@Ag coated silicon wafer

SEM images were obtained to confirm if the Au@Ag NPS have successfully coated the silicon wafer. Figure 3.13 shows the successful fixation of the Ag@Au nanoparticles on the surface of the silicon wafer. The nanoparticles are mostly homogeneously distributed over the silicon wafer surface as a monolayer. Also, additional SEM images show the formation of small aggregates which play the role of SERS hotspots. The SEM images were done by Christine Sternkopf at IWC.

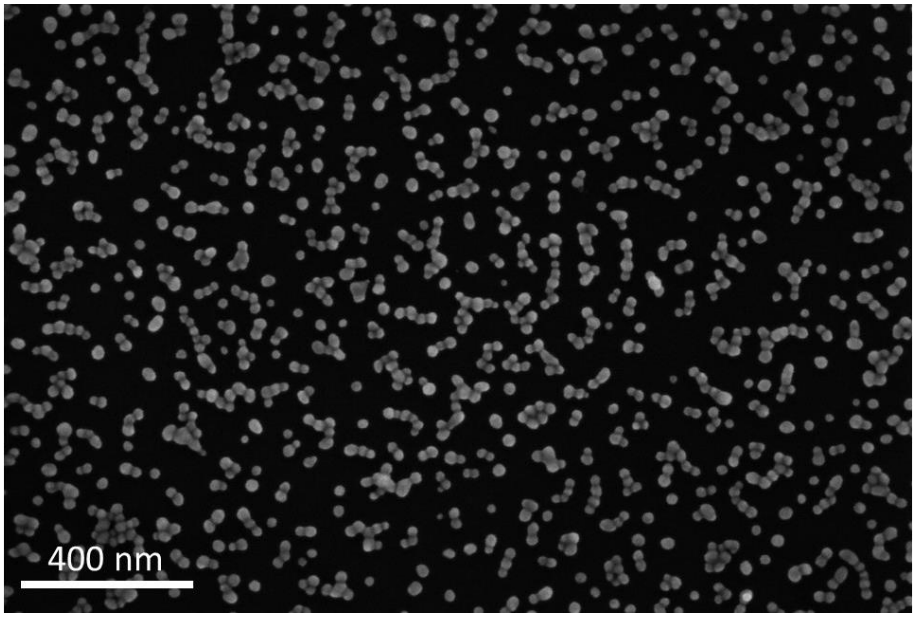

Figure 3.13 SEM image of Au@Ag coated silicon wafer.

3.2.2 Detection of 4-MBA at different concentrations

4-MBA and 4-MPy were used as the probe molecules to evaluate the SERS performance, including sensitivity, uniformity, reproducibility and stability of the as-prepared substrate.

Figure 3.14 shows the SERS spectra collected using the Ag@Au coated silicon wafer for 4-MBA solutions of various concentrations. The intensity of the most prominent peak at around 1076 cm^{-1} enhanced obviously along with the increasing concentration of 4-MBA solution. As

it can be seen, the detection limit of the substrate was found to be 5 x 10^{-9} M for 4-MBA solution.

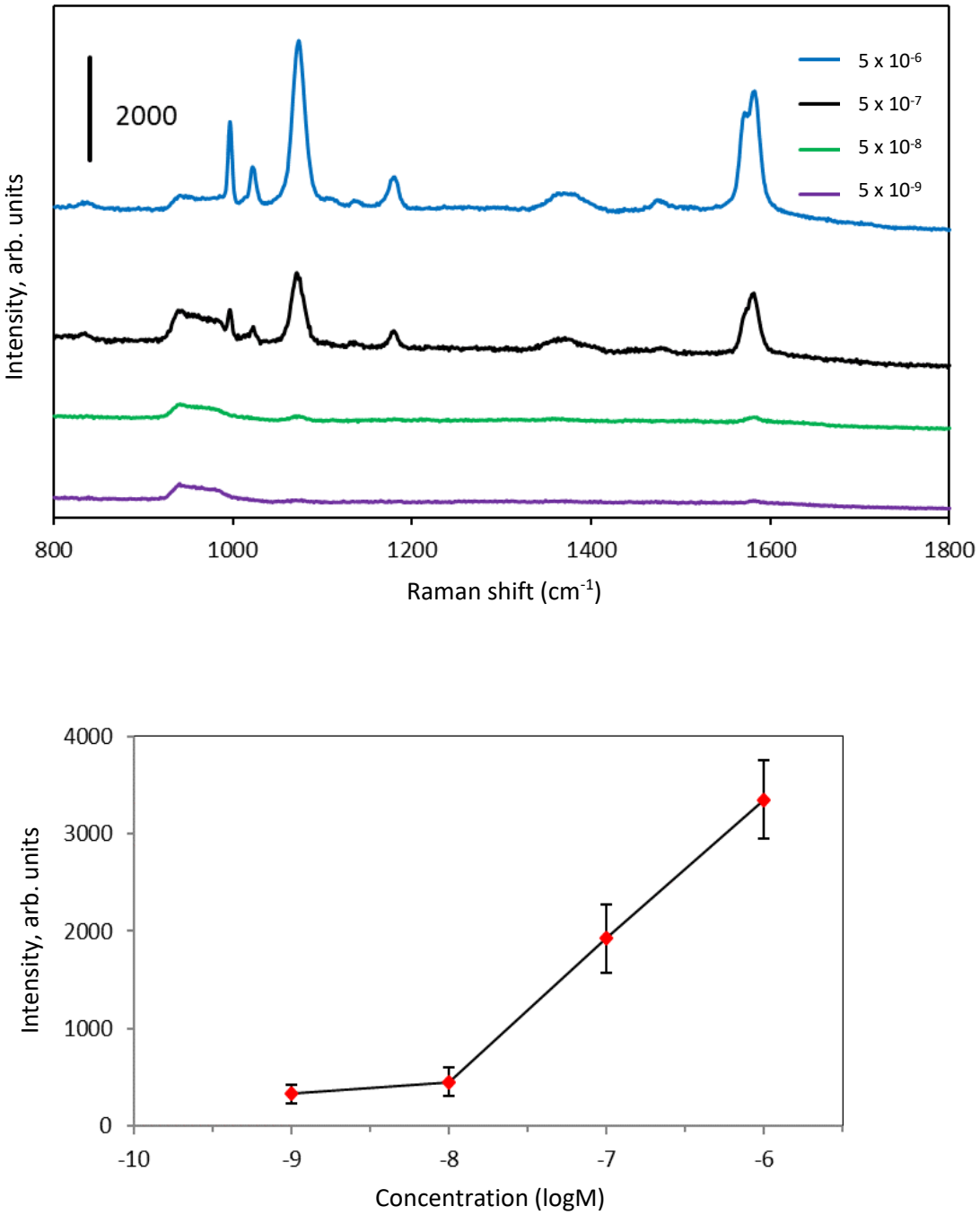

Figure 3.14 SERS spectra of 4-MBA on the substrate with different concentrations and Intensity-log plot for 4-MBA in plane (five replicates for each concentration).

3.2.3 Detection of 4-MPy at different concentrations

The SERS spectra of various concentrations of 4-MPy on Ag@Au coated silicon wafer were also studied and shown in Figure 3.15. The intensity of the most prominent peak at about 1097 cm^{-1} increased with increasing concentrations of 4-MPy solution, and the detection limit was found to be 5 x 10^{-9} M.

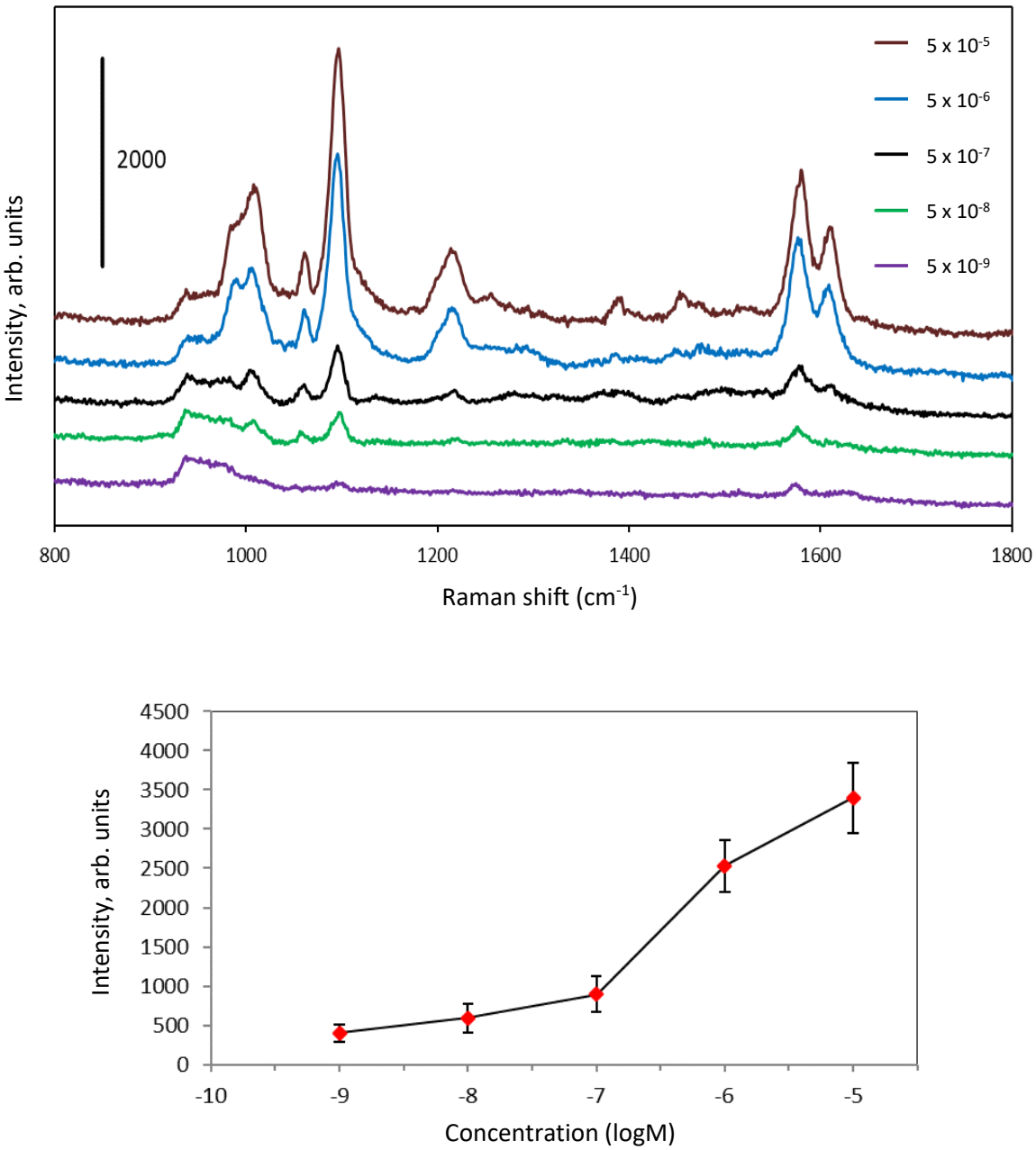

Figure 3.15 SERS spectra of 4-MBA on the substrate with different concentrations and Intensity-log plot for 4-MBA in plane (five replicates for each concentration).

3.2.4 Uniformity of the substrate

To test the spot-to-spot uniformity of the as-prepared substrate, single SERS spectra of 19 random spots of the same substrate were collected, and the intensities of the most prominent band at 1097 cm^{-1} were compared (Figure 3.16). The results can be found in Figure 3.17, which provides a favourable uniformity upon its entire surface. The relative standard deviation (RSD) of the SERS intensity at 1091 cm^{-1} is about 13.5%.

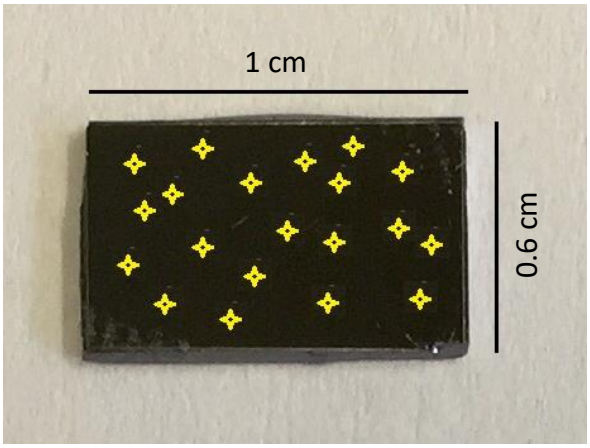

Figure 3.16 random spots for SERS measurements.

Figure 3.19 shows the average peak intensity at about 1097 cm^{-1} for 4-MPy on five different substrates, and it shows that substrates are reproducible. Furthermore, the stability of the substrate was investigated. Figure 3.20 shows the SERS spectra of 4-MPy adsorbed on fresh SERS substrate and (b) the same substrate stored for 1 and 2 weeks. As displayed in Figure 3.20, the Raman spectrum intensity has weakened after the storage time, which can happen due to the naked silver oxidation on the surface of the substrate.[168–170] This can lead to decreasing the SERS activity of the Ag@Au core-shell NPs for SERS detection.

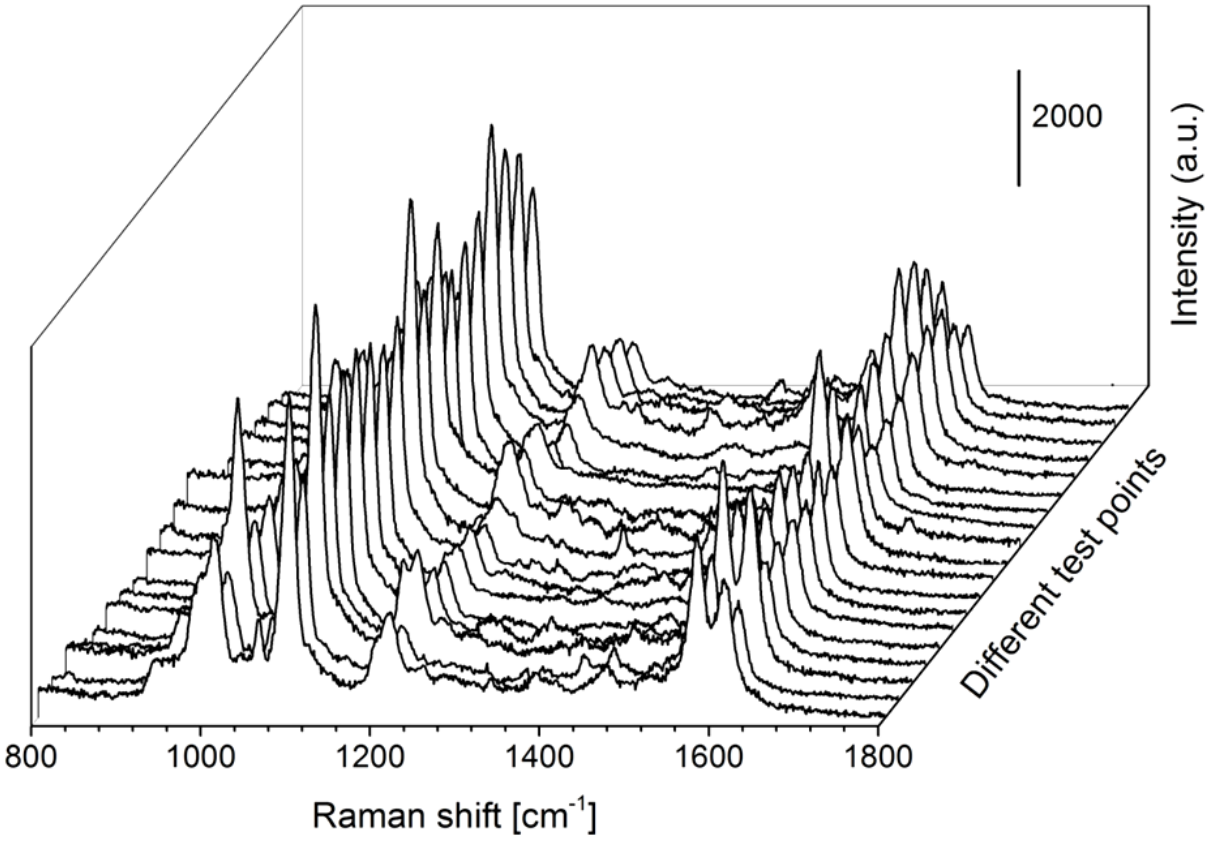

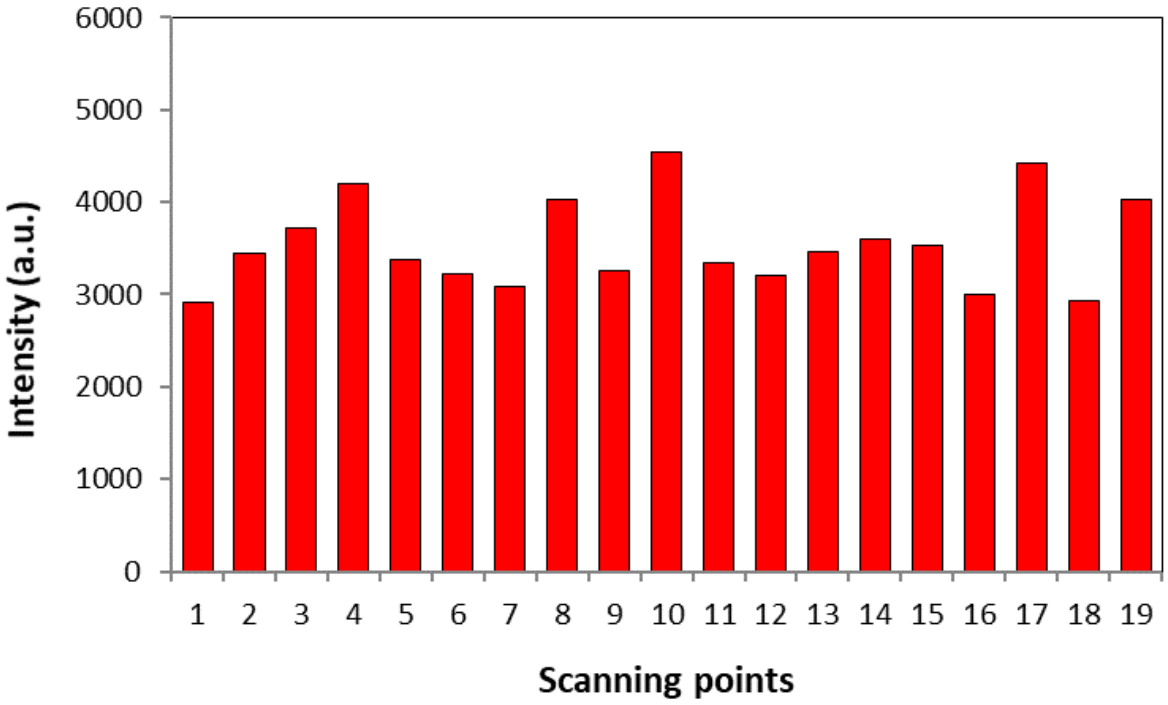

Figure 3.17 Single SERS spectra (a), Raman signal intensity of the 1097 cm^{-1} line(b) for 4-MPy (5 x 10^{-5} M) collected at 19 randomly chosen spots on the same substrate.

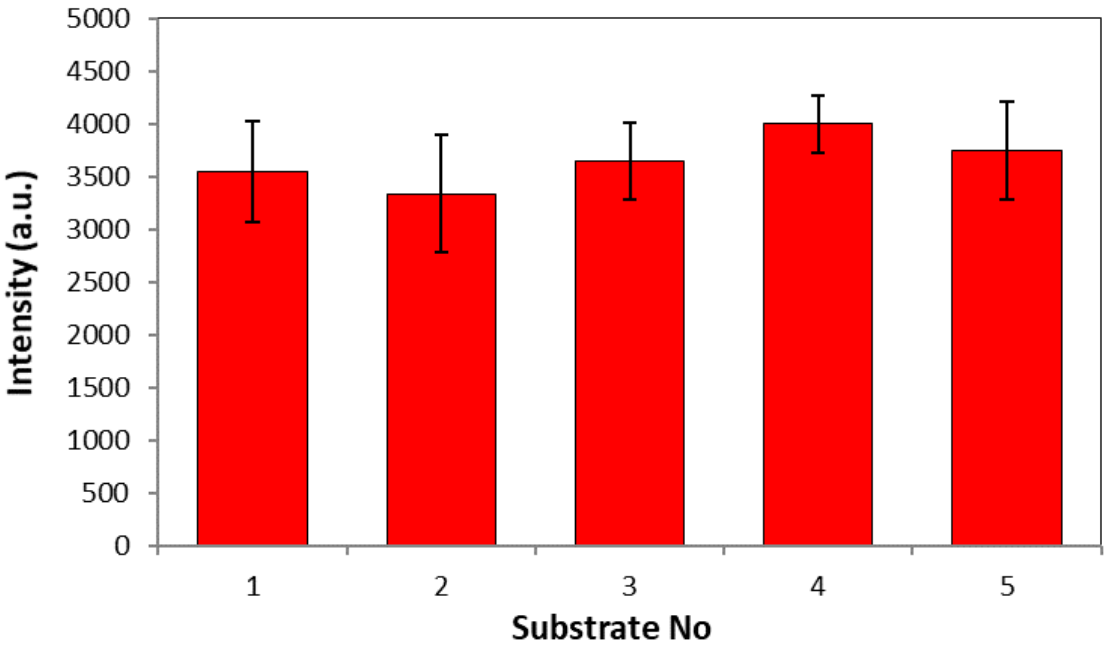

Figure 3.18 Raman signal intensity of the 1097 cm^{-1} line for 4-MPy (5 x 10^{-5}M) recorded on five different substrates

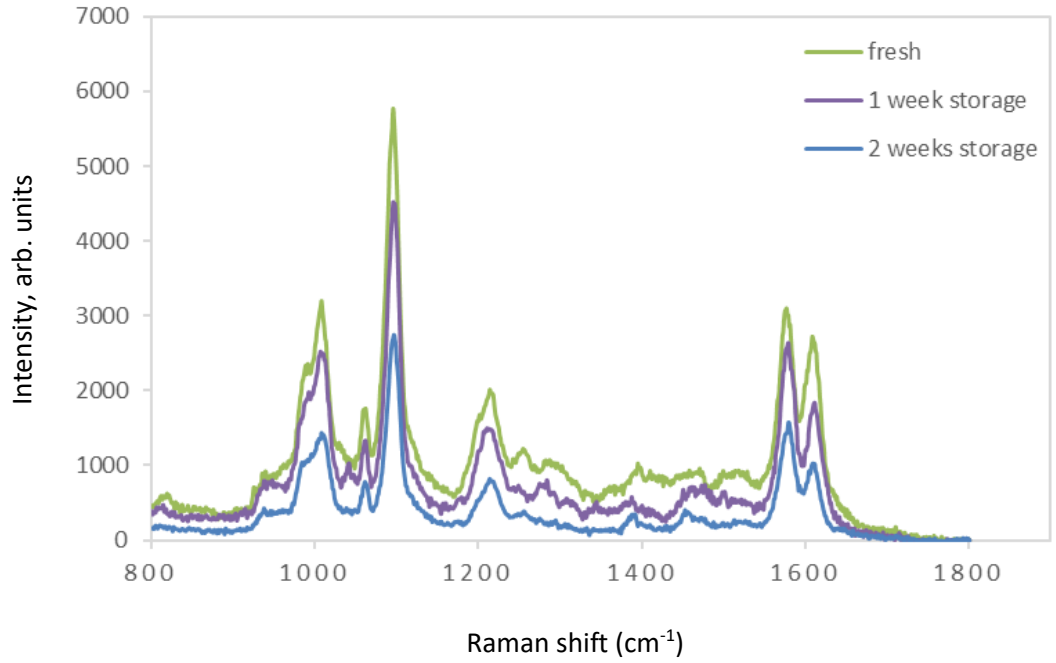

Figure 3.20 Raman spectra for 4-MPy collected on a freshly prepared substrate and substrates stored for 1 or 2 weeks.

To test the as-prepared substrate for practical applications, snow water and tap water were collected and spiked with a stock solution of 4-MPy. Following the same procedure, the SERS measurements were carried out, and the results are shown in Figure 3.19. The SERS signals of the 4-MPy dissolved in Tap and snowmelt water show lower intensities than in DI Water.

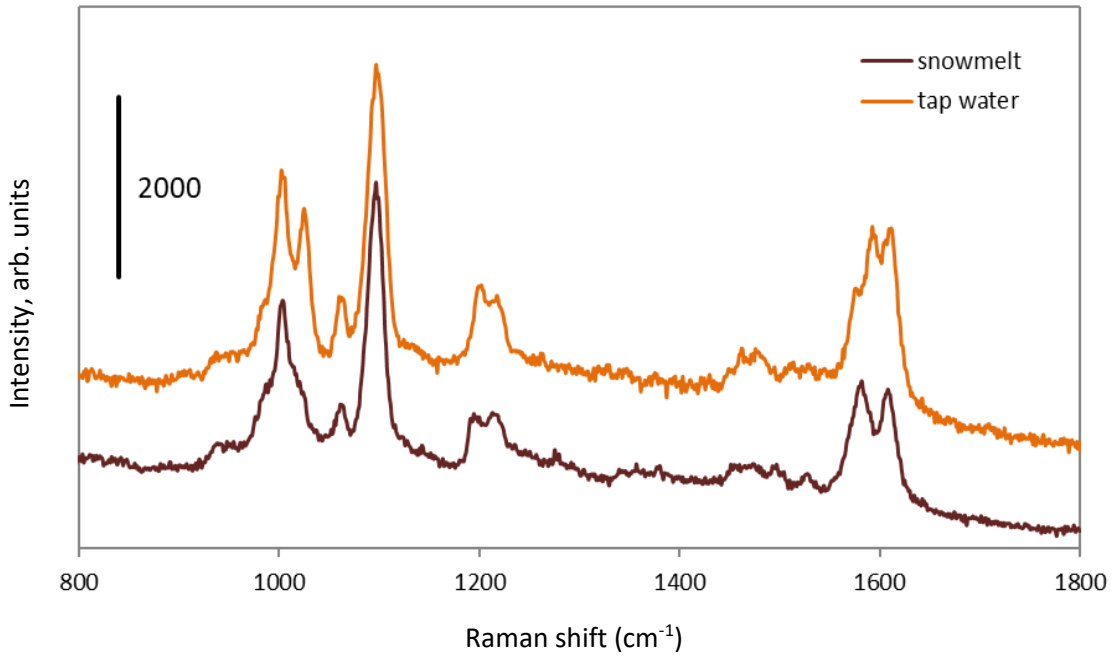

Figure 3.19 SERS spectra of 4-MPy diluted in snowmelt and tap water.

Furthermore, the SERS spectrums are nearly similar, expect an additional band with high intensity at about 1024 cm^{-1} for the spectra of dilution in tap water. Both situations can be caused due to interference of inherent impurities in tap and snowmelt water. However, the similar spectrums show the feasibility of using this SERS substrate for practical applications.

3.2.5 characterization of TiO_2 coating by Au@Ag coated silicon wafer

Figure 3.21 shows the microscope image of the 4-MPy coated TiO_2 Nanoparticles on top of the Au@Ag coated substrate. The green square was set as the SERS mapping area to detect the 4-MPy coating by the substrate.

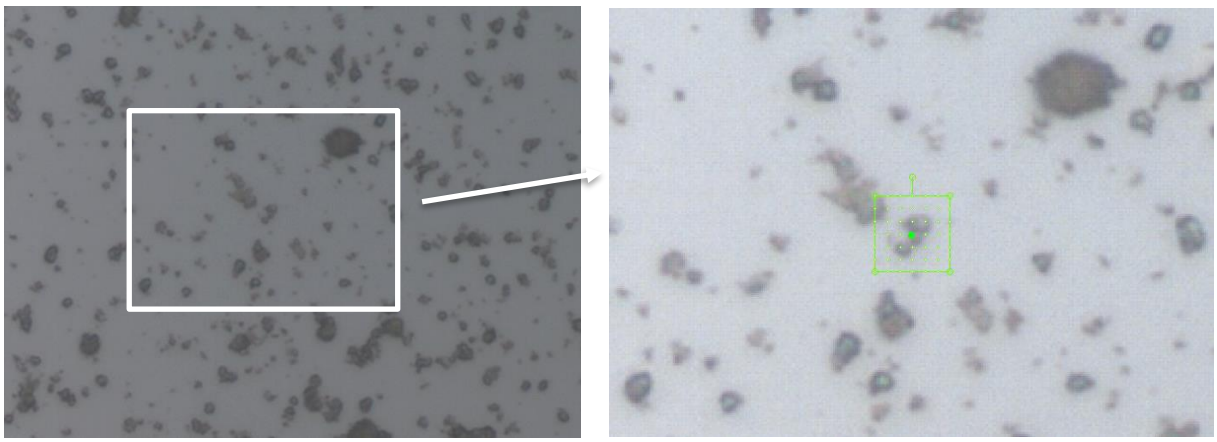

Figure 3.21 Selected area for SERS mapping of the 4-MPy coating of TiO_2 NPs by the substrate.

Figure 3.22 illustrates the result of the spatially resolved mapping of the 4-MPy coated TiO_2 nanoparticles on the surface of the Au@Ag coated silicon wafer. The green dots show the places in which the signals from 4-MPy coated TiO_2 are enhanced due to vicinity with the Au@Ag coated silicon wafer. The blue dots show the points where just the signals from the Au@Ag coated silicon wafer are detected. The red dots show the point where the signal from the substrate and the TiO_2 itself are detected, but no significant signal from the 4-MPy coating was detected. Single sample spectra from each of these areas are shown in Figure 3.23.

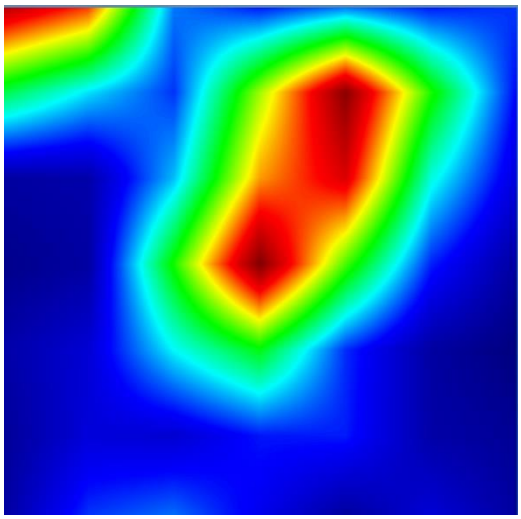

Figure 3.22 result of the SERS mapping of the selected area.

It has been shown that Ag NPs form Ag–S bond instead of Ag–N bond due to more stability of the system.[106,128] Therefore, TiO_2 NP connects with the N atom. It is believed that 4-MPy molecules form a bridge between TiO_2 and Ag@Au nanoparticles which leads to SERS signal. In our work, the 4-MPy coated TiO_2 nanoparticles did not show any SERS signal alone.

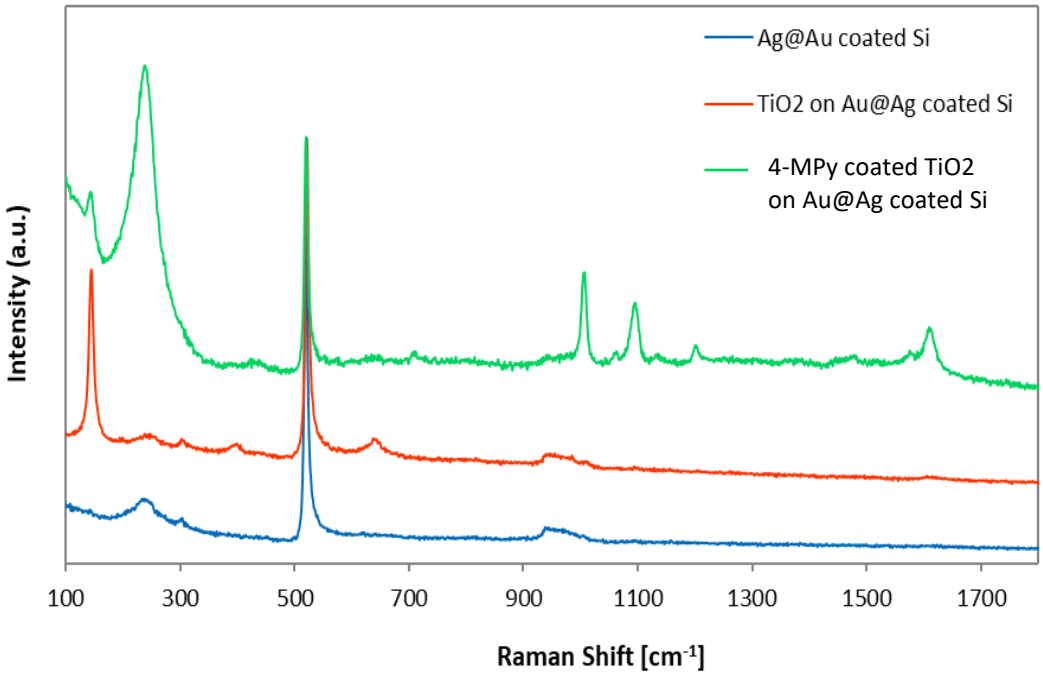

Figure 3.23 Single sample spectra of different areas during mapping of the selected area.

3.3 Antibacterial and SERS application of modified TiO_2 NPs

3.3.1 Characterization of modified TiO_2 nanoparticles

XRD is usually used for identification of the crystal phase structure and phase composition of nanoparticles. In general, the XRD peaks at 2θ= 25.3°, 37.8° and 48.1° are identified as the characteristic diffraction peaks of the anatase crystal phase. The XRD peaks at 2θ= 27.5°, 36.1° and 44.1° are identified as the characteristic diffraction peaks of rutile crystal phase.[82,171] The XRD patterns of TiO_2 nanoparticles modified at different temperatures are shown in Figure 3.24. It can be seen from the XRD patterns that the amount of rutile phase is increasing gradually with increasing the modification temperature and at 950 °C, all the anatase phase is transformed to rutile phase.

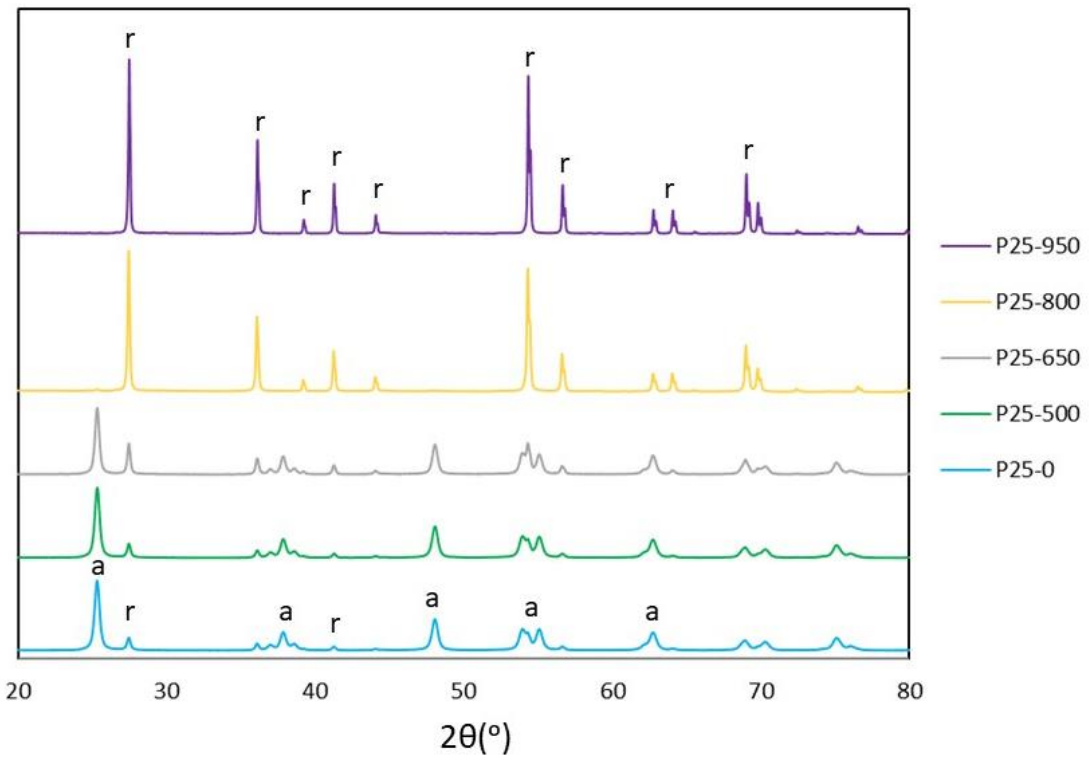

Figure 3.24 XRD patterns of the different powders modified at different temperatures.

Figure 3.25 shows the morphology and particle size of the nanoparticles by using the SEM images. The TiO_2 P25 and modified nanoparticles at 500 and 650 °C have a sphere like morphology with a 20-40 nm homogenous size.

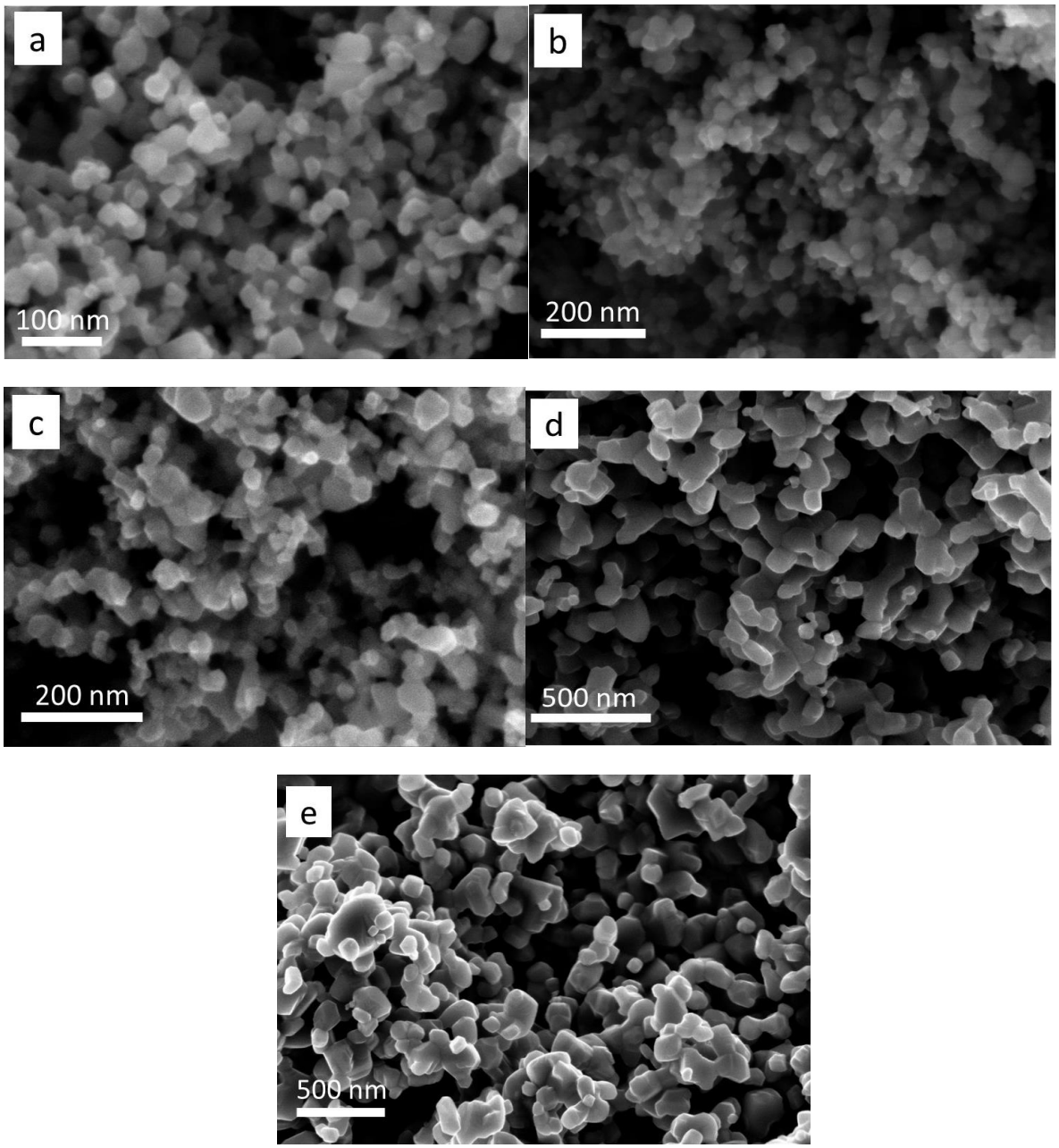

Figure 3.25 The SEM images of Degussa P25 titanium dioxide powders modified at different temperatures (a) P25-0 (b) P25-500 (c) P25-650 (d) P25-800 (e) P25-950.

The nanoparticles modified at 800 and 950 °C have a sphere like morphology with a heterogeneous particle size of 100-200 nm. Average crystallite size of the nanoparticles is calculated based on the Debye-Scherrer equation given below:[172,173]

$$D_{hkl} = \frac{0.9\lambda}{\beta \cos\theta}$$

In this equation D is the crystallize size, λ is the wavelength of X-ray (Cu Kα = 1.54056 Å), β is the full width at half maximum (FWHM) of a peak and θ is diffraction angle.

The results of the BET surface area show that TiO_2 P25 has almost an identical BET value of 52 m^2g^{-1} like nanoparticles modified at 500 and 650 °C. The particles modified at 800 and 950 °C have a lower surface area of almost 14 and 5 m^2g^{-1} respectively, which is attributed to the increase of particle size. The results of the BET measurements are summarized in table 1.

Table 1. Comparison of phase composition and surface features of the TiO_2 NPs modified at different temperatures

Samples	Anatase		Rutile		BET surface area (m2g-1)	E.g. (eV)
	Content (%)	Crystallite size (nm)	Content (%)	Crystallite size (nm)		
TiO2-P25	86.5	21.6	13.5	29.3	51.99	3.44
P25-500	84.5	22.2	15.5	29.57	52.74	3.37
P25-650	70.9	23	29.1	31.5	51.11	3.29
P25-800	2.1	-	97.9	44.52	14.02	3.11
P25-950	-	-	100	50.9	5.07	3.05

Figure 3.26 shows the result of the UV-vis DRS spectra of TiO_2 P25 and TiO_2 nanoparticles modified at different temperatures. With increasing the modification temperature, samples showed a red-shift of absorption edge toward longer wavelengths. This clearly indicates a decrease in the band gap energy of TiO_2. The Eg values are summarized in Table 1. The decrease of the band gap energy is attributed to phase transfer from anatase to rutile.

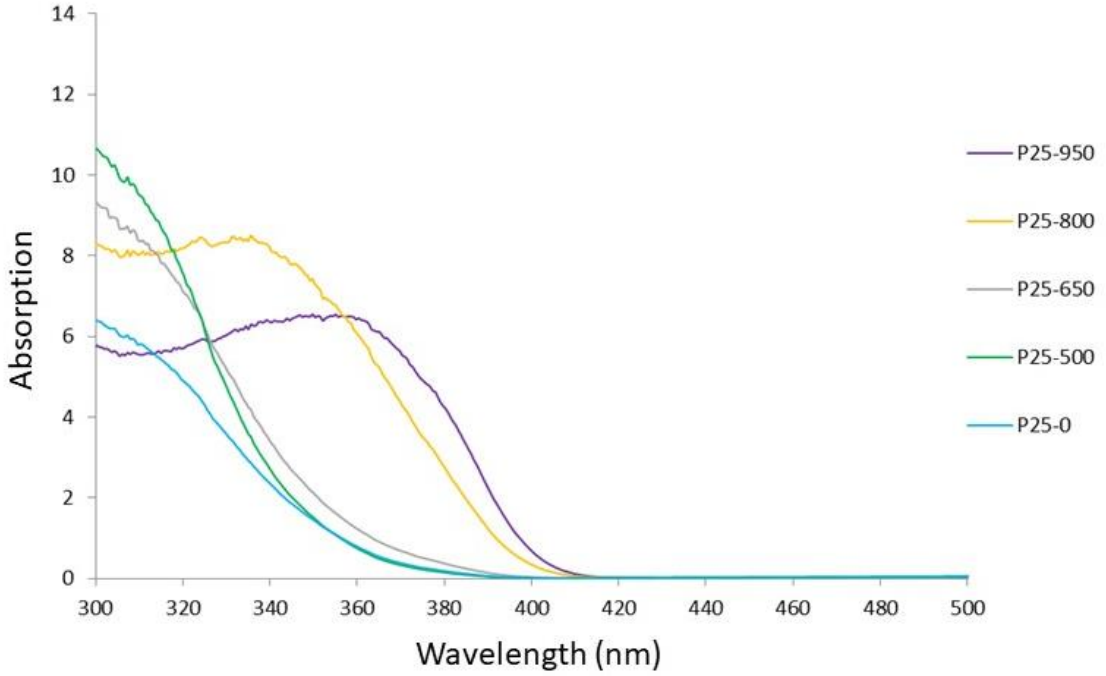

Figure 3.26 UV-visible diffuse reflectance spectra of Degussa P25 titanium dioxide modified at different temperatures.

Raman spectroscopy was used as an additional method to confirm the phase transformation of the modified nanoparticles (Figure 3.27). The rutile phase shows various bands at around 238, 448, 611 and 826 cm^{-1}. The anatase bands are observed at 196, 395, 517 and 639 cm^{-1}.[174–176] The comparison between the samples shows the transformation of the crystallite phase from anatase to rutile with increasing the modification temperature. The red arrows in figure 3.27, indicate the emerge of rutile bands because of phase transformation from anatase to rutile by increasing the modification temperature.

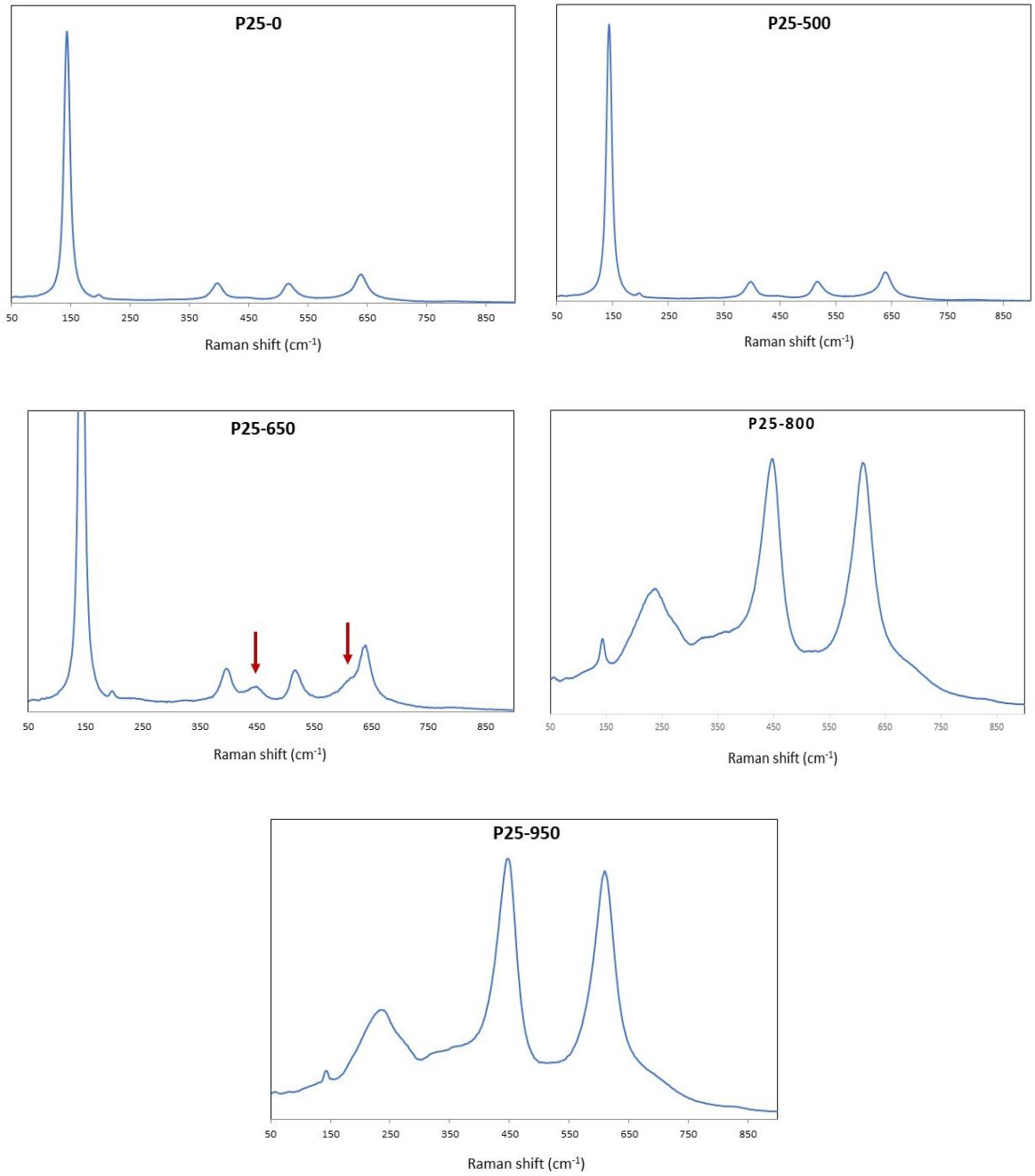

Figure 3.27 Raman spectra of Degussa powders modified at different temperatures. (The arrows show the emerge of rutile bands because of phase transformation from anatase to rutile at 650 °C).

3.3.2 SERS measurement of coating on modified TiO_2 NPs

Figure 3.28 illustrates the normal Raman spectra of 4-MBA in the solid state, in 0.1-M ethanol solution, the normal Raman spectrum of TiO_2-0 and SERS spectra of 4-MBA on TiO_2-0. The SERS spectrum of 4-MBA on TiO_2-0 is consistent with those previously reported in literature.[177,178] The spectrum is dominated by strong bands at about 1594 and 1078 cm^{-1},

which are assigned to aromatic ring v_{8a} (a_1) and v_{12} (a_1) characteristic vibrations, respectively. The band at 1182 cm^{-1} (v_9, a_1) is attributed to C-H deformation mode. For comparison, the normal Raman spectrum of TiO_2-0 is illustrated in the figure, and no Raman peaks are observed for TiO_2-0 in the range of 800-1800 cm^{-1}. The intensity and position of the Raman peaks for the SERS spectrum of 4-MBA adsorbed on TiO_2-0 is significantly different from the normal Raman spectra of 4-MBA in ethanol solution and also in solid form. This indicates that Raman bands of 4-MBA molecules adsorbed on TiO_2-0 particle are enhanced.

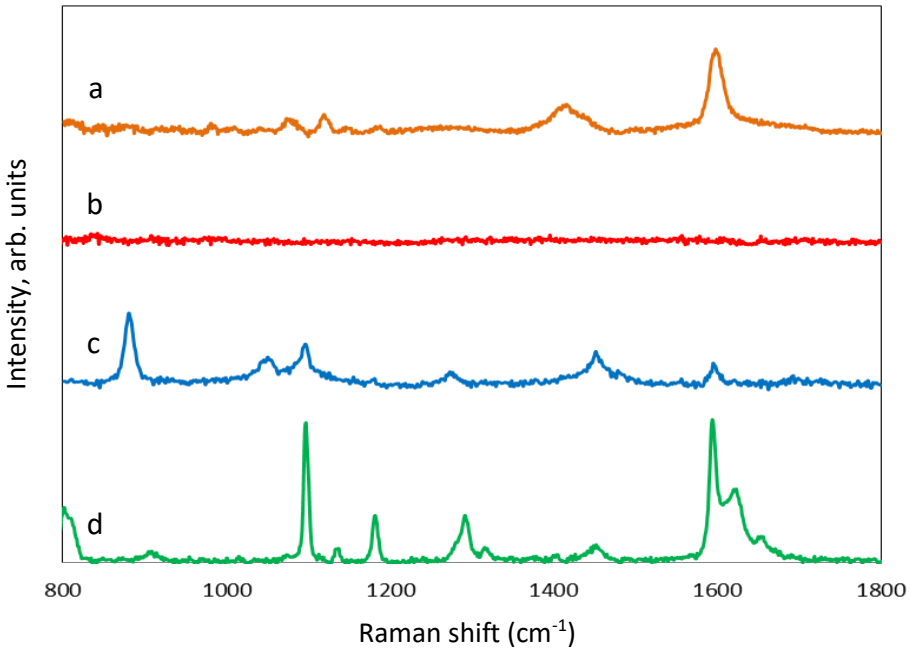

Figure 3.28 SERS spectrum of 4-MBA adsorbed on TiO_2 (a) and the normal Raman spectra of TiO_2 (b), normal Raman spectra of 4-MBA in 0.1 Methanol solution (c) and the solid state (d).

Figure 3.29 shows the SERS spectra of 4-MBA molecules adsorbed on TiO_2 NPs modified at different temperatures in the furnace. It can be seen that the TiO_2 NP modified at 500 °C shows a significantly higher SERS signal.

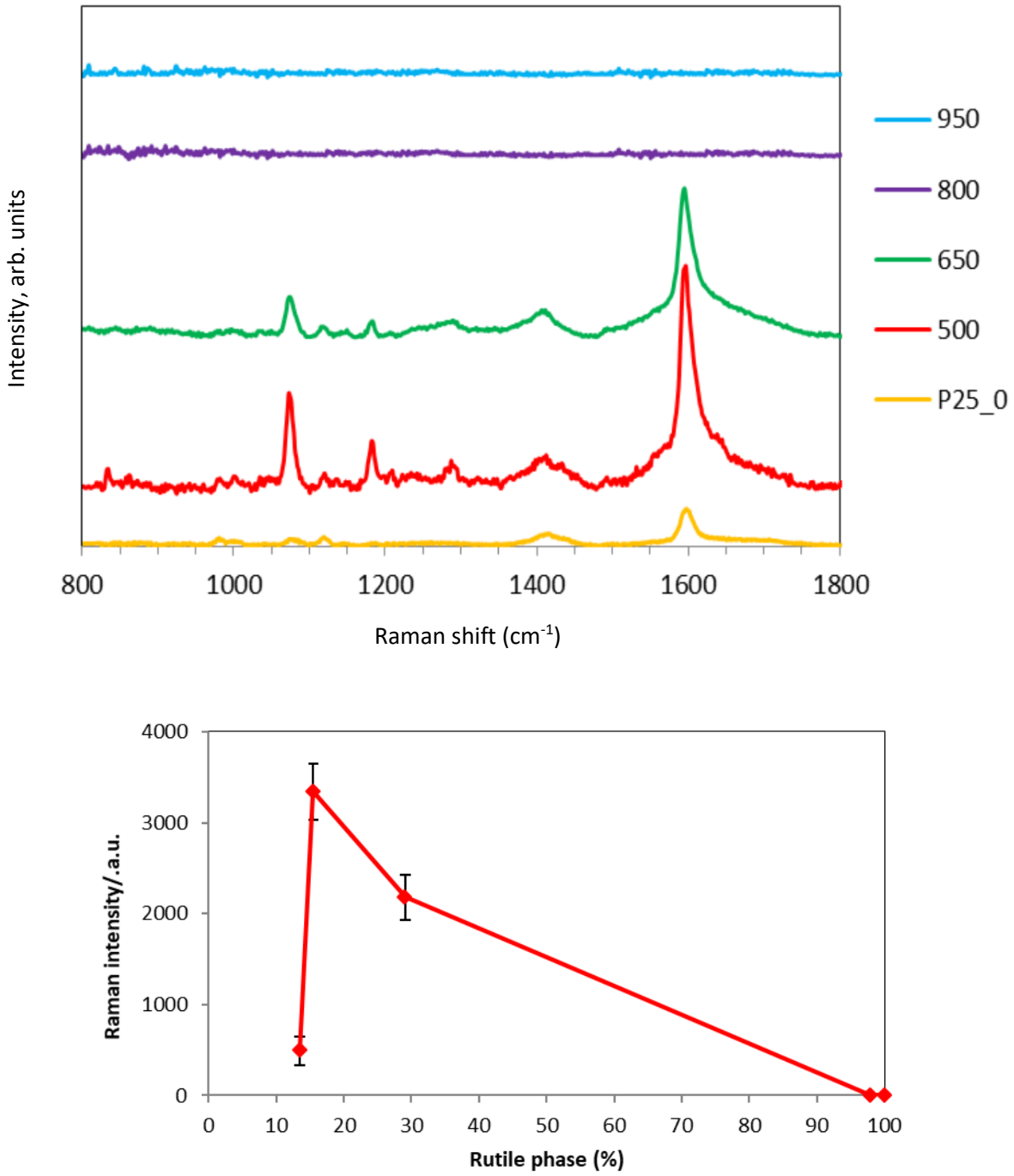

Figure 3.29 SERS spectra of 4-MBA adsorbed on TiO_2 NPs modified at different temperatures (a) The plot of the SERS signal intensity of 4-MBA at 1594 cm^{-1} versus the rutile phase (b).

By increasing the temperature from 500 °C to 650 °C, the enhancement declines, but anyway the enhancement is still much higher than the unmodified NPs. With increasing the temperature to 800 °C and 950 °C, the NPs show no enhancement, and therefore no SERS signals from 4-MBA molecules adsorbed on the NPs are observed. The unmodified TiO_2 NPs and NPs modified at 500 °C, and 650 °C have similar crystallite size and surface area. Therefore,

the changes in the intensity of SERS signals cannot be due to a significant difference in the amount of 4-MBA adsorbed on the surface of the NPs. There must be other factors contributing to the additional SERS enhancement of adsorbed 4-MBA molecules on TiO_2 NPs modified at these temperatures. With increasing the temperature to 800 °C and 950 °C, the SERS signal declines dramatically, and no peaks for the adsorbed 4-MBA molecules are observed. In literature, it has been contributed to different anatase and rutile structure phase for mixed crystal structure TiO_2.[179] It has been declared that at an appropriate proportion of anatase and rutile phase, the optimal interaction between the phases and therefore, the highest SERS enhancement signal can occur. The mechanism is explained as following:

The anatase TiO_2 has a band gap of 3.2 eV, which is different from the band gap energy of rutile TiO_2 with 3.0 eV. So, their conduction bands are positioned differently. Anatase TiO_2 has more oxygen vacancies (defects) and dislocations within the crystal lattice network than rutile TiO2, enabling it to capture more electrons. Correspondingly, the excited state of anatase TiO_2 has an active electron-hole pair potential with a higher oxidation-reduction capability. In mixed phase TiO_2 NPs, there is a band bending of the phases which helps interaction between the phases and enables the holes to be transferred easily from surface state energy levels of rutile phase to the surface state energy levels of anatase phase. The interaction between the phases provides a TiO_2-to-molecule CT in addition to the TiO_2-to-molecule CT for single phase anatase TiO_2. Other studies have also reported the effective separation of photogenic charge carriers due to the interaction between anatase and rutile phase, which leads to an overall enhancement of the TiO_2-to-molecule CT efficiency. Yang et al. mentioned that the appropriate ratio of the anatase and rutile phase is approximately 85% and 15% respectively and the enhancement declines dramatically when to ratio is 75% and 25% due to the excessive low surface defects and surface active sites[105]. In our experiment, the appropriate ratio of the anatase and rutile phase is also in the same range with 84.5% and 15.5%. By increasing the modification temperature from 500 °C to 650 °C, the anatase phase decreases to 75% (25% rutile phase), but the decrease of SERS signal for adsorbed 4-MBA molecules is not dramatic like what has been observed in the literature.[105] The reason can be due to the similar surface defects and surface area for both NPs modified at both temperatures.

3.3.4 Stability of coating

To investigate the coating's stability on TiO_2 NPs, the SERS spectra of 4-MBA coating with a concentration of 10^{-3} molar on TiO_2 NPs modified at 500 °C were taken after different washing steps as illustrated in Figure 3.30. As it can be seen the SERS spectra declines noticeably when two times washing steps are applied instead of one time washing step but no significant change of the intensities are observed when the NPs are washed for more times which shows the stability of the 4-MBA coating on TiO_2 NPs.

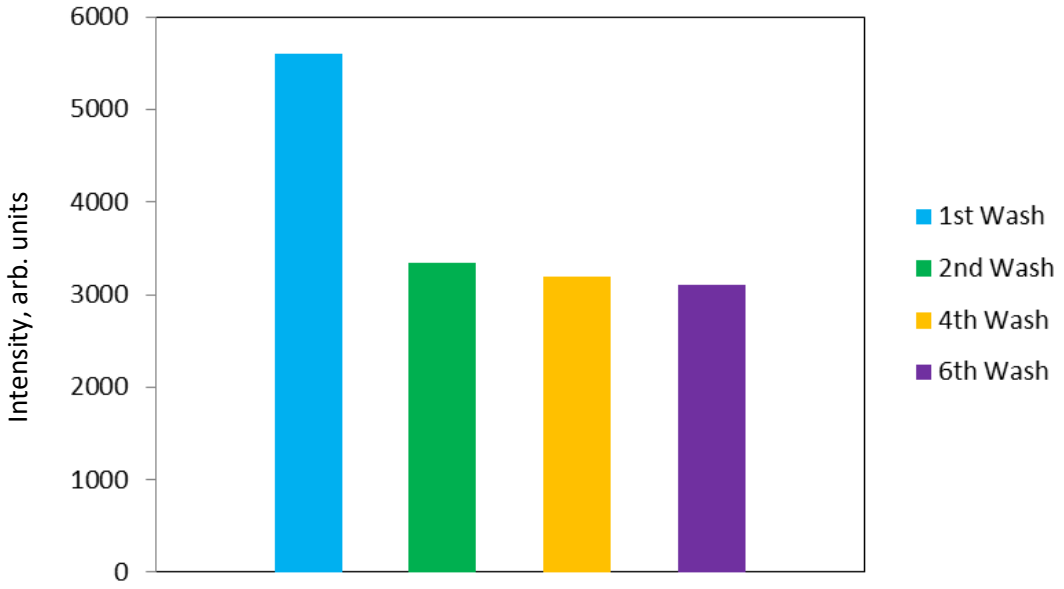

Figure 3.30 SERS signal intensity of 4-MBA at 1594 cm^{-1} after different washing steps.

3.3.5 Coating in the presence of metal ions

The effect of heavy ions on the SERS signal of 4-MBA adsorbed on TiO_2 NPs modified at 500 °C was investigated. It was found that the SERS spectrum of 4-MBA is very sensitive to the presence of heavy metal ions. Figure 3.31 shows the spectrum of 4-MBA solution with a concentration of 10^{-3} Molar in the presence of copper ion with the same concentration. As it can be seen the position of the main SERS signals exhibit some changes. The peak at about 1078 cm^{-1} shows a blue shift and the peak at about 1594 cm^{-1} shows a redshift. Also, the intensity of the peaks has declined in the presence of copper ion compared to the case when just 4-MBA is present in the solution.

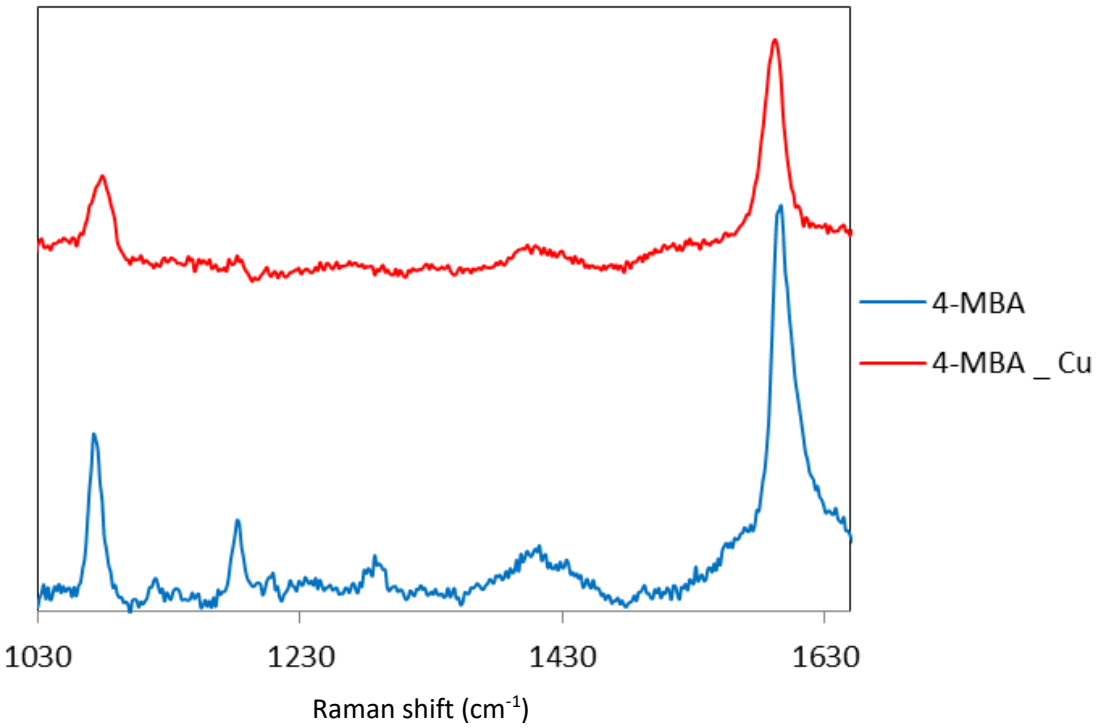

Figure 3.31 SERS response of 4-MBA (1 x 10^{-3} M) to the presence of Cu^{2+}.

Figure 3.32 shows the spectrum of 4-MBA in the presence of mercury in a concentration of 10^{-3} Molar, and as it can be seen, the position of the peaks is shifted. The peak at about 1078 cm^{-1} shows a blue shift and the peak at about 1594 cm^{-1} shows a red shift. The intensity of the SERS peaks has also significantly increased. Additionally, in the presence of Hg^{+}, new peaks are observed which can be assigned to the ring distortion modes of 4-MBA.

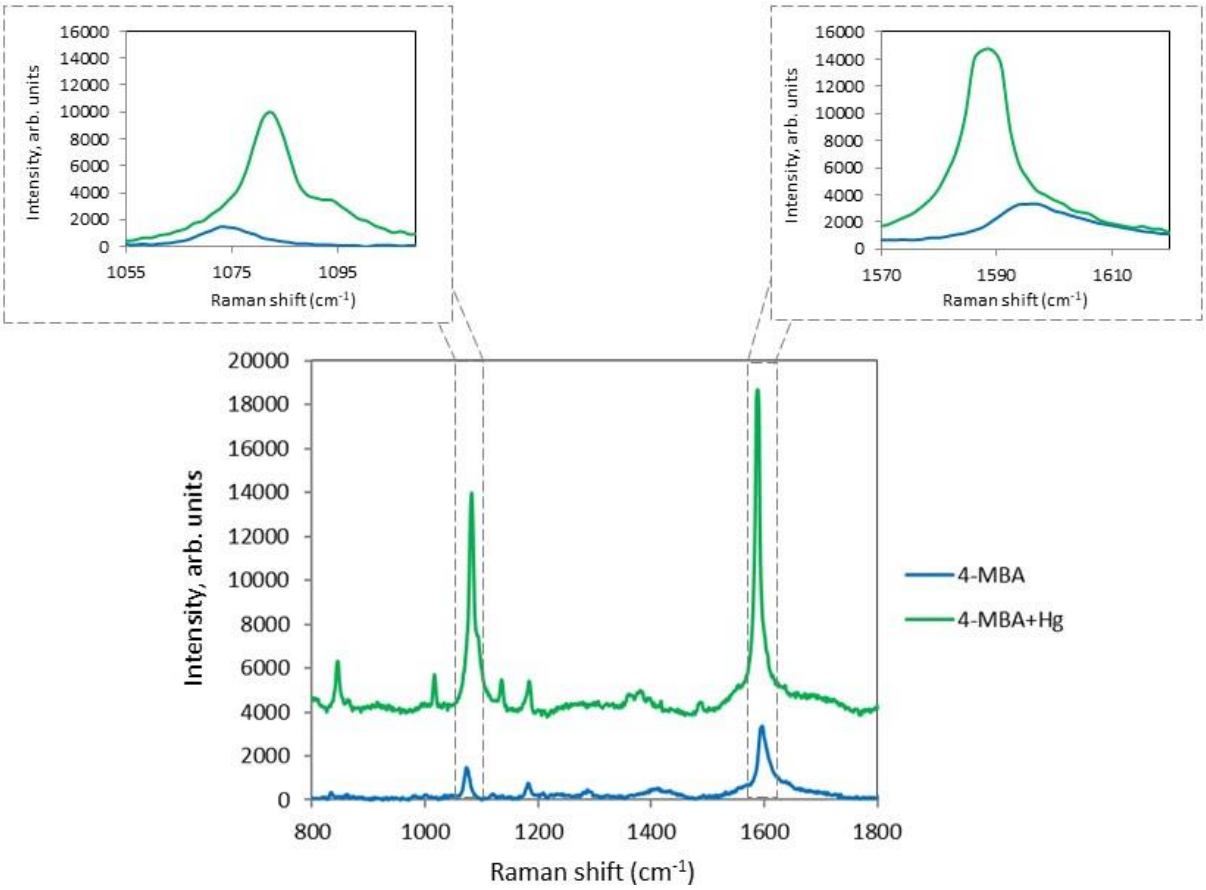

Figure 3.32 SERS response of 4-MBA (10^{-3} M) to Hg^{2+} cation.

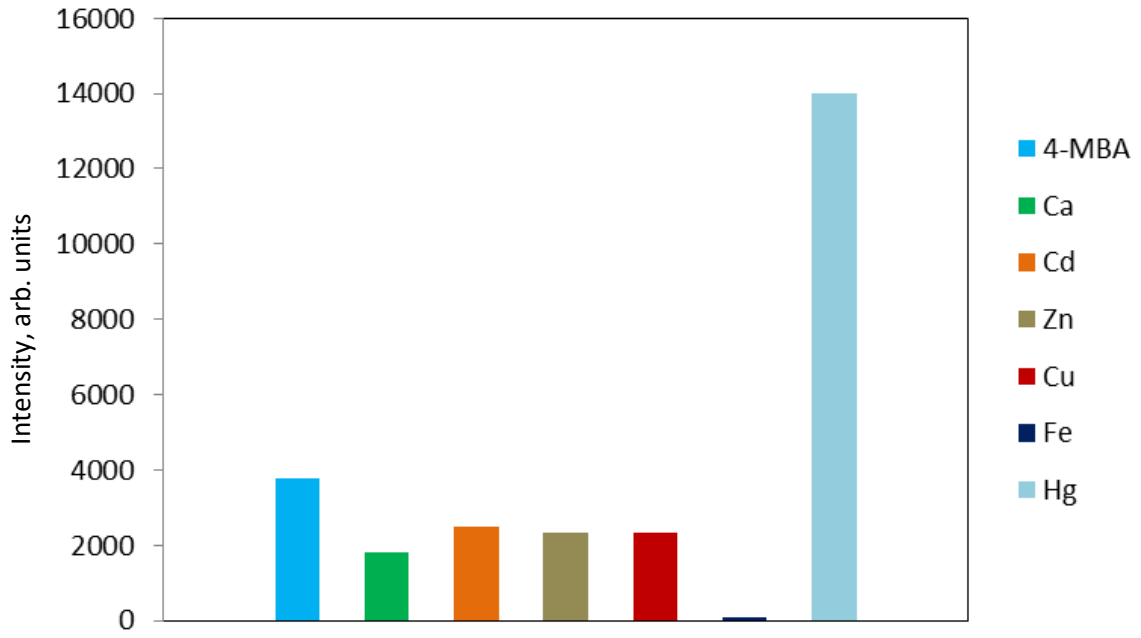

Figure 3.33 The dependence of the peak intensity of the band at 1594 cm^{-1} on different metal ions.

Figure 3.33 shows the intensity of the SERS peak at 1594 cm^{-1} in the presence of different metal ions. As can be seen, the intensity of the peak declines in the presence of Ca^{2+}, Cd^{2+}, Zn^{2+}, Fe^{3+}. It was also found that Fe^{3+} has a much more effect on the intensity of the signal than Ca^{2+}, Cd^{2+} and Zn^{2+}. The intensity of the signal increases significantly in the presence of Hg^{2+}.

Figure 3.34 shows the SERS spectral region between 1570 cm^{-1} and 1620 cm^{-1}. The graph shows the shift of the peak at 1594 cm^{-1} in the presence of metal ions. In the presence of Cu^{2+}, the peak is redshifted. In the presence of Cd^{2+} and Zn^{2+}, the peak is blue shifted. Ca^{2+} does not change the position of the peak. In the presence of Fe^{3+}, no peak was observed.

The aforementioned observations of spectral alteration suggest that the metal ions might interact with the 4-MBA molecules to form a complex, leading to the reorganization of the adsorption process of 4-MBA at the surface of the TiO_2 NP, and also the related vibrations becoming weakened or enhanced. The differences in the SERS spectra in the presence of different metal ions can be due to the difference in the coordination surrounding between metal ions and 4-MBA.

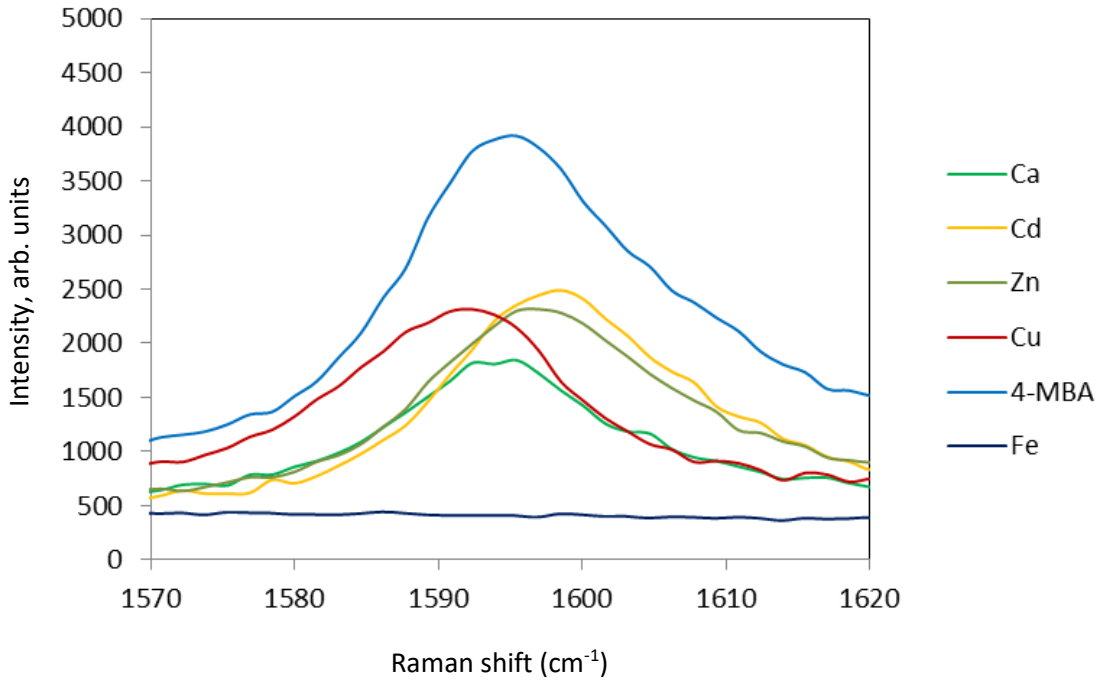

Figure 3.34 SERS response of the band at about 1594 cm^{-1} of 4-MBA to different metal cations.

Table 2 summarizes the amount of blue or redshift of the 4-MBA peak position in the presence of different heavy metal ions.

Table 2. Shifts in position of 4-MBA SERS peak at 1594 cm^{-1} in the presence of different metal ions

Metal ion	Shift in peak position (cm^{-1})
Ca^{2+}	0
Cd^{2+}	+3
Zn^{2+}	+1
Cu^{2+}	-3
Hg^{2+}	-3
Fe^{3+}	No peak observed

3.3.6 Antibacterial activity under UV light

In cooperation with the Islamic Azad University of Shahreza in Iran, the photocatalytic activity of modified TiO_2 NPs at different temperatures against sample bacteria (*E.coli and S. aureus*) was investigated. Initially, blank control experiments (bacterial solutions without any catalyst) were performed under dark and UV light irradiation. The results showed no significant colony-

forming unit (CFU) decrease in nanoparticle free medium. Other experiments were conducted under UV light under controlled conditions. All nanoparticles showed antibacterial activity under UV light conditions (Figure 3.35). The inactivation efficiency under the UV light conditions was as following order: P25-500 > P25-650 > P25-0 > P25-800 > P25-950

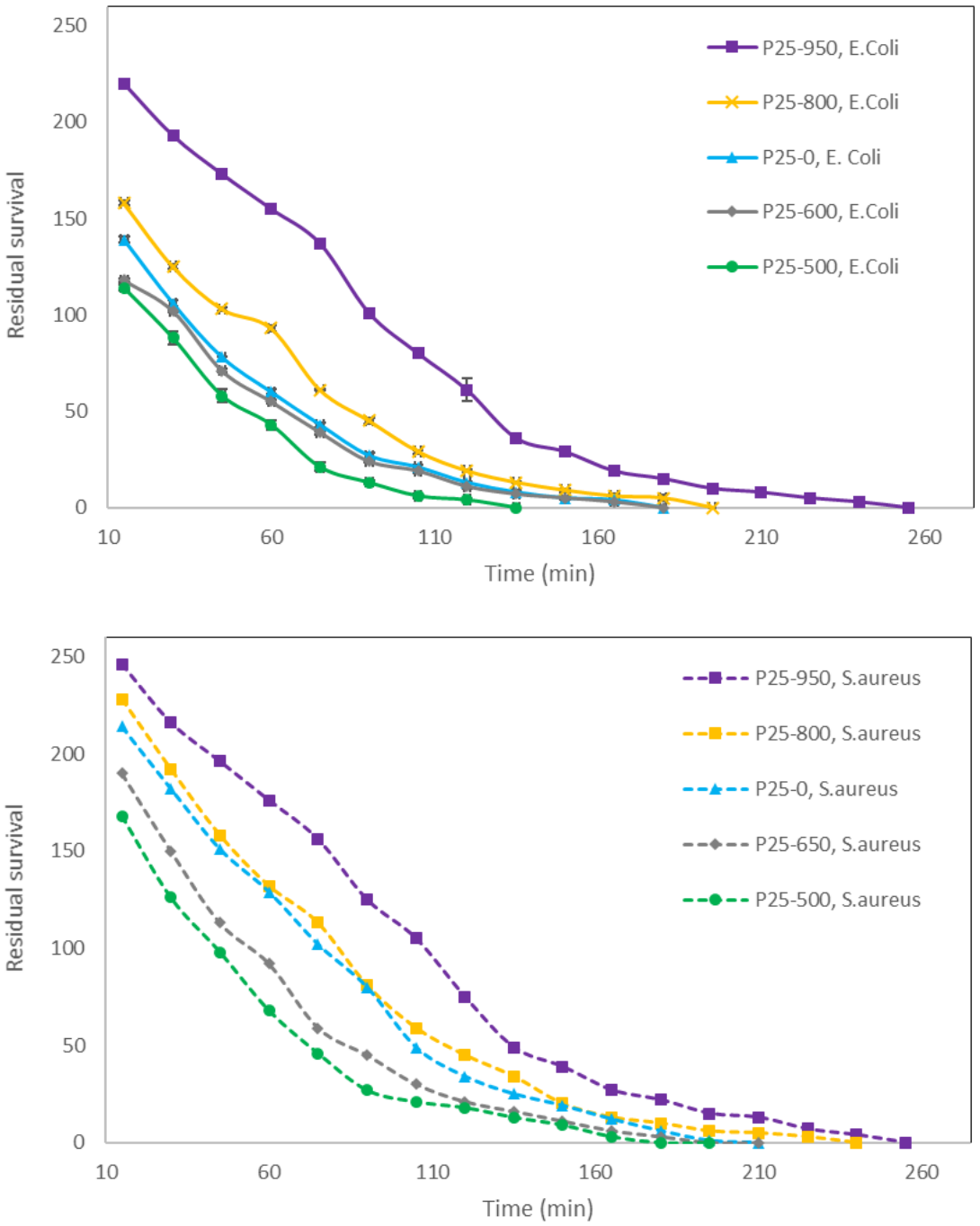

Figure 3.35 Antibacterial activity of modified TiO_2 NPs against sample microorganisms under UV light.

3.3.7 Influence of different factors on the antibacterial performance of TiO_2 NPs

Influence of particle size

Normally, a higher specific surface area leads to a better photocatalytic activity of the NP. Despite that, some studies show contradictive results regarding the size of the semiconductor nanoparticles, in general, it has been observed that small NPs are more toxic than bigger particles.[180] The current experiment found that the antibacterial of TiO_2 decreased with increasing particle size or decreasing the specific area. The NPs modified at 800°C, and 950°C have bigger particle sizes than other particles with similar particle sizes. The smaller the average size or higher the sample's surface area, the greater the observed antibacterial effect.

Effect of optical properties

There was a reverse relation between band gap energy and modification temperature of TiO_2 samples. In general, it is believed that decrease in band-gap energy results in higher antibacterial activity. In our study, there was no clear relation between bang pap and antibacterial activity of the modified NPs.

Effect of crystal structure

Most of the studies show that anatase TiO_2 NPs show a higher photocatalytic and antibacterial effect than rutile NPs. Our study also observed that the crystal structure plays a role in antibacterial activity.

Microorganism type

All samples exhibited antibacterial activity against both E. coli and S. aureus, but the deactivation efficiency in the case of E.coli as a gram-negative bacteria was higher than S. aureus, which is a gram-positive bacteria. The NPs antibacterial efficiency on gram-negative or gram-positive bacteria is still debatable, but several studies have shown higher efficiencies for gram-negative bacteria than gram-positive bacteria.[181,182] This difference can be due to different cell wall structures of the two types of bacteria. A Gram-positive bacterial cell has a thick multilayered peptidoglycan (PG) cell wall. In contrast, a Gram-negative bacterial cell consists of a thin PG layer which can make the bacterial cell more susceptible. Also, it has been

reported that fast-growing bacteria like E. coli are more susceptible than slow-growing bacteria like S. aureus to NPs.

3.4 Photocatalytic application of ZnO NPs with different morphologies

This chapter is based on joint work with the Islamic Azad University of Shahreza in Iran. The results in this chapter have been submitted to the "International Journal of Environmental Science and Technology".

3.4.1 Characterization of ZnO nanoparticles

XRD analysis of ZnO nanoparticles are summarized in Figure 3.36. All of the ZnO nanoparticles exhibited diffraction peaks correlated with those of (100), (002), (101), (102), (110), (103) and (200) planes which can be exactly indexed as the wurtize ZnO with lattice constants a = 0.3249 nm and c = 0.5206 nm. These results correspond well with the values in the standard card (JCPDS 36-1451).[183] Afterwards, ZnO powders were labelled as sample A, B and C, when synthesized in 1-hexanol, ethylene glycol and water as solvents, respectively. According to the XRD pattern, it can be concluded that all synthesized ZnO powders are crystallized well because all peaks are very sharp. Also, no characteristic peaks from other impurities are observed. Moreover, the particles size is estimated by employing Scherrer's formula based on the diffraction peak corresponding to the (002) plane, and the average particle size is 78, 64 and 49 nm for sample A, B and C, respectively.

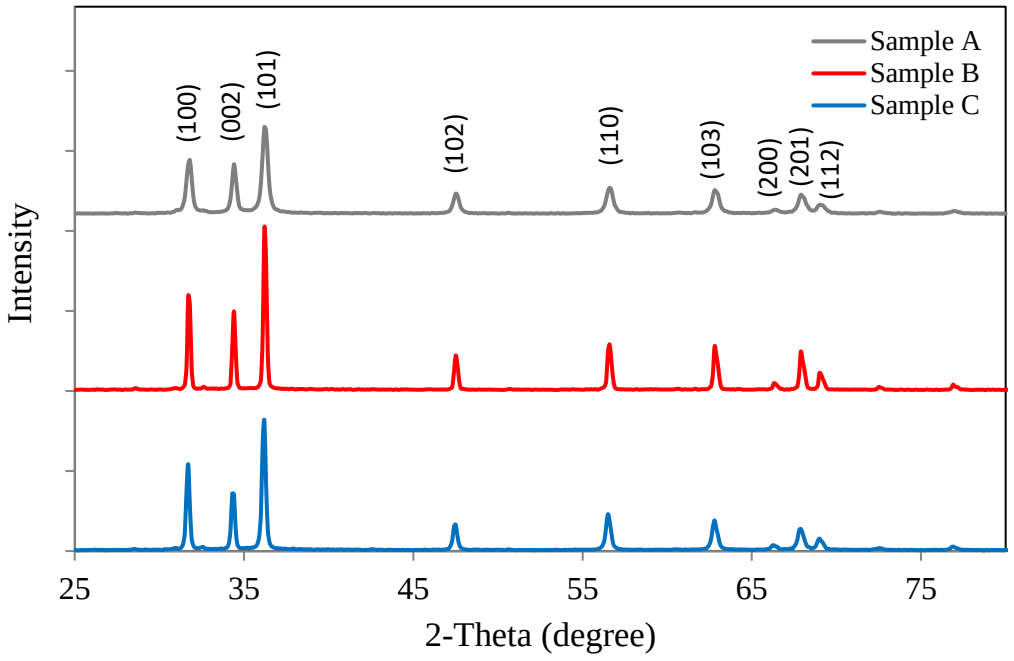

Figure 3.36 XRD patterns of the as-prepared ZnO nanoparticles synthesized in 1-hexanol (Sample A), ethylene glycol (Sample B) and water (Sample C).[184]

Further structural characterization of the ZnO powders was performed by SEM. The result of the SEM measurements were provided by the colleagues during the joint work. As illustrated in SEM images, different solvents contribute to the different morphologies of samples (Figure 3.37). It was revealed that the particles synthesized in 1-hexanol, ethylene glycol and water have rod, sphere and flower shape, respectively.

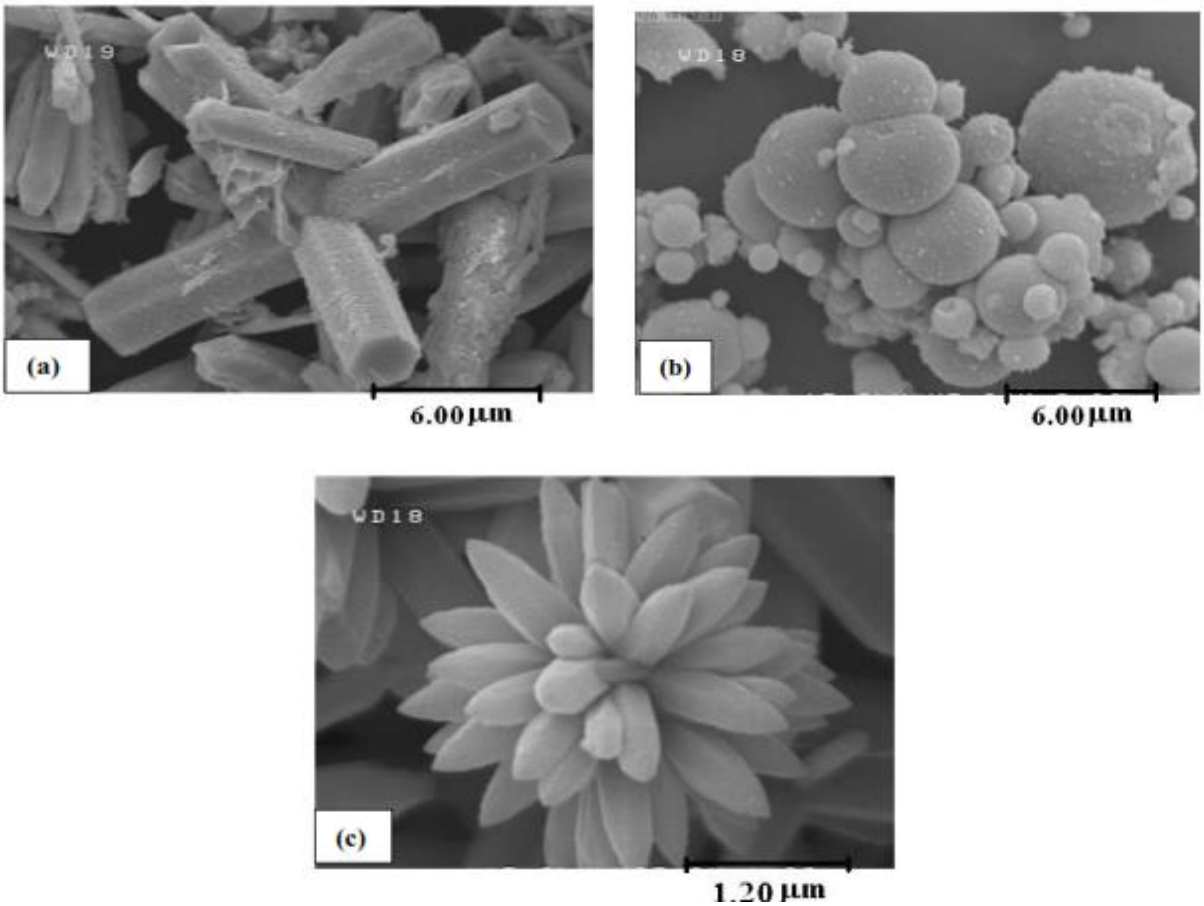

Figure 3.37 The SEM images of synthesized ZnO particles. (a) Sample A;(b) Sample B; (c) Sample C.[184]

In this experiment, external reaction factors such as zinc acetate dihydrate (the zinc source), the concentration of precursors, pH, temperature, and time were kept the same for all of the reactions. Thus, different morphologies of the various prepared ZnO samples can only be due to the impacts of the different solvents.

Figure 3.38 shows the UV-vis absorption spectra of synthesized ZnO powders. The optical band gap (E_g) of the ZnO samples was calculated by extrapolation of the linear portion of $(\alpha h\upsilon)^2$ as a function of hυ using the following equation:[185]

$$(\alpha h\upsilon)^2 = A\,(h\upsilon - E_g)^n$$

Where α is absorption coefficient, hυ is the photon energy, E_g the optical band-gap energy and A is a constant, depending on the electron-hole mobility, having a value between 10^5 cm^{-1} eV^{-1} and 10^6 cm^{-1} eV^{-1}. Good linearity was seen for different n values at n = 1 (direct allowed transition) that revealed the best fit for ZnO samples (not displayed here). The band gap value increases in the order of sample C (3.27) < sample B (3.31) < sample A (3.34), which is in consistency with particle size.

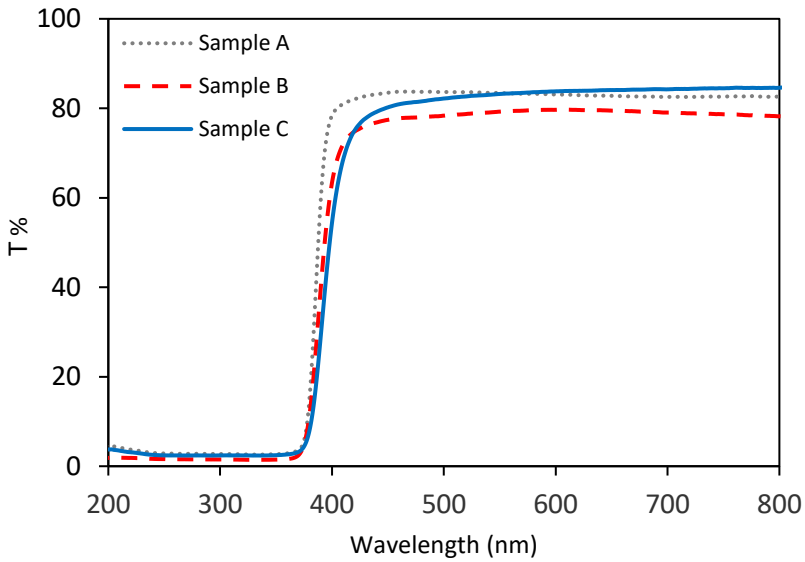

Figure 3.38 The UV-vis absorption spectra of synthesized ZnO nanoparticles.[184]

3.4.2 Photocatalytic activity

All of the ZnO powders were used to evaluate their photocatalytic activity in the presence of UV light. Results of blank experiments showed that the removal of the azo dye of 20 mg/L was negligible either during the 2h under the illumination of UV light, or with the addition of photocatalyst when they were used alone. However, it was found that reduction of azo dye with the addition of catalyst under the presence of UV light is considerable in contrast to blank

experiments. Photocatalytic reduction results of different ZnO powders at a dye concentration of 20 mg/L, catalyst loading of 0.2 g/L, reaction time of 2 hours, initial pH = 5 are demonstrated in Figure 3.39.

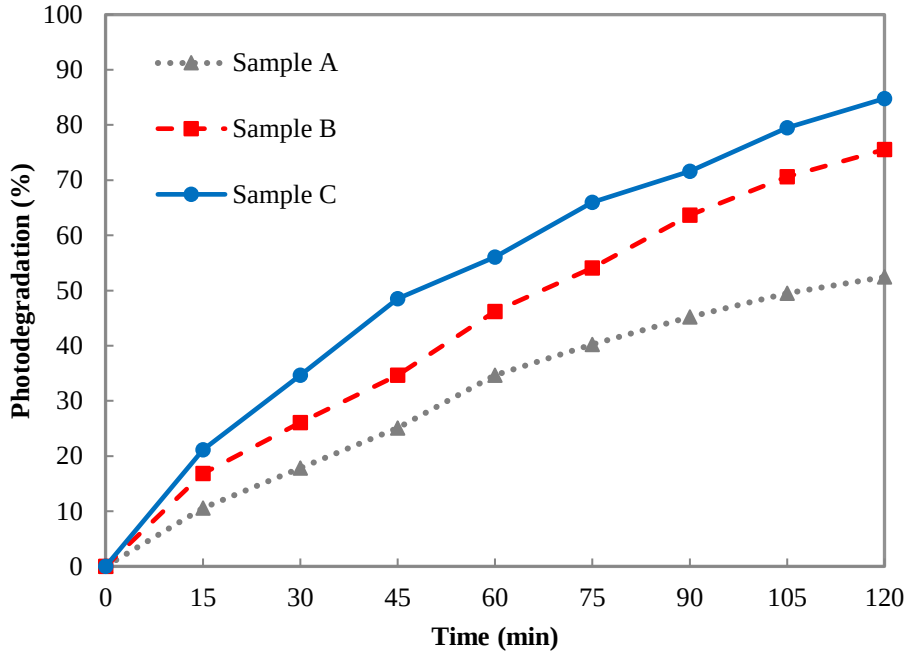

Figure 3.39 The photocatalytic reduction of sample azo dye by synthesized ZnO nanoparticles.[184]

It can be observed that all synthesized ZnO nanoparticles exhibited considerably high photocatalytic activity under the presence of UV light. Also, it can be seen that the photocatalytic activity of nanoparticles is inversely related to the particle size. The nanoflower ZnO showed the highest photocatalytic performance as 84.9% of the azo dye is eliminated within 120 min. The high photo-activity of synthesized ZnO nanoparticles can be attributed to their structure and morphology to absorb a large fraction of UV light. It can be concluded that the particle size changes influence the photocatalytic activity of ZnO nanoparticles through surface area improvement. Also, as reported in the literature, differences in photocatalytic activity are related to the type and concentration of oxygen vacancies on the surface.[186]

In this experiment, the kinetic behavior of photocatalytic reduction of azo dye was best presented by a first-order rate equation:

$$Ln\,[C_0/C] = kt$$

In this equation, C_0 is the initial dye concentration, C is the dye concentration at time t, k is the rate constant, and t is the reaction time. LnC_0/C against reaction time plots are drawn in Figure 3.40, and rate constants are deduced from the slopes.

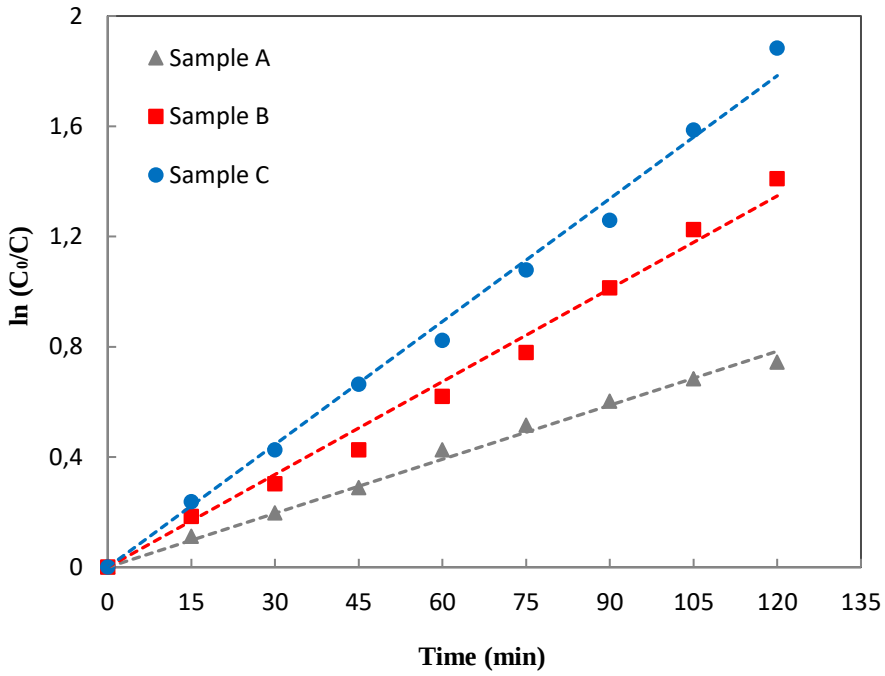

Figure 3.40 First-order kinetic model for the photocatalytic reduction of sample azo dye by prepared ZnO nanoparticles (dye concentration= 20 mg/L, pH= 5, catalyst loading= 0.2 g/L).[184]

Table 3 gives the comparative kinetic parameters and the corresponding coefficients of determination for the dye photocatalytic reduction by synthesized ZnO nanoparticles. $T_{1/2}$ is the half-life value ($T_{1/2} = 0.6932/ k$).

Table 3. Kinetic parameters and linear coefficient R^2 for photocatalytic reduction of azo dye by different ZnO nanoparticles

Samples	k (min^{-1})	$T_{1/2}$ (min)	R^2
Sample A	0.006	115.533	0.993
Sample B	0.011	63.018	0.989
Sample C	0.014	49.514	0.992

This result will contribute to the potential application of synthesized ZnO nanoparticles for the treatment of dye contaminated wastewater.

4 Summary and outlook

4.1 Research summary

In the first part of this thesis, we reported the synthesis of a core-shell Au@Ag NP with a high SERS enhancement factor to study the exchange and competition of different coating agents with different binding abilities to simulate the release of NPs into a water body with several potential coating agents. Suwannee River Natural Organic Matter (SRNOM), 4-mercaptobenzoic acid (4-MBA) and 4-Mercaptopyridine (4-MPy) were selected molecules for the experiments. SERS Experimental setup parameters such as aggregation size, laser excitation wavelength and laser power were optimized before further experiments were conducted. It was shown, 4-MPy has a higher binding affinity than SRNOM and 4-MBA through the presence of simultaneous sulfur and nitrogen atoms which leads to dominating the coating process when two coating agents are present in the media at the same time. Furthermore, 4-MBA and 4-MPy make bonds to the SRNOM coated nanoparticle despite that SRNOM coating has been previously formed. Therefore, with regard to the hypothesis mentioned in the introduction, it can be concluded that the first contact of potential coating agents does not drive the fate of the NPs which is rather controlled by a dynamic equilibrium and weak coating agents can be replaced by stronger binding coating agents.

In the second part, the synthesized Au@Ag NPs were successfully coated on silicon wafer using polydiallyldimethylammonium chloride to produce SERS substrates to detect different molecules easily. 4-MBA and 4-MPy were selected as sample molecules, and a detection limit as low as 5×10^{-9} M was obtained. Also, the application of the prepared substrate was evaluated by measuring 4-MPy molecule in more complex media such as tap water and water obtained from melted snow. The spectra obtained from 4-MPy in tap water showed an additional band which can be contributed to the presence of ions and impurities in the media. Also, the substrate was implemented to successfully characterize the 4-MPy coating on unmodified Degussa P25 TiO_2 NPs.

In the third part, the P25 Degussa TiO_2 NPs were thermally modified at different temperatures of 500, 650, 800 and 950°C to achieve NP with different crystal structure, morphology and size. The modified NPs were successfully used to characterize the formation and stability of coatings by SERS and also as photocatalytic material for deactivation of *Escherichia coli* and *Staphylococcus aureus* as model microorganisms. It was observed that the crystal structure of TiO_2 NPs plays an important role in their application. TiO_2 NPs modified at 500 °C showed the

highest SERS enhancement factor and also antibacterial activity against the sample microorganism. The SERS results showed the stability of 4-MBA coating on TiO_2 NPs after several washing steps. It was also observed that SERS Spectra of the coating show some changes if heavy metal ions are present in the media during the coating process. The peak positions of the SERS bands exhibit some apparent change with the kind of metal ion, showing a blue or red shift compared with those in the SERS spectrum of 4-MBA.

In the last section, ZnO NPs with different morphologies were synthesized via an easy hydrothermal method by using different solvents. The ZnO NPs were used for degradation of a sample azo dye. SEM imaging revealed that the particles synthesized in 1-hexanol, ethylene glycol and water have rod, sphere and flower shape, respectively. The photocatalytic efficiencies of the ZnO NPs were affected by their different morphologies and crystal growth habits, particle size and optical properties. Results indicate that flower-like ZnO NPs showed significantly higher photocatalytic efficiency than rod- and sphere-like ZnO NPs.

4.2 Future research work

Microfluidic systems are progressively gaining attention and finding their way into real world applications due to miniaturization of systems that are normally employed in laboratories. These systems allow flexible and highly controlled manipulation of liquids, suspended particles and biological samples. Therefore, integration of SERS and Microfluidic systems can be a key enabler for future applications. Integration of microfluidic systems for the SERS measurement of coating experiments would be another step toward a more realistic environmental condition than the actual experimental setup carried out in the lab.

The main drawback in the application of semiconductors is their wide band gap energy, limiting the spectral range of adsorbable solar photons to the UV region ($\lambda < 400$ nm) which is almost just 5% of the light reaching the earth's surface. This drawback of semiconductors can be improved by elementary doping, plasmonic enhancement or surface modification with organic molecules. However, these methods can also decrease the material performance. Therefore, further research can be done to increase the application of semiconductor material as photocatalyst by different modification methods to improve their physical and chemical properties. Also, the SERS application of semiconductors is a fast growing topic which further research can be done in this field to develop semiconductor substrates for the detection of

different chemicals. So far only a few molecules are found to be selectively enhanced by semiconductors, which limits the application fields of semiconductor-induced SERS. Thus, more studies are necessary to be conducted to better understand the semiconductor-enhanced Raman scattering for further improvements from fundamental studies to real practical systems.

5 Abbreviations

4-MBA	4-mercaptobenzoic acid
4-MPy	4-mercaptopyridine
AFM	atomic force microscopy
BET	Brunauer-Emmett-Teller
CB	conduction band
CFU	colony-forming unit
CIP	ciprofloxacin
CT	charge transfer
DBPs	disinfection byproducts
DLS	dynamic light scattering
EDX	energy-dispersive X-ray spectroscopy
EINP	engineered inorganic nanoparticle
EM	electromagnetic enhancement
FCS	fluorescence correlation spectroscopy
FFF	field flow fractionation
FTIR	Fourier Transform Infrared Spectroscopy
FWHM	full width at half maximum
HA	humic acid
HOMO	highest occupied molecular orbital
HPLC	high-performance liquid chromatography
HPSEC	high-performance size-exclusion chromatography
ICP-MS	inductively coupled plasma mass spectroscopy

LEIS	low energy ion scattering
LSPR	localized surface plasmon resonance
LUMO	lowest unoccupied molecular orbital
NB	Nutrient broth medium
NOM	Natural Organic Matter
NP	nanoparticle
NTA	nanoparticle tracking analysis
PDDA	polydiallyldimethylammonium chloride
PMMA	poly (methyl methacrylate)
PVP	polyvinylpyrrolidone
RS	Raman spectroscopy
ROS	reactive oxygen species
RSD	relative standard deviation
SEM	Scanning Electron Microscopy
SERS	surface-enhanced Raman scattering
SERRS	surface-enhanced resonance Raman scattering
SFG	surface sum-frequency generation
SIMS	secondary ion mass spectroscopy
SRNOM	Suwannee River Natural Organic Matter
STM	scanning tunneling spectroscopy
TEM	Transmission Electron Microscopy
UV	Ultra Violet

VB	valence band
XRD	X-ray crystallography

6 References

1. Aragay, G., Pino, F. & Merkoci, A. Nanomaterials for sensing and destroying pesticides. *Chemical reviews* **112**, 5317–5338 (2012).
2. Saha, S., Pal, A., Kundu, S., Basu, S. & Pal, T. Photochemical green synthesis of calcium-alginate-stabilized Ag and Au nanoparticles and their catalytic application to 4-nitrophenol reduction. *Langmuir* **26**, 2885–2893 (2009).
3. Sabouni, R. & Gomaa, H. Photocatalytic degradation of pharmaceutical micro-pollutants using ZnO. *Environmental Science and Pollution Research* 1–9 (2019).
4. Wang, Q. H., Kalantar-Zadeh, K., Kis, A., Coleman, J. N. & Strano, M. S. Electronics and optoelectronics of two-dimensional transition metal dichalcogenides. *Nature nanotechnology* **7**, 699 (2012).
5. Krishnan, N. *et al.* A hybrid life cycle inventory of nano-scale semiconductor manufacturing. *Environmental science & technology* **42**, 3069–3075 (2008).
6. Sharon, M., Choudhary, A. K. & Kumar, R. Nanotechnology in agricultural diseases and food safety. *Journal of Phytology* (2010).
7. Eslamian, S., Amininezhad, S. M., Amininejad, S. M. & Adamowski, J. Application of Nanotechnology in Water Reuse. in *Urban Water Reuse Handbook* 836–840 (CRC Press, 2016).
8. Han, J., Liu, Y., Singhal, N., Wang, L. & Gao, W. Comparative photocatalytic degradation of estrone in water by ZnO and TiO2 under artificial UVA and solar irradiation. *Chemical Engineering Journal* **213**, 150–162 (2012).
9. Ghaedi, M., Ahmadi, F. & Shokrollahi, A. Simultaneous preconcentration and determination of copper, nickel, cobalt and lead ions content by flame atomic absorption spectrometry. *Journal of Hazardous Materials* **142**, 272–278 (2007).
10. Talebian, N., Amininezhad, S. M. & Doudi, M. Controllable synthesis of ZnO nanoparticles and their morphology-dependent antibacterial and optical properties. *Journal of Photochemistry and Photobiology B: Biology* **120**, 66–73 (2013).

11. Sirelkhatim, A. *et al.* Review on zinc oxide nanoparticles: antibacterial activity and toxicity mechanism. *Nano-Micro Letters* **7**, 219–242 (2015).
12. Armelao, L. *et al.* Photocatalytic and antibacterial activity of TiO2 and Au/TiO2 nanosystems. *Nanotechnology* **18**, 375709 (2007).
13. Paul, T., Miller, P. L. & Strathmann, T. J. Visible-light-mediated TiO2 photocatalysis of fluoroquinolone antibacterial agents. *Environmental Science & Technology* **41**, 4720–4727 (2007).
14. Swetha, S., Santhosh, S. M. & Geetha Balakrishna, R. Synthesis and comparative study of nano-TiO2 over degussa P-25 in disinfection of water. *Photochemistry and photobiology* **86**, 628–632 (2010).
15. Frimmel, F. H. & Niessner, R. *Nanoparticles in the water cycle*. (Springer, 2014).
16. Sun, T. Y., Gottschalk, F., Hungerbühler, K. & Nowack, B. Comprehensive probabilistic modelling of environmental emissions of engineered nanomaterials. *Environmental Pollution* **185**, 69–76 (2014).
17. Baalousha, M., Nur, Y., Römer, I., Tejamaya, M. & Lead, J. R. Effect of monovalent and divalent cations, anions and fulvic acid on aggregation of citrate-coated silver nanoparticles. *Science of the Total Environment* **454**, 119–131 (2013).
18. Gao, J. *et al.* Influence of Suwannee River humic acid on particle properties and toxicity of silver nanoparticles. *Chemosphere* **89**, 96–101 (2012).
19. Wang, Z., Zhang, L., Zhao, J. & Xing, B. Environmental processes and toxicity of metallic nanoparticles in aquatic systems as affected by natural organic matter. *Environmental Science: Nano* **3**, 240–255 (2016).
20. Huynh, K. A. & Chen, K. L. Aggregation kinetics of citrate and polyvinylpyrrolidone coated silver nanoparticles in monovalent and divalent electrolyte solutions. *Environmental science & technology* **45**, 5564–5571 (2011).

21. Schaumann, G. E. *et al.* Understanding the fate and biological effects of Ag-and TiO2-nanoparticles in the environment: the quest for advanced analytics and interdisciplinary concepts. *Science of the Total Environment* **535**, 3–19 (2015).
22. Sharma, V. K., Siskova, K. M., Zboril, R. & Gardea-Torresdey, J. L. Organic-coated silver nanoparticles in biological and environmental conditions: fate, stability and toxicity. *Advances in colloid and interface science* **204**, 15–34 (2014).
23. Kühn, M., Ivleva, N. P., Klitzke, S., Niessner, R. & Baumann, T. Investigation of coatings of natural organic matter on silver nanoparticles under environmentally relevant conditions by surface-enhanced Raman scattering. *Science of The Total Environment* **535**, 122–130 (2015).
24. Marsich, L. *et al.* Poly- L -lysine-Coated Silver Nanoparticles as Positively Charged Substrates for Surface-Enhanced Raman Scattering. *Langmuir* **28**, 13166–13171 (2012).
25. Musumeci, A. *et al.* SERS of semiconducting nanoparticles (TiO2 hybrid composites). *Journal of the American Chemical Society* **131**, 6040–6041 (2009).
26. Yang, L. *et al.* Observation of enhanced Raman scattering for molecules adsorbed on TiO2 nanoparticles: charge-transfer contribution. *The Journal of Physical Chemistry C* **112**, 20095–20098 (2008).
27. Yang, B. *et al.* Recent development of SERS technology: semiconductor-based study. *Acs Omega* **4**, 20101–20108 (2019).
28. Lombardi, J. R. The theory of surface-enhanced Raman scattering on semiconductor nanoparticles; toward the optimization of SERS sensors. *Faraday discussions* **205**, 105–120 (2017).
29. Ong, T. T., Blanch, E. W. & Jones, O. A. Surface Enhanced Raman Spectroscopy in environmental analysis, monitoring and assessment. *Science of The Total Environment* **720**, 137601 (2020).
30. Maier, S. A. *Plasmonics: fundamentals and applications*. (Springer Science & Business Media, 2007).
31. Messiah, A. *Quantum Mechanics Ch. XVII*. (Courier Dover Publications, 1999).

32. Nayfeh, M. H. *Fundamentals and Applications of Nano Silicon in Plasmonics and Fullerines: Current and Future Trends*. (Elsevier, 2018).
33. Hamamatsu Photonics, K. K. *Nanophotonics*. (2016).
34. Willets, K. A. & Van Duyne, R. P. Localized surface plasmon resonance spectroscopy and sensing. *Annu. Rev. Phys. Chem.* **58**, 267–297 (2007).
35. Al-Amri, M. D., El-Gomati, M. & Suhail Zubairy, M. *Optics in Our Time*. (Springer Nature, 2016).
36. Banerjee, S., Dionysiou, D. D. & Pillai, S. C. Self-cleaning applications of TiO2 by photo-induced hydrophilicity and photocatalysis. *Applied Catalysis B: Environmental* **176**, 396–428 (2015).
37. Meilert, K. T., Laub, D. & Kiwi, J. Photocatalytic self-cleaning of modified cotton textiles by TiO2 clusters attached by chemical spacers. *Journal of molecular catalysis A: chemical* **237**, 101–108 (2005).
38. Paz, Y. Application of TiO2 photocatalysis for air treatment: Patents' overview. *Applied Catalysis B: Environmental* **99**, 448–460 (2010).
39. Lu, M. *Photocatalysis and water purification: from fundamentals to recent applications*. (John Wiley & Sons, 2013).
40. Whelton, A. J. *et al.* Residential tap water contamination following the Freedom Industries chemical spill: perceptions, water quality, and health impacts. *Environmental science & technology* **49**, 813–823 (2015).
41. Plappally, A. K. Energy requirements for water production, treatment, end use, reclamation, and disposal. *Renewable and Sustainable Energy Reviews* **16**, 4818–4848 (2012).
42. Daghrir, R., Drogui, P. & Robert, D. Modified TiO2 for environmental photocatalytic applications: a review. *Industrial & Engineering Chemistry Research* **52**, 3581–3599 (2013).
43. Marin, M. L., Santos-Juanes, L., Arques, A., Amat, A. M. & Miranda, M. A. Organic photocatalysts for the oxidation of pollutants and model compounds. *Chemical reviews* **112**, 1710–1750 (2011).
44. Tekin, D., Kiziltas, H. & Ungan, H. Kinetic evaluation of ZnO/TiO2 thin film photocatalyst in photocatalytic degradation of Orange G. *Journal of Molecular Liquids* **306**, 112905 (2020).

45. Zhou, X. *et al.* Improved electron-hole separation and migration in V2O5/rutile-anatase photocatalyst system with homo-hetero junctions and its enhanced photocatalytic performance. *Chemical Engineering Journal* **330**, 294–308 (2017).
46. Dong, S. *et al.* Recent developments in heterogeneous photocatalytic water treatment using visible light-responsive photocatalysts: a review. *Rsc Advances* **5**, 14610–14630 (2015).
47. Martínez, C., Fernández, M. I., Santaballa, J. A. & Faria, J. Kinetics and mechanism of aqueous degradation of carbamazepine by heterogeneous photocatalysis using nanocrystalline TiO2, ZnO and multi-walled carbon nanotubes–anatase composites. *Applied Catalysis B: Environmental* **102**, 563–571 (2011).
48. Sakthivel, S. *et al.* Solar photocatalytic degradation of azo dye: comparison of photocatalytic efficiency of ZnO and TiO2. *Solar Energy Materials and Solar Cells* **77**, 65–82 (2003).
49. Daneshvar, N., Salari, D. & Khataee, A. R. Photocatalytic degradation of azo dye acid red 14 in water on ZnO as an alternative catalyst to TiO2. *Journal of photochemistry and photobiology A: chemistry* **162**, 317–322 (2004).
50. Testino, A. *et al.* Optimizing the photocatalytic properties of hydrothermal TiO2 by the control of phase composition and particle morphology. A systematic approach. *Journal of the American Chemical Society* **129**, 3564–3575 (2007).
51. Ohno, T., Sarukawa, K., Tokieda, K. & Matsumura, M. Morphology of a TiO2 photocatalyst (Degussa, P-25) consisting of anatase and rutile crystalline phases. *Journal of Catalysis* **203**, 82–86 (2001).
52. Tian, J., Zhao, Z., Kumar, A., Boughton, R. I. & Liu, H. Recent progress in design, synthesis, and applications of one-dimensional TiO2 nanostructured surface heterostructures: a review. *Chemical Society Reviews* **43**, 6920–6937 (2014).
53. Chen, X. & Selloni, A. *Introduction: titanium dioxide (TiO2) nanomaterials*. (ACS Publications, 2014).

54. Malekshahi Byranvand, M., Nemati Kharat, A., Fatholahi, L. & Malekshahi Beiranvand, Z. A review on synthesis of nano-TiO2 via different methods. *Journal of nanostructures* **3**, 1–9 (2013).
55. Gribb, A. A. & Banfield, J. F. Particle size effects on transformation kinetics and phase stability in nanocrystalline TiO2. *American Mineralogist* **82**, 717–728 (1997).
56. Fujishima, A. & Zhang, X. Titanium dioxide photocatalysis: present situation and future approaches. *Comptes Rendus Chimie* **9**, 750–760 (2006).
57. Caratto, V. *et al.* Inactivation of Escherichia coli on anatase and rutile nanoparticles using UV and fluorescent light. *Materials Research Bulletin* **48**, 2095–2101 (2013).
58. Hidalgo, M. C., Maicu, M., Navío, J. A. & Colón, G. Photocatalytic properties of surface modified platinised TiO2: Effects of particle size and structural composition. *Catalysis Today* **129**, 43–49 (2007).
59. Bosc, F., Ayral, A., Keller, N. & Keller, V. Room temperature visible light oxidation of CO by high surface area rutile TiO2-supported metal photocatalyst. *Applied Catalysis B: Environmental* **69**, 133–137 (2007).
60. Isa, E. D. M., Shameli, K., Jusoh, N. W. C. & Hazan, R. Rapid photodecolorization of methyl orange and rhodamine B using zinc oxide nanoparticles mediated by pullulan at different calcination conditions. *Journal of Nanostructure in Chemistry* 1–16 (2020).
61. Jones, N., Ray, B., Ranjit, K. T. & Manna, A. C. Antibacterial activity of ZnO nanoparticle suspensions on a broad spectrum of microorganisms. *FEMS microbiology letters* **279**, 71–76 (2008).
62. Brunner, T. J. *et al.* In vitro cytotoxicity of oxide nanoparticles: comparison to asbestos, silica, and the effect of particle solubility. *Environmental science & technology* **40**, 4374–4381 (2006).
63. Applerot, G. *et al.* Enhanced antibacterial activity of nanocrystalline ZnO due to increased ROS-mediated cell injury. *Advanced Functional Materials* **19**, 842–852 (2009).
64. Hirota, K. *et al.* Preparation of zinc oxide ceramics with a sustainable antibacterial activity under dark conditions. *Ceramics International* **36**, 497–506 (2010).

65. Talebian, N., Nilforoushan, M. R. & Zargar, E. B. Enhanced antibacterial performance of hybrid semiconductor nanomaterials: ZnO/SnO2 nanocomposite thin films. *Applied Surface Science* **258**, 547–555 (2011).

66. Grillo, R., Rosa, A. H. & Fraceto, L. F. Engineered nanoparticles and organic matter: A review of the state-of-the-art. *Chemosphere* **119**, 608–619 (2015).

67. Kühn, M., Ivleva, N. P., Klitzke, S., Niessner, R. & Baumann, T. Investigation of coatings of natural organic matter on silver nanoparticles under environmentally relevant conditions by surface-enhanced Raman scattering. *Science of The Total Environment* **535**, 122–130 (2015).

68. Ivleva, N. P., Wagner, M., Horn, H., Niessner, R. & Haisch, C. In situ surface-enhanced Raman scattering analysis of biofilm. *Analytical chemistry* **80**, 8538–8544 (2008).

69. Schuster, K. C., Reese, I., Urlaub, E., Gapes, J. R. & Lendl, B. Multidimensional information on the chemical composition of single bacterial cells by confocal Raman microspectroscopy. *Analytical chemistry* **72**, 5529–5534 (2000).

70. Zhou, H. Label-Free Applications of SERS for Bacteria Analysis. (Technische Universität München, 2014).

71. Bertrand, M. J. *Handbook of Instrumental Techniques for Analytical Chemistry Edited by Frank A. Settle. Prentice Hall: Upper Saddle River. 1997. xxi+ 995 pp. ISBN 0-13-177338-0.* (ACS Publications, 1998).

72. Kneipp, K. *et al.* Single molecule detection using surface-enhanced Raman scattering (SERS). *Physical review letters* **78**, 1667 (1997).

73. Fleischmann, M., Hendra, P. J. & McQuillan, A. J. Raman spectra of pyridine adsorbed at a silver electrode. *Chemical Physics Letters* **26**, 163–166 (1974).

74. Ivleva, N. P., Wagner, M., Horn, H., Niessner, R. & Haisch, C. Raman microscopy and surface-enhanced Raman scattering (SERS) for in situ analysis of biofilms. *Journal of biophotonics* **3**, 548–556 (2010).

75. Zhou, H. *et al.* SERS detection of bacteria in water by in situ coating with Ag nanoparticles. *Analytical chemistry* **86**, 1525–1533 (2014).

76. Lane, L. A., Qian, X. & Nie, S. SERS nanoparticles in medicine: from label-free detection to spectroscopic tagging. *Chemical reviews* **115**, 10489–10529 (2015).

77. Kneipp, K., Moskovits, M. & Kneipp, H. *Surface-enhanced Raman scattering: physics and applications*. vol. 103 (Springer Science & Business Media, 2006).

78. Kneipp, J., Kneipp, H. & Kneipp, K. SERS—a single-molecule and nanoscale tool for bioanalytics. *Chemical Society Reviews* **37**, 1052–1060 (2008).

79. Sun, Z., Zhao, B. & Lombardi, J. R. ZnO nanoparticle size-dependent excitation of surface Raman signal from adsorbed molecules: Observation of a charge-transfer resonance. *Applied Physics Letters* **91**, 221106 (2007).

80. Wang, Y. *et al.* Enhanced Raman scattering as a probe for 4-mercaptopyridine surface-modified copper oxide nanocrystals. *Analytical sciences* **23**, 787–791 (2007).

81. Wang, Y. *et al.* Mercaptopyridine surface-functionalized CdTe quantum dots with enhanced Raman scattering properties. *The Journal of Physical Chemistry C* **112**, 996–1000 (2008).

82. Xue, X. *et al.* Raman investigation of nanosized TiO2: effect of crystallite size and quantum confinement. *The Journal of Physical Chemistry C* **116**, 8792–8797 (2012).

83. Wang, X., Shi, W., She, G. & Mu, L. Surface-enhanced Raman scattering (SERS) on transition metal and semiconductor nanostructures. *Physical Chemistry Chemical Physics* **14**, 5891–5901 (2012).

84. Kneipp, K., Kneipp, H., Itzkan, I., Dasari, R. R. & Feld, M. S. Surface-enhanced Raman scattering and biophysics. *Journal of Physics: Condensed Matter* **14**, R597 (2002).

85. Ding, S.-Y., You, E.-M., Tian, Z.-Q. & Moskovits, M. Electromagnetic theories of surface-enhanced Raman spectroscopy. *Chemical Society Reviews* **46**, 4042–4076 (2017).

86. Haynes, C. L., McFarland, A. D. & Van Duyne, R. P. *Surface-enhanced Raman spectroscopy*. (ACS Publications, 2005).

87. Guo, H., He, L. & Xing, B. Applications of surface-enhanced Raman spectroscopy in the analysis of nanoparticles in the environment. *Environmental Science: Nano* **4**, 2093–2107 (2017).
88. Campion, A. & Kambhampati, P. Surface-enhanced Raman scattering. *Chemical society reviews* **27**, 241–250 (1998).
89. Witlicki, E. H. *et al.* Turning on resonant SERRS using the chromophore- plasmon coupling created by host- guest complexation at a plasmonic nanoarray. *Journal of the American Chemical Society* **132**, 6099–6107 (2010).
90. Kim, N. H., Lee, S. J. & Moskovits, M. Aptamer-mediated surface-enhanced Raman spectroscopy intensity amplification. *Nano letters* **10**, 4181–4185 (2010).
91. Li, X., Jiang, L., Zhan, Q., Qian, J. & He, S. Localized surface plasmon resonance (LSPR) of polyelectrolyte-functionalized gold-nanoparticles for bio-sensing. *Colloids and Surfaces A: Physicochemical and Engineering Aspects* **332**, 172–179 (2009).
92. Wei, H., Abtahi, S. M. H. & Vikesland, P. J. Plasmonic colorimetric and SERS sensors for environmental analysis. *Environmental Science: Nano* **2**, 120–135 (2015).
93. Mock, J. J., Barbic, M., Smith, D. R., Schultz, D. A. & Schultz, S. Shape effects in plasmon resonance of individual colloidal silver nanoparticles. *The Journal of Chemical Physics* **116**, 6755–6759 (2002).
94. Mock, J. J., Smith, D. R. & Schultz, S. Local refractive index dependence of plasmon resonance spectra from individual nanoparticles. *Nano letters* **3**, 485–491 (2003).
95. Sherry, L. J., Jin, R., Mirkin, C. A., Schatz, G. C. & Van Duyne, R. P. Localized surface plasmon resonance spectroscopy of single silver triangular nanoprisms. *Nano letters* **6**, 2060–2065 (2006).
96. Deinert, J.-C. Zinc oxide surfaces and interfaces: electronic structure and dynamics of excited states. (Technische Universität Berlin, 2016).
97. Han, X. X., Ji, W., Zhao, B. & Ozaki, Y. Semiconductor-enhanced Raman scattering: Active nanomaterials and applications. *Nanoscale* **9**, 4847–4861 (2017).

98. Maznichenko, D., Venkatakrishnan, K. & Tan, B. Stimulating multiple SERS mechanisms by a nanofibrous three-dimensional network structure of titanium dioxide (TiO2). *The Journal of Physical Chemistry C* **117**, 578–583 (2012).

99. Maznichenko, D., Venkatakrishnan, K. & Tan, B. Stimulating multiple SERS mechanisms by a nanofibrous three-dimensional network structure of titanium dioxide (TiO2). *The Journal of Physical Chemistry C* **117**, 578–583 (2012).

100. Islam, S. K., Tamargo, M., Moug, R. & Lombardi, J. R. Surface-enhanced Raman scattering on a chemically etched ZnSe surface. *The Journal of Physical Chemistry C* **117**, 23372–23377 (2013).

101. Valley, N., Greeneltch, N., Van Duyne, R. P. & Schatz, G. C. A Look at the Origin and Magnitude of the Chemical Contribution to the Enhancement Mechanism of Surface-Enhanced Raman Spectroscopy (SERS): Theory and Experiment. *The Journal of Physical Chemistry Letters* **4**, 2599–2604 (2013).

102. Lombardi, J. R. & Birke, R. L. Time-dependent picture of the charge-transfer contributions to surface enhanced Raman spectroscopy. *The Journal of chemical physics* **126**, 244709 (2007).

103. Ling, X., Moura, L. G., Pimenta, M. A. & Zhang, J. Charge-transfer mechanism in graphene-enhanced Raman scattering. *The Journal of Physical Chemistry C* **116**, 25112–25118 (2012).

104. Quagliano, L. G. Observation of molecules adsorbed on III-V semiconductor quantum dots by surface-enhanced Raman scattering. *Journal of the American Chemical Society* **126**, 7393–7398 (2004).

105. Yang, L. *et al.* SERS investigation of ciprofloxacin drug molecules on TiO 2 nanoparticles. *Physical Chemistry Chemical Physics* **17**, 17809–17815 (2015).

106. Xue, X. *et al.* Enhanced Raman scattering when scatterer molecules located in TiO 2/Ag nanojunctions. *RSC Advances* **5**, 64235–64239 (2015).

107. Hirakawa, A. Y. & Tsuboi, M. Molecular geometry in an excited electronic state and a preresonance Raman effect. *Science* **188**, 359–361 (1975).

108. Nie, S. & Emory, S. R. Probing single molecules and single nanoparticles by surface-enhanced Raman scattering. *science* **275**, 1102–1106 (1997).

109. Cho, H. *et al.* Aptamer-based SERRS sensor for thrombin detection. *Nano letters* **8**, 4386–4390 (2008).

110. Thomson, G. & Batchelder, D. Development of a hand-held forensic-lidar for standoff detection of chemicals. *Review of scientific instruments* **73**, 4326–4328 (2002).

111. Muehlethaler, C., Leona, M. & Lombardi, J. R. Review of surface enhanced Raman scattering applications in forensic science. *Analytical chemistry* **88**, 152–169 (2015).

112. Cui, H., Li, S., Deng, S., Chen, H. & Wang, C. Flexible, Transparent, and Free-Standing Silicon Nanowire SERS Platform for in Situ Food Inspection. *ACS Sensors* **2**, 386–393 (2017).

113. Guo, H. *et al.* Analysis of silver nanoparticles in antimicrobial products using surface-enhanced raman spectroscopy (SERS). *Environmental science & technology* **49**, 4317–4324 (2015).

114. Kurouski, D. & Van Duyne, R. P. *In Situ* Detection and Identification of Hair Dyes Using Surface-Enhanced Raman Spectroscopy (SERS). *Analytical Chemistry* **87**, 2901–2906 (2015).

115. Xu, M.-L., Gao, Y., Han, X. X. & Zhao, B. Detection of Pesticide Residues in Food Using Surface-Enhanced Raman Spectroscopy: A Review. *Journal of Agricultural and Food Chemistry* **65**, 6719–6726 (2017).

116. Zhao, J., Zhang, K., Li, Y., Ji, J. & Liu, B. High-Resolution and Universal Visualization of Latent Fingerprints Based on Aptamer-Functionalized Core–Shell Nanoparticles with Embedded SERS Reporters. *ACS Applied Materials & Interfaces* **8**, 14389–14395 (2016).

117. Tian, F., Bonnier, F., Casey, A., Shanahan, A. E. & Byrne, H. J. Surface enhanced Raman scattering with gold nanoparticles: effect of particle shape. *Anal. Methods* **6**, 9116–9123 (2014).

118. Das, G. *et al.* Nano-patterned SERS substrate: application for protein analysis vs. temperature. *Biosensors and Bioelectronics* **24**, 1693–1699 (2009).

119. Qian, X.-M. & Nie, S. M. Single-molecule and single-nanoparticle SERS: from fundamental mechanisms to biomedical applications. *Chemical Society Reviews* **37**, 912–920 (2008).

120. Moskovits, M. Surface-enhanced Raman spectroscopy: a brief retrospective. *Journal of Raman Spectroscopy: An International Journal for Original Work in all Aspects of Raman Spectroscopy, Including Higher Order Processes, and also Brillouin and Rayleigh Scattering* **36**, 485–496 (2005).

121. Stamplecoskie, K. G., Scaiano, J. C., Tiwari, V. S. & Anis, H. Optimal size of silver nanoparticles for surface-enhanced Raman spectroscopy. *The Journal of Physical Chemistry C* **115**, 1403–1409 (2011).

122. Boca, S. C., Farcau, C. & Astilean, S. The study of Raman enhancement efficiency as function of nanoparticle size and shape. *Nuclear Instruments and Methods in Physics Research Section B: Beam Interactions with Materials and Atoms* **267**, 406–410 (2009).

123. Sussman, E. M., Jayanti, P., Dair, B. J. & Casey, B. J. Assessment of total silver and silver nanoparticle extraction from medical devices. *Food and Chemical Toxicology* **85**, 10–19 (2015).

124. Holbrook, R. D., Rykaczewski, K. & Staymates, M. E. Dynamics of silver nanoparticle release from wound dressings revealed via in situ nanoscale imaging. *Journal of Materials Science: Materials in Medicine* **25**, 2481–2489 (2014).

125. Reed, R. B. *et al.* Potential environmental impacts and antimicrobial efficacy of silver-and nanosilver-containing textiles. *Environmental science & technology* **50**, 4018–4026 (2016).

126. Quadros, M. E. & Marr, L. C. Silver nanoparticles and total aerosols emitted by nanotechnology-related consumer spray products. *Environmental science & technology* **45**, 10713–10719 (2011).

127. Orendorff, C. J., Gole, A., Sau, T. K. & Murphy, C. J. Surface-enhanced Raman spectroscopy of self-assembled monolayers: sandwich architecture and nanoparticle shape dependence. *Analytical chemistry* **77**, 3261–3266 (2005).

128. Guo, H., Xing, B., Hamlet, L. C., Chica, A. & He, L. Surface-enhanced Raman scattering detection of silver nanoparticles in environmental and biological samples. *Science of The Total Environment* **554**, 246–252 (2016).

129. Zhao, B. *et al.* A green, facile, and rapid method for microextraction and Raman detection of titanium dioxide nanoparticles from milk powder. *RSC Advances* **7**, 21380–21388 (2017).

130. Love, J. C., Estroff, L. A., Kriebel, J. K., Nuzzo, R. G. & Whitesides, G. M. Self-assembled monolayers of thiolates on metals as a form of nanotechnology. *Chemical reviews* **105**, 1103–1170 (2005).

131. Sekine, R., Vongsvivut, J., Robertson, E. G., Spiccia, L. & McNaughton, D. Comparative Analysis of Surface-Enhanced Raman Spectroscopy of Daidzein and Formononetin. *The Journal of Physical Chemistry B* **114**, 7104–7111 (2010).

132. Giese, B. & McNaughton, D. Surface-enhanced Raman spectroscopic and density functional theory study of adenine adsorption to silver surfaces. *The Journal of Physical Chemistry B* **106**, 101–112 (2002).

133. Iliescu, T., Baia, M. & Kiefer, W. FT-Raman, surface-enhanced Raman spectroscopy and theoretical investigations of diclofenac sodium. *Chemical physics* **298**, 167–174 (2004).

134. Li, W., Camargo, P. H., Lu, X. & Xia, Y. Dimers of silver nanospheres: facile synthesis and their use as hot spots for surface-enhanced Raman scattering. *Nano letters* **9**, 485–490 (2008).

135. Liu, K. *et al.* Porous Au–Ag nanospheres with high-density and highly accessible hotspots for SERS analysis. *Nano letters* **16**, 3675–3681 (2016).

136. Yang, M. *et al.* SERS-active gold lace nanoshells with built-in hotspots. *Nano letters* **10**, 4013–4019 (2010).

137. Leng, W. & Vikesland, P. J. MGITC facilitated formation of AuNP multimers. *Langmuir* **30**, 8342–8349 (2014).

138. Wei, W. Y. & White, I. M. A simple filter-based approach to surface enhanced Raman spectroscopy for trace chemical detection. *Analyst* **137**, 1168–1173 (2012).

139. Xing, B., Senesi, N. & Vecitis, C. D. *Engineered nanoparticles and the environment: biophysicochemical processes and toxicity*. vol. 4 (John Wiley & Sons, 2016).

140. Cui, L., Wu, D.-Y., Wang, A., Ren, B. & Tian, Z.-Q. Charge-transfer enhancement involved in the SERS of adenine on Rh and Pd demonstrated by ultraviolet to visible laser excitation. *The Journal of Physical Chemistry C* **114**, 16588–16595 (2010).

141. Ren, B. *et al.* Surface-enhanced Raman scattering in the ultraviolet spectral region: UV-SERS on rhodium and ruthenium electrodes. *Journal of the American Chemical Society* **125**, 9598–9599 (2003).

142. Wen, Z. Raman spectroscopy of protein pharmaceuticals. *Journal of Pharmaceutical Sciences* **96**, 2861–2878 (2007).

143. Kalachyova, Y., Lyutakov, O., Kostejn, M., Clupek, M. & Svorcik, V. Silver nanostructures: From individual dots to coupled strips for the tailoring of SERS excitation wavelength from near-UV to near-IR. *Electronic Materials Letters* **11**, 288–294 (2015).

144. Zhang, Z., Guo, H., Deng, Y., Xing, B. & He, L. Mapping gold nanoparticles on and in edible leaves in situ using surface enhanced Raman spectroscopy. *RSC Advances* **6**, 60152–60159 (2016).

145. Guo, H., Xing, B., White, J. C., Mukherjee, A. & He, L. Ultra-sensitive determination of silver nanoparticles by surface-enhanced Raman spectroscopy (SERS) after hydrophobization-mediated extraction. *Analyst* **141**, 5261–5264 (2016).

146. Guo, H., Xing, B. & He, L. Development of a filter-based method for detecting silver nanoparticles and their heteroaggregation in aqueous environments by surface-enhanced Raman spectroscopy. *Environmental Pollution* **211**, 198–205 (2016).

147. Zhao, B., Yang, T., Zhang, Z., Hickey, M. E. & He, L. A triple functional approach to simultaneously determine the type, concentration, and size of titanium dioxide particles. *Environmental science & technology* **52**, 2863–2869 (2018).

148. Mitrano, D. M. *et al.* Presence of nanoparticles in wash water from conventional silver and nano-silver textiles. *ACS nano* **8**, 7208–7219 (2014).

149. Levard, C., Hotze, E. M., Lowry, G. V. & Brown Jr, G. E. Environmental transformations of silver nanoparticles: impact on stability and toxicity. *Environmental science & technology* **46**, 6900–6914 (2012).

150. Bell, S. E. & McCourt, M. R. SERS enhancement by aggregated Au colloids: effect of particle size. *Physical Chemistry Chemical Physics* **11**, 7455–7462 (2009).

151. Corrado, G., Sanchez-Cortes, S., Francioso, O. & Garcia-Ramos, J. V. Surface-enhanced Raman and fluorescence joint analysis of soil humic acids. *analytica chimica acta* **616**, 69–77 (2008).

152. Roldán, M. L., Corrado, G., Francioso, O. & Sánchez-Cortés, S. Interaction of soil humic acids with herbicide paraquat analyzed by surface-enhanced Raman scattering and fluorescence spectroscopy on silver plasmonic nanoparticles. *Analytica chimica acta* **699**, 87–95 (2011).

153. Song, L., Mao, K., Zhou, X. & Hu, J. A novel biosensor based on Au@Ag core–shell nanoparticles for SERS detection of arsenic (III). *Talanta* **146**, 285–290 (2016).

154. Li, H. *et al.* Detection of 6-Thioguanine by surface-enhanced Raman scattering spectroscopy using silver nanoparticles-coated silicon wafer. *Colloids and Surfaces A: Physicochemical and Engineering Aspects* **493**, 52–58 (2016).

155. Le, T. K., Flahaut, D., Martinez, H., Nguyen, H. K. H. & Huynh, T. K. X. Study of the effects of surface modification by thermal shock method on photocatalytic activity of TiO2 P25. *Applied Catalysis B: Environmental* **165**, 260–268 (2015).

156. Amininejad, S., Ivleva, N. P. & Baumann, T. Characterization of coatings on metallic nanoparticles by surface-enhanced Raman scattering (SERS) for environmental purposes. *Vadose Zone Journal* **19**, e20076 (2020).

157. Riddick, T. M. *Control of colloid stability through zeta potential: with a closing chapter on its relationship to cardiovascular disease*. (1968).

158. De Leersnyder, I., De Gelder, L., Van Driessche, I. & Vermeir, P. Revealing the importance of aging, environment, size and stabilization mechanisms on the stability of metal nanoparticles: A case study for silver nanoparticles in a minimally defined and complex undefined bacterial growth medium. *Nanomaterials* **9**, 1684 (2019).

159. Yaffe, N. R., Ingram, A., Graham, D. & Blanch, E. W. A multi-component optimisation of experimental parameters for maximising SERS enhancements. *Journal of Raman Spectroscopy* **41**, 618–623 (2009).

160. Wang, Z. & Rothberg, L. J. Origins of Blinking in Single-Molecule Raman Spectroscopy. *The Journal of Physical Chemistry B* **109**, 3387–3391 (2005).

161. Zhang, L., Bai, Y., Shang, Z., Zhang, Y. & Mo, Y. Experimental and theoretical studies of Raman spectroscopy on 4-mercaptopyridine aqueous solution and 4-mercaptopyridine/Ag complex system. *Journal of Raman Spectroscopy* **38**, 1106–1111 (2007).

162. Ho, C.-H. & Lee, S. SERS and DFT investigation of the adsorption behavior of 4-mercaptobenzoic acid on silver colloids. *Colloids and Surfaces A: Physicochemical and Engineering Aspects* **474**, 29–35 (2015).

163. Yuan, H., Fales, A. M., Khoury, C. G., Liu, J. & Vo-Dinh, T. Spectral characterization and intracellular detection of Surface-Enhanced Raman Scattering (SERS)-encoded plasmonic gold nanostars: Nanostars SERS characterization. *Journal of Raman Spectroscopy* **44**, 234–239 (2013).

164. Dreaden, E. C., Alkilany, A. M., Huang, X., Murphy, C. J. & El-Sayed, M. A. The golden age: gold nanoparticles for biomedicine. *Chemical Society Reviews* **41**, 2740–2779 (2012).

165. Rycenga, M. *et al.* Controlling the synthesis and assembly of silver nanostructures for plasmonic applications. *Chemical reviews* **111**, 3669–3712 (2011).

166. Zheng, X.-S. *et al.* Laser Power Dependent Surface-Enhanced Raman Spectroscopic Study of 4-Mercaptopyridine on Uniform Gold Nanoparticle-Assembled Substrates. *The Journal of Physical Chemistry C* **118**, 3750–3757 (2014).

167. Dai, S., Zhang, X., Du, Z., Huang, Y. & Dang, H. Structural properties and Raman spectroscopy of lipid Langmuir monolayers at the air–water interface. *Colloids and surfaces B: Biointerfaces* **42**, 21–28 (2005).

168. Zhu, Y., Li, M., Yu, D. & Yang, L. A novel paper rag as 'D-SERS'substrate for detection of pesticide residues at various peels. *Talanta* **128**, 117–124 (2014).

169. Cheng, M.-L., Tsai, B.-C. & Yang, J. Silver nanoparticle-treated filter paper as a highly sensitive surface-enhanced Raman scattering (SERS) substrate for detection of tyrosine in aqueous solution. *Analytica chimica acta* **708**, 89–96 (2011).

170. Kundu, S., Mandal, M., Ghosh, S. K. & Pal, T. Photochemical deposition of SERS active silver nanoparticles on silica gel and their application as catalysts for the reduction of aromatic nitro compounds. *Journal of colloid and interface science* **272**, 134–144 (2004).

171. Liu, X., Chen, G. & Su, C. Effects of material properties on sedimentation and aggregation of titanium dioxide nanoparticles of anatase and rutile in the aqueous phase. *Journal of colloid and interface science* **363**, 84–91 (2011).

172. Scherrer, P. Bestimmung der inneren Struktur und der Größe von Kolloidteilchen mittels Röntgenstrahlen. in *Kolloidchemie Ein Lehrbuch* 387–409 (Springer, 1912).

173. Scherrer, P. Göttinger nachrichten math. *Phys* **2**, 98–100 (1918).

174. Dou, L., Gao, L., Yang, X. & Song, X. Hierarchical architectures TiO2: Pollen-inducted synthesis, remarkable crystalline-phase stability, tunable size, and reused photo-catalysis. *Journal of hazardous materials* **203**, 363–369 (2012).

175. Thongsuwan, W., Kumpika, T. & Singjai, P. Photocatalytic property of colloidal TiO2 nanoparticles prepared by sparking process. *Current Applied Physics* **8**, 563–568 (2008).

176. Liu, X., Chen, G., Erwin, J. G. & Su, C. Silicon impurity release and surface transformation of TiO2 anatase and rutile nanoparticles in water environments. *Environmental pollution* **184**, 570–578 (2014).

177. Yang, L. *et al.* Adsorption study of 4-MBA on TiO2 nanoparticles by surface-enhanced Raman spectroscopy. *Journal of Raman Spectroscopy: An International Journal for Original Work in all Aspects of Raman Spectroscopy, Including Higher Order Processes, and also Brillouin and Rayleigh Scattering* **40**, 2004–2008 (2009).

178. Zhang, Z. L., Li, D. N. & Mao, Y. L. Effects of trap density on the surface-enhanced Raman scattering of molecules adsorbed on TiO2 (Degussa P25). *Journal of Raman Spectroscopy* **43**, 1920–1923 (2012).

179. Yang, L. *et al.* Investigation on SERS of different phase structure TiO2 nanoparticles. *Journal of Raman Spectroscopy* **46**, 287–292 (2015).

180. Yamamoto, O. Influence of particle size on the antibacterial activity of zinc oxide. *International Journal of Inorganic Materials* **3**, 643–646 (2001).

181. Rincón, A.-G. & Pulgarin, C. Bactericidal action of illuminated TiO2 on pure Escherichia coli and natural bacterial consortia: post-irradiation events in the dark and assessment of the effective disinfection time. *Applied Catalysis B: Environmental* **49**, 99–112 (2004).

182. Pal, A., Pehkonen, S. O., Liya, E. Y. & Ray, M. B. Photocatalytic inactivation of Gram-positive and Gram-negative bacteria using fluorescent light. *Journal of Photochemistry and Photobiology A: Chemistry* **186**, 335–341 (2007).

183. Mridha, S. & Basak, D. Effect of thickness on the structural, electrical and optical properties of ZnO films. *Materials research bulletin* **42**, 875–882 (2007).

184. Amininejad, S., Baumann, T., Talebian, N. & Amininezhad, S. M. Application of ZnO nanoparticles with different morphologies for photocatalytic reduction of a sample azo dye in aqueous solution. *International Journal of Environmental Science and Technology,* (submitted).

185. Jia, H., Hu, Y., Tang, Y. & Zhang, L. Synthesis and photoelectrochemical behavior of nanocrystalline CdS film electrodes. *Electrochemistry communications* **8**, 1381–1385 (2006).

186. Zheng, Y. *et al.* Luminescence and photocatalytic activity of ZnO nanocrystals: correlation between structure and property. *Inorganic chemistry* **46**, 6675–6682 (2007).